RRCAT Newsletter

Vol. 39, Issue 1, 2026

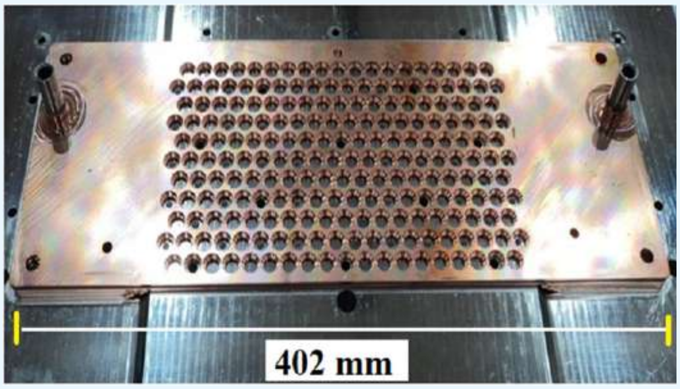

Raja Ramanna Centre for Advanced Technology, Indore

Inside view of the IR-FEL facility at RRCAT

Indigenously developed SSR-2 SCRF Cavity for PIP-II project

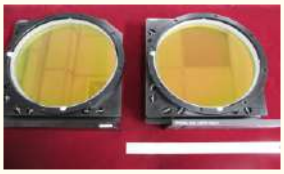

High transmission, high LIDT AR coated optics of 200 mm diameter

LAM-DED based manufacturing of thin wall dome structure

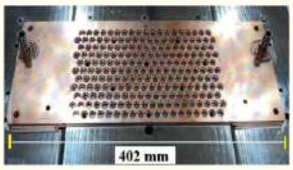

Prototype Acceleration Grid plate with embedded cooling channels

Indigenously developed VME32 DAQ card for FCT interface

From the Director's Desk...

It gives me immense pleasure to present this issue of the RRCAT Newsletter covering the period July–December 2025. This issue captures a vibrant spectrum of scientific, technological, engineering, and institutional achievements accomplished across the Centre. The activities reported here span some of the most challenging frontiers of modern science and technology, which includes accelerator physics, superconducting RF systems, synchrotron radiation sources, high-power lasers, free-electron lasers, advanced materials, cryogenics, vacuum science, precision instrumentation, additive manufacturing, biomedical diagnostics, and applied photonics.

The continued reliable operation and technological enhancement of the Indus synchrotron radiation facilities remain a matter of great satisfaction. These national facilities support a large user community and play a pivotal role in enabling cutting-edge research across multiple scientific disciplines. Equally encouraging is the progress achieved in development of SSR-2 superconducting RF cavities, compact low level RF systems, cryogenic infrastructure for testing superconducting magnets, and indigenous development of critical accelerator subsystems, all of which strengthen our long-term capabilities in accelerator science and technology.

The achievements reported by the Laser Group are equally noteworthy. Advances in high-power laser systems, ultrafast science, laser-driven ion acceleration, optical coatings, semiconductor-based radiation detector technologies, and high-energy laser components demonstrate the Centre's continuing leadership in laser research. The successful demonstration of laser-driven proton acceleration at the PW Laser Facility represents an important milestone and opens new opportunities for frontier research in high-energy-density and plasma science.

The contributions in materials science and advanced technologies further illustrate the multidisciplinary nature of RRCAT's research ecosystem. These include opening up of the IR-FEL facility for external users, additive manufacturing for strategic and aerospace applications, development of advanced hyperspectral imaging system, Chromox ceramic based detector for hydrogen ions, flexible triboelectric energy harvesting devices, and Raman spectroscopy-based diagnostics reflect our commitment to translating fundamental research into impactful technologies.

The improvements in the IT infrastructure, advanced manufacturing technologies, and civil infrastructure continue to provide crucial support to various important projects of RRCAT, thereby enabling scientific programmes to progress efficiently and reliably. The theme articles on IR-FEL and LIBS summarize the recent developments which have taken place in these fields in the Centre.

I am particularly pleased to note the Centre's growing contributions to major national and international scientific programmes. The indigenous development of high-RRR niobium sheets, which were handed over by Dr. Ajit Kumar Mohanty, Chairman, AEC, and Secretary, DAE, to Shri Unmesh D. Malshe, the then Director, RRCAT, represent a major milestone in this direction. In addition, development of advanced accelerator components, superconducting technologies, and participation in collaborative programmes with leading international laboratories underline the confidence that the global scientific community places in RRCAT's technical expertise and scientific capabilities. Such collaborations not only enrich our scientific environment but also position India as a valued contributor to large-scale international scientific endeavours. The list of publications presented in this issue is a testament of the high quality of research being pursued at the Centre, and points towards the dedication, innovation, and excellence of our scientific community.

Beyond the scientific accomplishments, this issue also highlights our sustained focus on personnel safety, environmental stewardship, staff welfare activities, skill development, Hindi language promotional activities, and various community engagement. These dimensions are essential for all-round development of RRCAT staff members and a happy, healthy, vibrant scientific community.

My hearty congratulations to Shri Alok Singh and Shri Sachin Kumar Agrawal for being bestowed the Homi Bhabha Science and Technology Maan Patra for the year 2025 for their outstanding contribution to the Department. I also congratulate the other award winners in different categories, and look forward to many more such laurels for my colleagues in the years to come.

The RRCAT Newsletter occupies a special place among our institutional publications. It serves not only as a record of achievements but also as a valuable window through which the scientific community, collaborating institutions, policymakers, students, and the public can appreciate the challenging and impactful research and development activities being pursued at the Centre. I congratulate all contributors whose efforts have culminated in the achievements reported here.

I place on record my deep appreciation for the efforts put in by the newly constituted Editorial Board. The team has demonstrated remarkable commitment and professionalism in compiling and presenting this issue in an engaging manner. I am confident that the Newsletter will continue to evolve into a vibrant and widely appreciated publication that effectively communicates the Centre's accomplishments to the scientific community and society at large.

With best wishes,
June 17, 2026

Viraj P. Bhanage
Director, RRCAT

From the Editor's Desk...

The Editorial Board is happy to present this issue of the **RRCAT Newsletter (Vol. 39, Issue 1, 2026)**, which chronicles the diverse scientific, technological and institutional activities carried out at the Centre during the period **July–December 2025**. More than a compilation of technical reports, this Newsletter reflects the collective endeavour of scientists, engineers, technical staff and support personnel who continue to push the frontiers of accelerator science, laser technology, materials science and advanced engineering in pursuit of scientific excellence and technological self-reliance.

The articles featured in this issue demonstrate the remarkable breadth of research activities pursued at the Centre. The round-the-clock operation of the Indus-1 and Indus-2 synchrotron radiation facilities, together with advances in beamline instrumentation, accelerator magnets, precision power supplies, detector electronics, X-ray optics and indigenous data acquisition systems, underscore the Centre's sustained commitment towards providing world-class national research facilities while continuously enhancing their capabilities through indigenous technological innovations.

The achievements of the Proton Accelerator Group in superconducting RF technology, ultra-high vacuum systems, cryogenics, RF engineering and accelerator physics are very noteworthy. The development of superconducting cavities, qualification facilities for superconducting magnets, digital low-level RF systems and sophisticated computational tools represents significant progress towards realizing next-generation accelerator facilities based on indigenous technologies. These developments not only strengthen our scientific capabilities but also contribute to India's growing competence in strategically important accelerator technologies.

The Laser Group continues to expand the horizons of laser science and photonics through significant advances in high-power laser optics, ultrafast phenomena, high harmonic generation, laser-driven ion acceleration, fibre laser technologies and radiation detector development. The successful demonstration of a 20 MeV proton beam using laser-driven ion acceleration at the PW Laser Facility marks yet another important milestone that places RRCAT among the select institutions worldwide actively pursuing frontier research in high-energy-density science.

The multidisciplinary nature of research at RRCAT is vividly reflected in the contributions from the Materials Science and Advanced Technology Group. Developments ranging from additive manufacturing for aerospace applications and advanced ceramic materials to triboelectric energy harvesters, multimodal biomedical imaging systems and Raman spectroscopy-based food quality assessment illustrate how fundamental research is being translated into technologies with broad societal and industrial relevance. The successful operation of the Infrared Free Electron Laser in the user mode further reinforces the Centre's growing role as a national user facility serving researchers from diverse scientific disciplines.

The enabling contributions made by the Technology Development and Support Group through the strengthening of information technology infrastructure, development of specialized fabrication technologies and establishment of advanced accelerator subsystem development facilities are very significant.

This issue also includes two insightful theme articles highlighting the growing importance of Infrared Free Electron Laser user facilities and Laser-Induced Breakdown Spectroscopy as a powerful analytical tool. Together, they provide readers with an appreciation of emerging research opportunities and evolving technological applications in these exciting fields.

The rich publication output during the period is a testimony to the scientific productivity of the Centre, while the sections on events and institutional activities capture another equally important dimension of RRCAT. Activities related to safety and environmental management, the DAE–Fermilab quality interaction meeting, indigenous development of high-RRR niobium sheets, the Rashtriya Karmayogi programme, Hindi implementation, Women's Welfare Committee initiatives, Staff Club activities, awards and honours, and the induction of new colleagues collectively portray a vibrant institution that nurtures both scientific excellence and human values.

As RRCAT continues to contribute to several high technology national programs, effective dissemination of our scientific accomplishments becomes increasingly important. The RRCAT Newsletter serves a valuable outreach platform, documenting institutional progress, preserving scientific milestones and communicating our achievements to academia, industry, and policymakers.

The Editorial Board remains committed to continually enhancing the quality and reach of this publication. We warmly invite our colleagues to contribute technical articles that reflect the dynamic research environment of RRCAT. Through wider participation, the Newsletter can evolve into an even more vibrant and comprehensive chronicle of the Centre's scientific journey.

I sincerely acknowledge the valuable support extended by the members of the Editorial Board in bringing out this issue in a professional and timely manner. I also express our deep gratitude to the Director, RRCAT for his constant encouragement, guidance and unwavering support, which continue to inspire the Editorial Board in its endeavour to showcase the scientific and technological achievements of RRCAT to the wider community.

Sunil Verma
Chairman, Editorial Board
(On behalf of the RRCAT Newsletter Editorial Board)

With warm regards,
June 17, 2026

E.1: Status report on operation of Indus-1 and Indus-2 synchrotron radiation sources

The synchrotron radiation sources, Indus-1 and Indus-2, maintained excellent operational performance during second half of 2025. These machines, constituting a national facility, provided SR beam to the users from Indian universities, research institutes, national laboratories and industries on round-the-clock basis.

In the said period, both the machines were operated smoothly following prescribed safety procedures. Three planned shutdowns totaling 15 days were taken for preventive maintenance and upgradation activities. Taking this into account, the machines were operated for 169 days in round-the-clock mode. Beam availability for users in Indus-2 was 3182 hrs (~18.8 hrs/day) whereas in Indus-1, it was 3863 hrs (~22.8 hrs/day).

With this, in calendar year 2025, there were 337 days of RTC operation. Figures E.1.1 and E.1.2 shows beam availability for users in recent years.

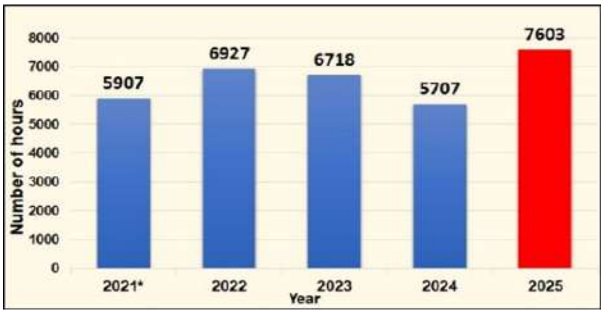

Fig. E.1.1: Indus-1 beam availability

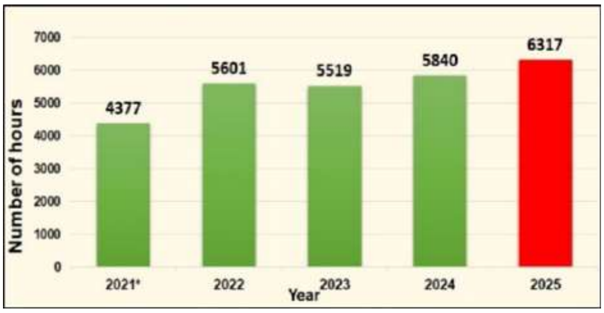

Fig. E.1.2: Indus-2 beam availability

Improvement in Indus-2 beam lifetime with skew quadrupoles: Since July 2024, the Indus-2 facility is being operated in low-emittance mode, wherein the emittance of electron beam is improved to 45 nm.rad, as compared to the 135 nm.rad earlier. This led to the improvement in flux by ~ 50% at fine focus beamlines. However, the beam lifetime gets significantly reduced in the low-emittance operation. Since October, 2025, the skew-quadrupole coils on the sextupole magnets in Indus-2 are being energized routinely using newly installed power converters that improved the beam life time from ~50 hours to ~70+ hours (Fig. E.1.3).

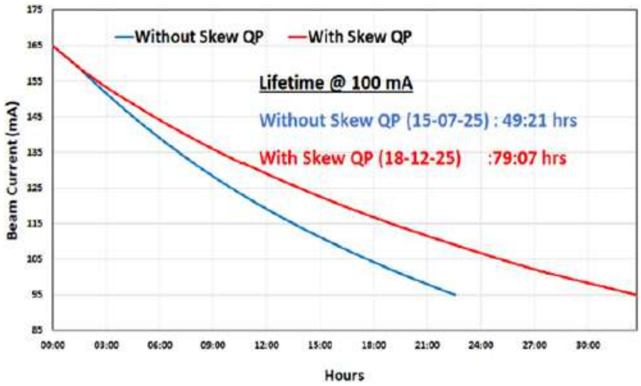

Fig. E.1.3: Improvement in beam lifetime by energizing skew-quadrupole

Utilization: A total of seven beamlines in Indus-1 and twenty beamlines in Indus-2 are operational. Users from a number of universities, research institutes and industries carried out experiments at these beamlines. More details on beam utilization on Indus beamlines is given in report E.2.

Machine Studies: During two days per month reserved for machine experiments, calculation of alignment offsets of BPIs using BBA technique and the improvement of beam lifetime in Indus-2 with skew quadrupole was completed successfully.

Major Upgrade and Upkeep Activities: During sheduled shutdowns of the machine, beamline frontend components of BL-11 and BL-12, namely, water-cooled shutter and fixed mask, were replaced.

Training Qualification and Licensing (TQL) Programme: The training of 6th batch of operators under TQL programme was completed successfully in September. Twenty four personnel have been trained and qualified for operation of Indus facility at qualifying levels 3, 4 and 5 (Fig. E.1.4). This team of dedicated operation crew is now shouldering round-the-clock operation of the machine.

Fig. E.1.4: 6th batch of TQLP staff for operation of Indus facility

Reported by:
Rajesh Kumar Sahu (rksahu@rrcat.gov.in)

E.2: User activities at Indus beamlines

Indus-1 and Indus-2 are national facilities that have a total of 27 operational beamlines. These beamlines have been in regular use by the scientists, researchers and students from the Indian academia and Indian industry. The total number of user experiments that have been carried out at Indus beamlines during June-Dec 2025 were 482 and 120 peer reviewed publication generated. More than 104 academic institutes and 7 industries utilized Indus for their research work. Work on diverse topics have been carried out at the Indus beamlines. Some of the published works are highlighted below:

The Scanning EXAFS investigations revealed how atomic-level tailoring of Zn-ZIF-8 via RuNi nanoalloy replacement enhances hydrogen evolution reaction (HER) performance. Concurrent studies focus on Zn–air batteries, high-energy-density systems limited by sluggish oxygen reduction and oxygen evolution kinetics and the monofunctional behaviour of conventional metal–organic frameworks (MOFs). Measurements have been pivotal in the development of a bifunctional FeNi-MOF/C_3N_5 catalyst. EXAFS resolved the mixed Fe/Ni coordination environment, revealing metal-supported electronic coupling, charge redistribution, and reaction-specific catalytic switching. Consequently, the material functioned as an efficient bifunctional catalyst, improving battery power output and cycling stability (*Advanced Functional Materials Volume 36, Issue 19, 2025*).

Also, investigation was done on the role of orbital degrees of freedom in $CrVO_4$, focusing on orbital-driven spin-exchange interactions and spin-phonon coupling through both experiments using x-ray absorption fine structure measurements and first-principles calculations. This work was published in *Phys. Rev. Research 7, 043189, 2025*. The field of high-entropy oxides (HEOs) surprises traditional materials science. By exploring material properties via tuning configurational disorder one can imbues HEOs with surprising functional properties, sometimes surpassing those of their more ordered counterparts. Strain-Driven Lattice Distortion in Calcium-Added (Co, Cu, Mg, Ni, Zn)O and its Electrical Properties have been studied using spectroscopy beamlines at Indus *(Advanced Engineering Materials, Volume 27, Issue 23 2025)*.

Influence of high-pressure severe plastic deformation on germanium using rotational diamond anvil cell was examined using in situ scanning micro-XRD measurements. Nearly threefold reduction in the cubic diamond to β-tin phase transition (PT) was observed. PT initiation pressure varied from ~ 10.4 GPa under quasi-hydrostatic conditions to ~ 3.1 GPa under severe plastic deformation at high pressures. These findings provide the first in situ evidence of plastic strain–driven phase transformation in germanium and emphasize the critical role of deviatoric stresses in shaping phase behaviour in covalently bonded materials.

Protein crystallography beamline of Indus-2 has been used by various national labs. Crystal Structure of glucose tolerant beta-glucosidase has been determined which has implications in bioethanol production. Crystal structures of two artificial intelligence (AI) designed protein which bind specifically to cancer and SARS-CoV-2 proteins have been determined, which has importance for diagnosis and therapy. Crystal Structure of HadAB protein complexes with its substrate from TB causing bacteria, *Mycobacterium tuberculosis*, have also been determined. In the calendar year, total of 30 protein structures has been released in Protein Data Bank (PDB) and published in peer-reviewed journals.

Synchrotron-assisted micro X-ray fluorescence based mapping of micro nutrient was carried out using microprobe-XRF beamline. The study was done on for four representative Indian wheat varieties; namely Emmer (Khapli), Bansi (durum), Sonamoti (Indian dwarf wheat), and black wheat. A thin transverse cross-section of the wheat grain was prepared using microtome cutter of thickness ~ 200 µm to investigate the spatial distribution of important micro-nutrients present in different varieties of grains. µ-XRF results clearly demonstrate that elemental distribution within the wheat grains is highly non-uniform and strongly dependent on grain anatomy. In case of all wheat grains, K, Fe, Cu, and Zn were found to be predominantly localized in the bran layer region, particularly in the aleurone region, while the endosperm region was largely devoid of essential micronutrient elements. This observation highlights that there are fair chances of loss of essential minerals during the conventional milling processes that removes mostly bran region. This study showed that Sonamoti wheat, which is considered to be very age-old Indian wheat variety, contains relatively higher amount of micronutrients abundance compared to other wheat varieties *(Analytical Letters, Volume 59, Issue 6, 1096-1108, 2025).*

Regarding applications for DAE and ISRO, stress analysis of different weld joints and components have been carried out for optimizing the fabrications process. Also, number of soft and hard x-ray detectors were calibrated for ISRO's Aditya mission.

Reported by:
Sanjay Rai (sanjayrai@rrcat.gov.in)

E.3: Development of high-quality X-ray multilayer mirror for hard X-ray applications

X-ray multilayer (ML) optics plays a vital role to manipulate X-rays for frontier scientific and technological applications. It acts as a notch filter passing a narrow band of energies. ML mirror is advantageous compared to diffractive crystal optics because of greater flux and design flexibility. In addition, ML mirrors allow a variety of optical configuration by tailoring reflective responses using a figured surface. The objective of the present work is to develop high-quality X-ray ML mirrors for high-throughput and high-resolution applications in the hard X-ray energy range (10–20 keV). Indigenous development of such precision optics is essential for HBSRS (Indus-3) beamlines to deliver diffraction-limited, coherence-preserving X-ray beams. The major challenge in fabricating these mirrors lies in achieving nanometer-scale layer thicknesses with angstrom-level precision and atomically smooth interfaces across hundreds of layer pairs.

Mo/Si and W/B_4C ML mirrors have been successfully developed with low achievable interface roughness (~0.21–0.24 nm) and thickness errors below 0.2%, suitable for high-performance X-ray applications. Under optimized deposition conditions, Mo/Si ML mirrors are designed for high-flux applications, whereas W/B_4C ML mirrors are optimized for moderate- to high-resolution applications. All MLs are deposited using magnetron sputtering with carefully tuned periodicities and number of layer pairs to optimize for either high photon flux or high spectral resolution.

Fabricated structural parameters of ML Mirrors: Mo/Si MLs (ML-1 and ML-2) have periods (d) of 9.43 and 6.53 nm, layer pairs (N) of 60 and 50, and roughness (σ) of 0.24 and 0.21 nm, respectively. W/B_4C MLs (ML-3 and ML-4) have d = 3.74 and 1.85 nm, N = 50 and 400, and σ = 0.24 and 0.27 nm, respectively.

A systematic investigation of the structure, stress and optical property correlation is carried out for hard x-ray application. Optical performance, measured using Indus-2 in the 10–20 keV range, shows that Mo/Si MLs exhibit high measured reflectivity (R_m80–92%) and excellent integrated reflectivity, suitable for high-flux applications. In contrast, W/B_4C MLs with shorter periods provide high-resolution performance with relative energy resolution (ΔE/E) down to ~1.2%. The results indicate high quality of fabricated ML mirrors.
A representative measured first-order Bragg reflectivity (R) profiles of MLs are shown in Fig. E.3.1, with the results as follows:

ML-1: $R_m \approx 82\%$, $\Delta E/E \approx 11.9\%$ at 10 keV
ML-2: $R_m \approx 81\%$, $\Delta E/E \approx 6.8\%$ at 11 keV
ML-3: $R_m \approx 81\%$, $\Delta E/E \approx 4.1\%$ at 10 keV
ML-4: $R_m \approx 60\%$, $\Delta E/E \approx 1.2\%$ at 10 keV

ML-1 and ML-2 show excellent agreement with the theoretical reflectivity, R_T (R_m/R_T> 0.93) up to 18 keV, with a sharp drop at 20 keV due to the absorption edge. ML-3 shows reasonable agreement, with R_m/R_T ranging from 0.91 to 0.97 across 10–20 keV. In contrast, ML-4 exhibits significantly reduced values (0.75 at 10 keV and 0.55 at 14 keV), mainly due to enhanced interdiffusion in the ultra-short period structure.

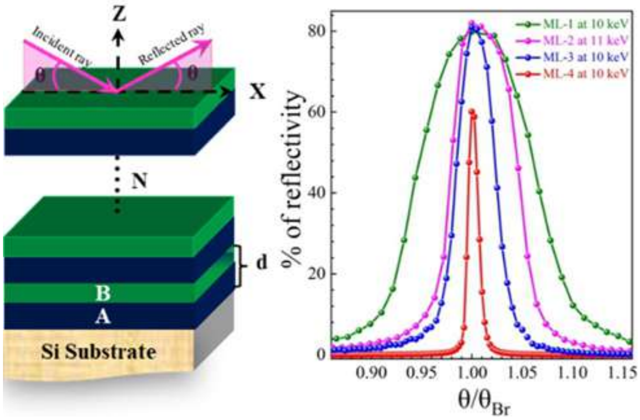

Fig. E.3.1: (a) Schematic of a ML structure. (b) Measured reflectivity data using Indus-2 of first order Bragg peak for four MLs, normalized to Bragg angle.

The results are comparable to current international benchmarks for similar multilayer X-ray optics. The study demonstrates that Mo/Si systems are well suited for high-flux applications, while W/B_4C systems provide high-resolution performance, addressing different requirements in hard X-ray optics. These outcomes offer valuable insights for optimizing the design of multilayer-based synchrotron mirrors and monochromators for future Indus-3 applications.

For further details please see: Mollick Faiyaz, Nayak Maheswar et al., "Structure, stress, and optical property correlations in nano-structured Mo/Si and W/B_4C multilayer mirrors for hard x-tray applications", *J. Appl. Phys. 138, 175303 (2025).*

Reported by:
Maheswar Nayak (mnayak@rrcat.gov.in)

E.4: Characterization of spectropolarimeter test mirror samples using Indus-1 reflectivity beamline

To study the coronal magnetic field in the solar atmosphere, an extreme ultraviolet (EUV) spectropolarimeter is proposed by Indian Institute of Astrophysics (IIA), Bengaluru for wavelength range of 50–100 nm (24.8–12.4 eV). The proposed spectropolarimeter will be used to measure the degree of linear polarization and the orientation of the polarization vector associated with the EUV emission from the solar corona. Using the Hanle effect, the measured polarization information will be used to study the vector magnetic fields of solar corona.

The EUV spectropolarimeter will comprised of a set of reflective mirrors, mirrors are set in Brewster's angle geometry. Theoretical analyses suggest the platinum coated EUV mirror has a good polarization power and high reflectivity (> 40%). Platinum-coated test mirror samples fabricated using a DC sputtering setup at the CeNSE laboratory, Indian Institute of Science (IISc), Bengaluru, were tested at the reflectivity beamline which provides the soft x-ray and VUV photons in the energy range of 10 to 300 eV with an energy resolution (E/ΔE) ~200-500. Both angle and energy dependent reflectivity measurements were performed in s and p polarization geometry to experimentally determine the Brewster angle and corresponding reflectivity of Pt coated test mirror samples. The experimental results obtained so will be used for validation of platinum coated mirrors for EUV solar spectropolarimeter applications by IIA group. Inside view of the beamline goniometer setup arranged in p-polarization geometry for EUV reflectivity experiments is shown in Fig. E.4.1.

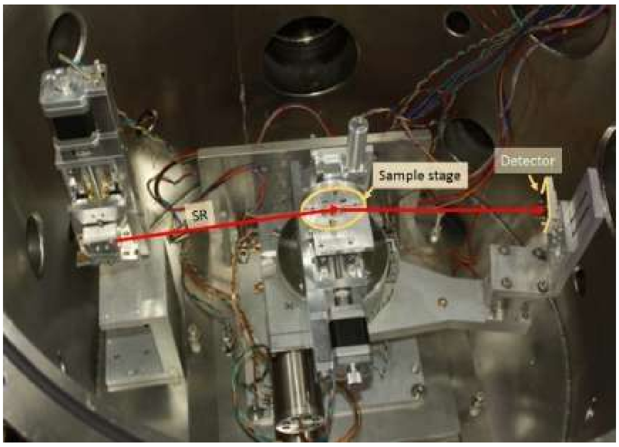

Fig. E.4.1: Inside view of the BL-04 experimental station setup in p- polarization geometry.

Measured Energy dependent reflectivity curves for s- and p-polarized radiation near the Brewster angle are shown in Fig. E.4.2. The experimentally obtained R_s and R_p demonstrate strong polarization performance and show good agreement with Zemax simulations, confirming the suitability of platinum coatings for EUV polarimeter mirrors. R_s and R_p reflectivities are also compared with Werner et. al [1] and Windt et. al [2] results (Shown in Fig. E.4.2).

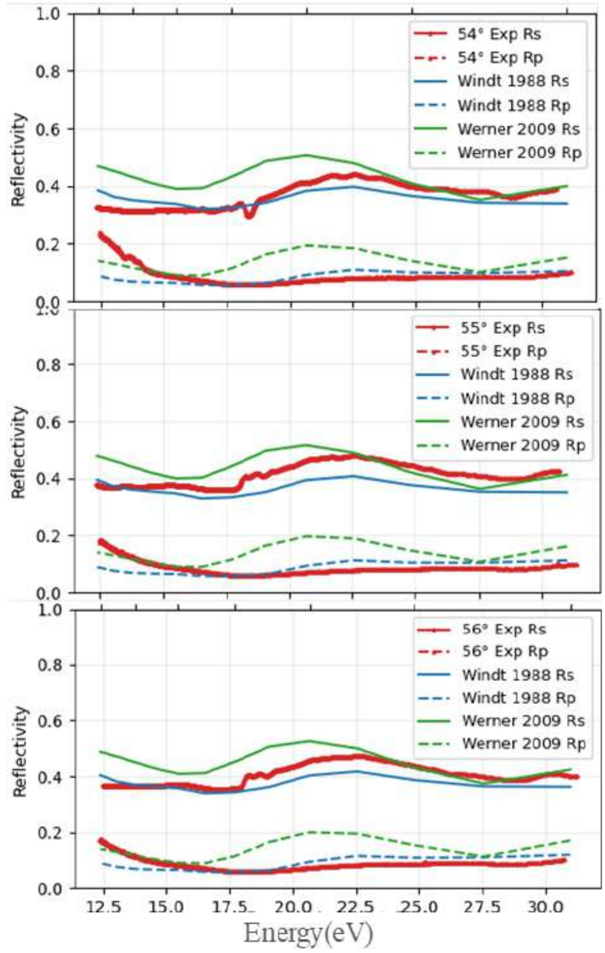

Fig. E.4.2: s and p- polarized x-ray reflectivity of Pt mirror measured at Indus-1 reflectivity beamline (BL-04) near the Brewster angle (54º, 55º and 56º) are shown along with earlier reported data from literature.

Courtesy: Savitha M S & K. Nagaraju, IIA, Bengaluru.

References:

[1] Wolfgang S.M. Werner et. al, Optical constants and inelastic electron scattering data for 17 elemental metals. J. Phys. Chem. Ref data 38. 1013-1092 (2009).

[2] David L. Windt et. al, Optical constants for thin films of Ti, Zr, Nb, Mo, Ru, Rh, Pd, Ag, Hf, Ta, W, Re, Ir, Os, Pt and Au from 24 to 216 Å. Applied Optics Vol. 27 No.2, 246-278 (1988).

Reported by:
Praveen Yadav (praveenyadav@rrcat.gov.in)

E.5: FPGA controlled bipolar power supply with integrated human machine interface

A FPGA controlled bipolar power supply rated at ±15 A / ±50 V has been designed and developed for magnetic characterization of the Indus accelerator magnets having wide range of time constants by the Accelerator Ramping Power Converter Section. Figure E.5.1 shows photograph of the power supply.

Fig. E.5.1: FPGA controlled bipolar power supply with HMI

The power stage of the power supply has an uncontrolled rectifier stage followed by an H-Bridge four quadrant converter switching at 50 kHz. The power supply has a FPGA based digital control with 64-bit floating-point architecture and HMI interface. Figure E.5.2 shows screenshot of the HMI panels.

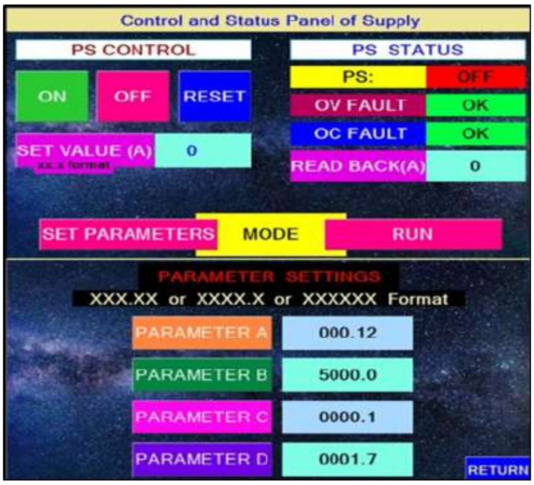

Fig. E.5.2: HMI control panels

The digital control has the provision to independently tune the control loop gains with a resolution of 0.01. This enables the power supply to adapt and cater to varying magnet loads of different time constants and provide exceptional control over system accuracy and response. This feature of power supply significantly eases the characterization of the magnets over the analog controlled power supplies, wherein the controller gains have to be physically adjusted by changing components on the PCBs. There is a provision to set these gains, monitor and control the power supply operation through a touch screen interface. Overcurrent and overvoltage protections have been implemented and a provision for an additional interlock is also provided in case any need arises during the operation. A custom software, GUI as shown in Fig. E.5.3, is also developed to compute the gain parameters for the power supply as per the magnet load parameters.

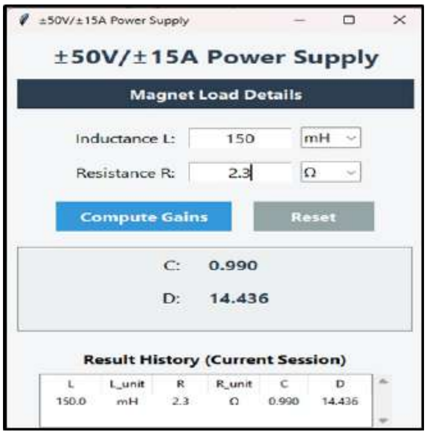

Fig. E.5.3: GUI of software for controller gains

The power supply was tested with different loads with time constants varying up to 4 times. Figure E.5.4 shows the stability data of the power supply, with a load time constant of 0.4 s, showcasing nearly ±25 PPM stability over 7 hours of operation.

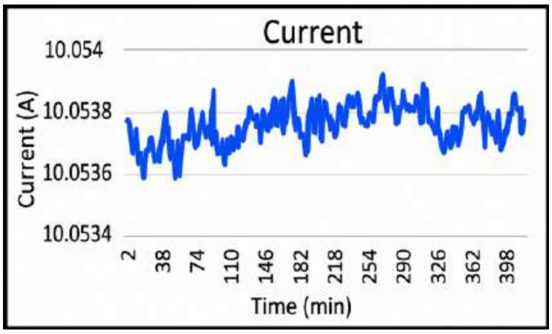

Fig. E.5.4: Load current stability over 7 hours

This power converter has been deployed at AMTD, RRCAT, Indore. Its modular, floating-point-based architecture is scalable to higher power levels and serves as a robust platform for future digitally controlled power systems being developed for the next generation particle accelerator at RRCAT.

Reported by:
Seema Singhai Sheth (singhai@rrcat.gov.in)

E.6: Development of an indigenous VME32 DAQ card for Fast Current Transformer interface

An indigenous, VME32-compliant DAQ card has been developed for pulse-by-pulse beam parameter measurement using FCT sensors for LINACs operating at a 300 Hz pulse repetition rate. This system is designed to capture e-beam data and extract parameters such as pulse width, height, and charge. The measured charge is utilized for beam power calculations, which are essential for dose calculation. To ensure reliable measurement, the board incorporates an automated in-application calibration mechanism that simulates e-beam behaviour using a dedicated calibration source.

Figure E.6.1 and E.6.2 shows the hardware and implementation scheme. The developed hardware is a VME32-compliant DAQ board designed for pulse-by-pulse beam parameter measurement using FCT sensors. The card is equipped with two signal processing chains, allowing it to interface with two FCT sensors simultaneously. Upon detecting a valid trigger, the board captures a beam pulse window and utilizes a 16-bit ADC to sample the signals at 125 MSPS. By performing a charge comparison between the two channels, the system can detect beam loss events and generate critical control signals to protect the machine hardware. The extracted pulse charge is further utilized for beam power and dose calculations. To maintain measurement integrity, the board integrates an FPGA and a MicroBlaze softcore processor to automate an in-application calibration process using a dedicated current source.

Fig. E.6.1: In-house developed VME32 FCT card

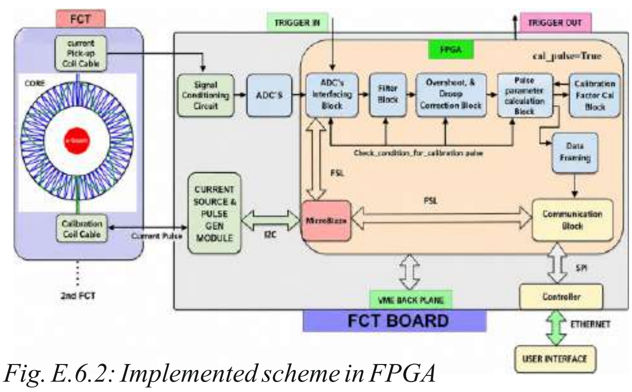

Fig. E.6.2: Implemented scheme in FPGA

Figure E.6.3 shows the measured electron beam pulse during field testing confirms that the system successfully removes high-frequency noise and restores the FCT pulse. The system software extracts/ calculated critical parameters, including pulse width and charge, on a pulse-by-pulse basis at a 300 Hz repetition rate.

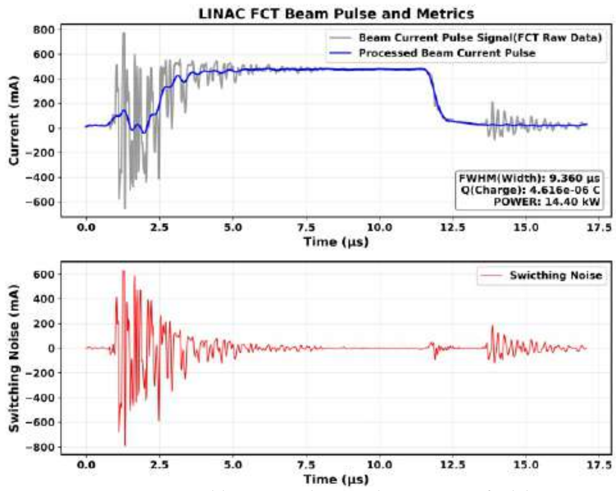

Fig. E.6.3: Measured beam pulse and metric in field

Figure E.6.4 shows a 10 ms communication snapshot of the data framing used to support the 300 Hz pulse repetition rate (PRR) within the limited bandwidth of the SPI bridge. To achieve this, a compression algorithm based on a band-pass filtering technique was implemented to group processed data into batches of three pulses per channel. These batches are subsequently framed into a unified data structure over a 400 ms scan cycle. Each frame includes these compressed pulse parameters—such as pulse width and charge—alongside a complete raw signal trace of the first pulse for verification.

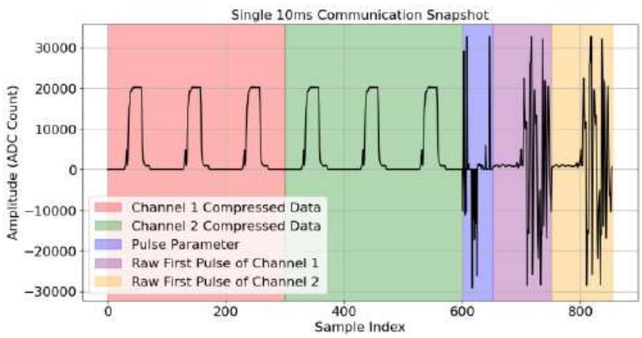

Fig. E.6.4: Communication snapshot of a 10 ms frame illustrating the grouping of 3-pulse compressed data and raw traces for two channels

Reported by:
R. P. Yadav (rpyadav@rrcat.gov.in)

E.7: Development of fast dipole magnet for IRFEL

A pulsed magnetic field is required to study the energy spread of electron beam within a macropulse in IRFEL. For this, a linearly rising magnetic field having an integrated magnetic field of 2000 G-cm to 3000 G-cm in the pole aperture is required. A field uniformity of 1×10^{-2} in good field region (GFR) ±10 mm must be achieved. To fulfill this requirement, a fast dipole (vertical kicker) magnet has been designed, developed, characterised and deployed in IRFEL.

The physical length of the magnet should be less than 42 mm due to limitation of available physical space along beam direction for the magnet. A window frame magnet geometry was chosen in order to be able to achieve the required integrated field and field uniformity. The magnet consists of Ni-Zn ferrite core and a single turn copper coil. The magnet design was carried out using opera 3D Elektra solver. Several 3D simulations have been performed and magnet parameters were optimized.

Figure E.7.1 shows the exploded 3D view of the magnet and its excitation coil. The magnet core is fabricated from Ni-Zn ferrite blocks. The excitation coil is single turn and it has been developed using ETP copper. It has provision to open and install it around the ceramic vacuum chamber without disturbing the chamber. The Cu coil conductors were insulated using Kapton tape. The magnet outer casing is developed from stainless steel. The ferrite core, copper coil and glass epoxy sheets have been assembled precisely into stainless steel casing. The achieved pole gap accuracy is ± 0.01 mm.

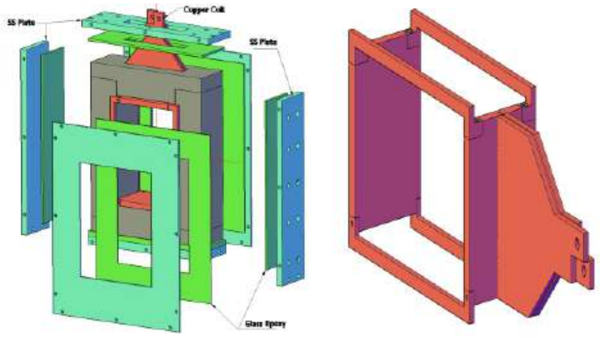

(a) (b)

Fig. E.7.1: a) Assembly view of the magnet, b) Single turn excitation coil of the magnet.

The magnet was excited by a linearly rising current pulse (8 - 8.5 us) of 2.8 kA peak and corresponding magnetic field was measured. The magnetic field measurements was carried out using search coil method. The search coil signal is measured using PC based 14-bit digitizer system and DSO. The search coil was precisely placed and moved in the pole aperture using 3-axis bench. Figure E.7.2 shows the measured current and magnetic field waveforms.

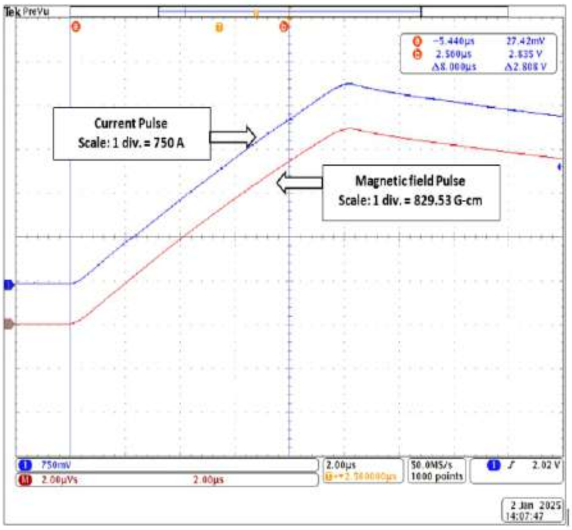

Fig. E.7.2: Measured current and magnetic field waveforms.

The fast dipole magnet installed in the IRFEL beam line and its power supply are shown in Fig. E.7.3.

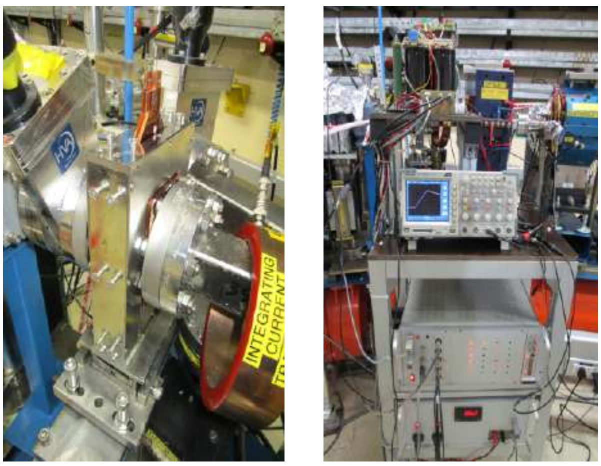

(a) (b)

Fig. E.7.3: The fast dipole magnet installed in IRFEL: a) Magnet, b) Magnet being energised.

The measured field uniformity is better than $\pm1.11\times10^{-2}$ over good field region (± 10 mm) which fulfills the requirement. The magnet installed in the IRFEL beam line.

Reported by:
Shesh Nath Singh (snsingh@rrcat.gov.in)

E.8: Panic button alarm system for Indus-2 beamlines personnel safety

In a significant step toward augmenting the safety infrastructure of the Indus-2 Synchrotron Radiation Source, an indigenously developed Panic Button Alarm System has been successfully commissioned across 24 beamlines. Designed as a fail-safe rapid-response mechanism for medical, fire, or radiation emergencies, the system ensures that critical assistance is only a button-press away for beam line scientists, researchers and other staff. By providing immediate audio-visual alerts to the Indus control room, security posts and first aid centre, the system facilitates rapid activation of the response in case of any emergency at the beamlines, significantly enhancing the safety and security architecture of the Indus-2 facility.

System Overview

Developed as per recommendations of the Safety Review Sub-Committee' for Indus and EAG activities, the system features 24 strategically placed panic boxes (Fig. E.8.1) at the beamline hutch entries. The architecture as shown in Fig. E.8.2 is built on "Fail-Safe" principles, utilizing three parallel redundant cables to ensure that the system remains functional even in the event of physical cable damage. Furthermore, the entire network is supported by an Uninterrupted Power Supply (UPS), guaranteeing performance during power fluctuations or outages.

Fig. E.8.1: Panic Button Boxes (BL-1 to24)

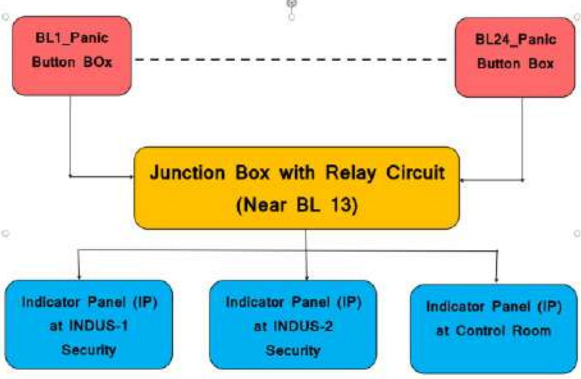

Fig. E.8.2: Block diagram of Panic Button Alarming system

Strategically Located Indicator Panels (IP): To ensure zero-latency response, high-visibility Indicator Panels equipped with synchronized flashing lights and high-decibel audible alarms have been installed at three primary security and monitoring hubs:

- **Indus Control Room:** Mounted at the main entrance for immediate operator awareness.
- **Indus-2 Security Post:** Positioned on the left sidewall to alert security personnel.
- **Indus First-aid Centre:** Installed on the primary front wall to ensure immediate medical assistance

Fig. E.8.3: Indicator panel with audio/visual alarming

The IP is having 22mm dia EM lamps in a matrix form (Fig. E.8.3) with marking of Beam Line locations.

Each panel features a localized matrix of LED indicators, allowing responders to identify the specific beamline in distress at a glance. The internal wiring of junction box (Fig. E.8.4), which contains the relay logic, is located near BL13.

Fig. E.8.4: Internal wiring of junction box

Operational Workflow: From Trigger to Resolution

The system follows a synchronized four-stage protocol. An emergency is triggered by pressing a local mushroom top latch-type button located outside experimental hutch of each beamline of Indus-2, which immediately alerts the control room, security posts and first aid centre simultaneously with precise location mapping. An intuitive indicator panel allows to pinpoint the exact location of the emergency instantly, facilitating a rapid response to the emergency.

The commissioning of this system reinforces the commitment to a robust safety culture at the facility. By utilizing high-reliability components and a redundant signal architecture, the system provides a dependable safety net for the diverse operations conducted at the Indus-2 beamlines.

Reported by:
Lalita Jain (lalita@rrcat.gov.in)

P.1: Development of programmable standalone controller for bakeout & activation of hybrid UHV pump

Non-evaporable getter (NEG) coating technology for vacuum chambers was developed in UHV Technology Section for its application in vacuum systems of particle accelerator and storage ring. Ti-Zr-V NEG coating is a novel room temperature capture pump for achieving very low pressure down to extreme high vacuum (< 10^{-11} mbar). The primary advantage of Ti–Zr–V NEG thin-film coating is its passive pumping action, requiring no electrical power during operation once activated. NEG coating on Aluminium chamber can be fully activated by heating up to 180°C for around 24 hours. It pumps active gases (H_2O, CO, CO_2) by chemisorption and H_2 by diffusion. However, it is ineffective for pumping methane (CH_4) and inert gases. Combination of NEG and SIP, henceforth called hybrid pump overcomes this & deliver high pumping performance in an extremely compact design. Triode type SIP effectively pumps CH_4 and inert gases. Thus, the hybrid NEG+SIP configuration provides comprehensive gas species coverage required for accelerator-grade UHV systems. These hybrid pumps are highly reliable, long lasting and state of art UHV pumping solution for next generation synchrotron radiation sources and LIGO projects.

A prototype standalone compact single-channel heating controller, operable without the need for a PC, has been designed and developed for bakeout and activation of this hybrid pump (shown in Fig. P.1.1).

Fig. P.1.1: Photograph of the controller

The controller features an LCD & keyboard interface. Temperature monitoring is carried out using a K-type thermocouple sensor. Up to 1 kW heater control is achieved using an SSR in ON/OFF mode. The typical baking and activation cycle consists of five stages: RAMP-UP-1 to 100 °C, DWELL-1 for 24 hours, RAMP-UP-2 to 180 °C, DWELL-2 for 24 hours (NEG activation), and finally RAMP-DOWN to room temperature with controlled cooling.

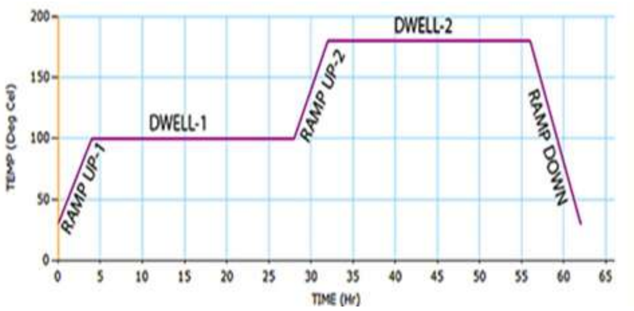

Fig. P.1.2: Typical cycle showing all states

The user can configure the controller for either single ramp or dual ramp and thus increasing its further scope of use.

The ATmega328 controller was used for overall control & supervision of the process. The thermocouple is interfaced with controller using MAX31855 ADC. This converter resolves temperatures to 0.25°C, and exhibits thermocouple accuracy of ±2°C, over the specified operating range of the K-type thermocouple.

The user can configure various settings like the dwell-temperatures, dwell times, slope, etc. Key features of the controller include:

1. Single button cycle start using pre-configured parameters stored in EEPROM.
2. Configurable hold state, allowing coordination with another connected system bakeout cycles to prevent premature NEG activation.
3. Automatic detection of open or reversed thermocouples, pausing the heating cycle until corrected.
4. Controlled set-point ramping that limits temperature to the user-defined slope, with dynamic cycle-time adjustment using the current temperature as the starting set-point to minimize total cycle time.
5. Power-failure recovery capability, wherein the cycle resumes from the last state upon restart, using the current temperature as the new initial set-point.

Various baking & activation cycles were conducted using this standalone controller. Further observation & upgradation are under process to enhance robustness and multi-channel capability.

Reported by:
Nilesh J. Bhange (bnilesh@rrcat.gov.in)

P.2. Optimization of NEG coating process for SWLS chamber of Indus-2: Findings of second experimental run

In the INDUS-2 storage ring, a Superconducting Wavelength Shifter (SWLS) is planned to be installed in the long straight section LS-4 to extract synchrotron radiation through the 0° port downstream of the dipole chamber for beamline experiments. The proposed aluminium alloy SWLS chamber is 1400 mm long with a racetrack cross-sectional profile of 20 mm × 100 mm. Due to the very low conductance of this narrow chamber and space constraints along its length, pumping using only lumped pumps at the ends is insufficient to maintain the required vacuum level in the central region. To address this limitation, distributed pumping using a Ti–Zr–V non-evaporable getter (NEG) coating of approximately 1 µm thickness has been proposed. NEG coatings provide distributed pumping, reduce outgassing rate, and enhance vacuum performance. As part of coating process optimisation study, the second experimental run was undertaken to study the effect of increased sputtering power on film microstructure, elemental composition, and coating duration required to achieve the target thickness.

NEG-coated chambers and flat aluminium samples were coated using an in-house cylindrical DC magnetron sputter deposition system. Intertwined Ti–Zr–V wires of 1 mm diameter were used as cathodes. Considering the racetrack cross-section of the vacuum chamber, three targets were employed to minimize thickness non-uniformity along the perimeter [1]. Thickness uniformity along the chamber length and periphery was studied with the first experimental run carried out last year. Flat aluminium samples of size 10 mm x 30 mm were simultaneously coated for characterization purposes. Surface morphology and chemical composition were analyzed using scanning electron microscopy (SEM) and energy dispersive spectroscopy (EDS), respectively.

The deposition parameters for the second experimental run are listed in Table P.2.1.

Table P.2.1: Deposition Process Parameters

Process Gas	Kr
Target	Ti -Zr -V
Sputtering Power (W)	100
Solenoid Current (A)	90
Coating Duration (hrs.)	9

With 100 W sputtering power, a deposition rate of 19 Å/min was achieved. In comparison, the first run was conducted at 55 W and yielded a deposition rate of 9.8 Å/min. The increase in deposition rate with sputtering power is attributed to the higher discharge current and increased number of atoms ejected from the target.

SEM analysis of samples coated in the second experimental run is shown in Figure P.2.1. The films exhibit a cauliflower-type morphology (similar to first run) but with comparatively larger grain size than those obtained in the first run (Figure P.2.2).

EDS analysis was performed on coated aluminium samples to determine elemental composition. The measured atomic percentages were: Ti: 37%, Zr: 23% and V: 40%.

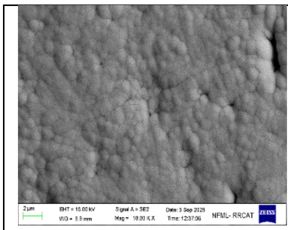

Fig. P.2.1: SEM of 2nd Experimental run

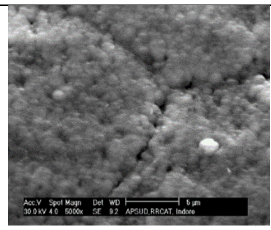

Fig. P.2. 2: SEM of 1st Experimental run

Figure P.2.3 shows the representative EDS spectrum. The measured composition falls within the suitable range for low-temperature activation (~180°C), meeting the requirements of INDUS-2 aluminium vacuum chambers.

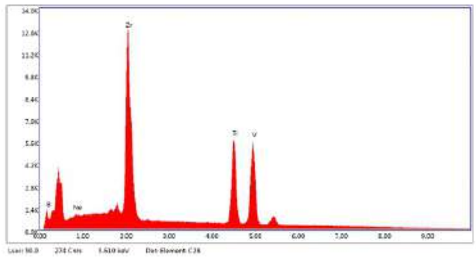

Fig. P.2.3: EDS spectrum of DC Magnetron sputter coated TiZrV film on Aluminium sample

Vacuum performance of 350 mm long SWLS-profile NEG-coated chambers was evaluated using a 35 l/s sputter ion pump. After activation at 180°C, an ultimate pressure of 2×10^{-10} mbar and a CO partial pressure of 3×10^{-11} mbar were achieved, demonstrating effective distributed pumping.

Results indicate that increasing sputtering power improves deposition rate but leads to increased grain size due to higher adatom mobility. Comparative analysis of the first and second runs suggests that lower sputtering power is more suitable for producing finer-grained NEG films desired for enhanced pumping speed.

The effect of increased sputtering power and gas flow rate on NEG coating characteristics was investigated during the second experimental run. Higher power resulted in increased deposition rate and larger grain size, while the elemental composition remained within the desired range. Effective ultra-high vacuum performance was achieved after activation. The study indicates that lower sputtering power is preferable for obtaining finer-grained NEG coatings. Further experimental run will focus on the repeatable performance of the coating process.

The technical support and expertise for SEM and EDS analysis by PMTS team is duly acknowledged.

Reported by:
Tripti Bansod (tripti@rrcat.gov.in)

P.3: Development of the β=0.47 Single Spoke Resonator (SSR-2) Superconducting RF cavity

The development of the 325 MHz Single Spoke Resonator-2 (SSR-2) bare cavity represents an important milestone in superconducting RF engineering. Successfully produced at RRCAT in collaboration with CDM, BARC, this component is intended for Fermilab under the Indian Institutions and Fermilab Collaboration (IIFC) for the PIP-II project. The SSR-2 cavity is optimized to accelerate medium-velocity protons via superconducting technology, offering superior performance for accelerator systems. Its development process utilized precision fabrication of high-purity niobium parts and sophisticated electron beam (EB) welding to achieve structural integrity and electromagnetic excellence within rigorous and highly demanding technical specifications.

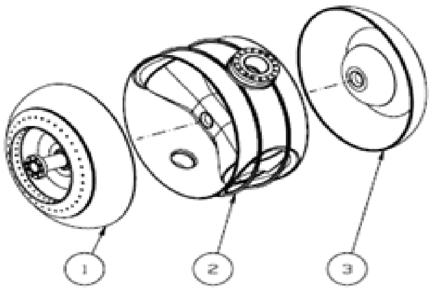

Fig. P.3.1: SSR-2 Cavity sub-assemblies: 1) End wall left, 2) Shell-spoke assembly, 3) End wall right

Material Specifications

The SSR-2 cavity operates at 325 MHz with a geometric beta (β) of 0.47, designed specifically for medium-velocity proton acceleration. The cavity structure comprises two end walls along with a shell containing spoke, which creates accelerating gap (figure P.3.1). The fabrication utilized high-residual-resistivity-ratio (RRR ⩾ 300) niobium sheets, critical for maintaining superconducting properties. The main beam tube and side port flanges were manufactured from Titanium Grade-5, while transition regions employed Titanium Grade-2, optimizing both structural strength and thermal conductivity at cryogenic temperatures.

Fig.P.3.2: Various components of SSR-2 cavity

Manufacturing Process

The manufacturing sequence employed high-precision machining followed by BCP to remove 20 µm of surface material, ensuring a contaminant-free weld edge. The cavity was assembled using EBW across multiple joints, including Nb-Nb full-penetration welds of varying thicknesses (4.75 mm, 4.0 mm, and 3.2 mm) and dissimilar metal joints (13 mm and 6 mm) as shown in figure P.3.2 and P.3.3. After completing the conical stiffening ring and spoke EBW, the assembly underwent rigorous MSLD to verify vacuum integrity and joint reliability.

Fig. P.3.3: SSR-2 Cavity assembly after final EB welding

Qualification and Performance

The completed SSR-2 cavity underwent comprehensive post-fabrication qualification testing. MSLD confirmed vacuum integrity with a measured leak rate of $\leqslant 5\times10^{-11}$ mbar·l/s, well below the FNAL requirement of $\leqslant 1\times10^{-10}$ mbar·l/s. RF characterization measurements performed at room temperature (300K) demonstrated a resonant frequency of 324.71 MHz with a quality factor exceeding 8200, confirming dimensional accuracy post-fabrication. Field flatness evaluation via bead-pull technique revealed >98% uniformity, indicating excellent electromagnetic field distribution within the accelerating region. These results validate the manufacturing methodology and confirm the cavity's readiness for subsequent surface treatment and superconducting operation.

Summary

The integration of precision engineering, rigorous quality assurance, and innovative repair strategies demonstrates a comprehensive approach to complex superconducting cavity manufacturing. Future production units will benefit from lessons learned regarding shell circularity control and pre-weld machining allowances, further optimizing manufacturing consistency and reducing dimensional deviations.

The machining support for finalizing joints carried out by DMTD team and RF measurement by RFSD team.

Reported by:
Manish Bagre (manish@rrcat.gov.in)

P.4: Commissioning of test cryostat for qualification of superconducting magnets

Superconducting insertion devices are under development at RRCAT as part of ongoing Indus-2 upgradation program. This also serves as a vital technological foundation for the state-of-the-art insertion devices required by the proposed High Brilliance Synchrotron Radiation Source (HBSRS). The development of Superconducting Wavelength Shifter (SWLS) and Multi-Pole Wiggler (MPW), both having superconducting magnets at their core, is in advanced stages. A liquid helium (LHe) pool type cryostat for the qualification of superconducting magnets is one of the critical requirements for the development of these insertion devices.

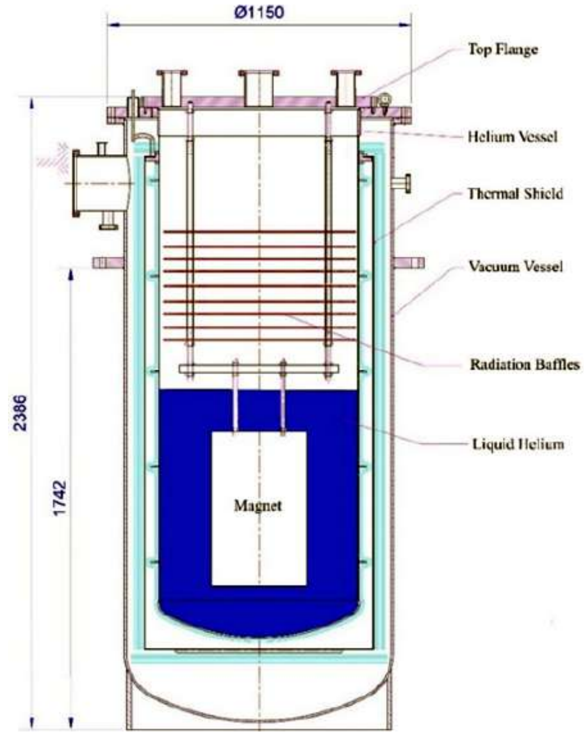

Fig. P.4.1: Dimensional Schematics of the cryostat

Magnet test cryostat consists of three thermal boundaries viz, vacuum vessel at room temperature, helium vessel at 4.2 K and an intermediate LN2 cooled thermal shield at 80 K. A 10-layer Multi-Layer Insulation (MLI) wrapping on helium vessel and 30-layer MLI wrapping on thermal shield are provided for reducing radiative heat leak. Insert assembly for placing the magnets in LHe pool, consist of top cover, magnet suspension rods, radiation baffles and helium gas displacer foam. Cryostat was designed in-house at RRCAT and fabricated by an Indian manufacturer. Cryostat was interfaced with the existing cryogen transfer line and helium recovery systems and successfully commissioned by cooling it down to 4.2 K temperature followed by collection of liquid helium. Superconducting joints immersed in the LHe pool were tested and successfully qualified in the cryostat.

Fig. P.4.2: (a) Test Cryostat, (b) Insert assembly.

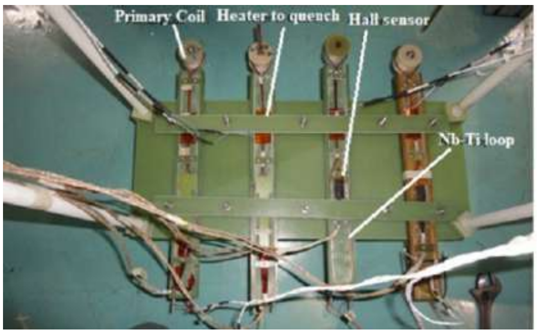

Fig. P.4.3: Measurement of Sc joint resistance.

For the measurement of SC (Nb-Ti) wire joint resistance, a system is created using a primary coil (1500 turns, L~25.6 mH) that is mutually coupled with a secondary loop of Nb-Ti wire (2 turns, L~1.3 H), with the loop ends joined through ultrasonic welding. Four such joints are made and placed inside the cryostat. The primary coil is energized with 1- 4 A DC current keeping the SC loop in resistive state using a heater connected to it. When the primary current reaches to a peak value, the heater is switched off to make the SC loop to reach into superconducting state. Once the SC loop becomes superconducting, the current of the primary coil is suddenly switched-off, thus an induced current is generated in SC loop which is read by the Hall sensor placed in the middle of SC NbTi loop. By knowing the exponential decay of Hall voltage with respect to time and the known value of the inductance of NbTi loop, the resistance of ultrasonic welded wire joint is calculated. The maximum values of the joint resistances are found in the range of 1.9 n (multiple overlap joints) to ~5 n (single overlap joint)

Reported by:
Nidhin. S. L (nidhin@rrcat.gov.in)

P.5: Development of a 3D computer code to study space charge induced multipacting current saturation in superconducting RF elliptic cavities

Design and development of superconducting elliptic RF cavities at RRCAT have progressed significantly in recent years. Several cavities have achieved the design accelerating gradients during the powering experiments conducted at the Vertical Test Stand (VTS). During VTS tests, it is sometimes observed that at a particular accelerating gradient, even when additional RF power is supplied, the gradient does not increase further. At this point, the quality factor drops significantly, along with observation of increased x-ray emission. This condition occurs due to multipacting, where the cavity surface produces a large number of secondary electrons whose motion between successive surface impacts is resonant with oscillation of RF field. The multipacting electrons repeatedly strike the cavity surface, resulting in exponential growth in the electron population. The electrons absorb a large amount of RF energy form the cavity, and deposit it as heat, thereby creating local hotspots on the cavity surface, which often lead to quench. Since multipacting is detrimental to cavity operation, it should preferably be mitigated at the RF design stage itself, by suitably modifying the cavity geometry.

To gain deeper insight into this phenomenon in superconducting elliptic cavities, dedicated computer code is needed. Traditionally, in numerical simulations of multipacting, multiple seed electrons are initialized within the cavity and tracked for several RF cycles. When the seed electrons strike the cavity surface, new secondary electrons are emitted according to the secondary emission model used in the simulation code. After a few initial RF cycles, if the electron population grows exponentially over successive cycles, multipacting is considered to be present. In the absence of multipacting, the electron population decays. These simulations are repeated over a range of accelerating gradients to identify multipacting prone gradient ranges. However, the typical analysis does not account for realistic scenario experienced by multipacting electrons, such as electrostatic repulsion among multipacting electrons (space charge effects) and RF loading induced by the multipacting current. These effects lead to saturation of multipacting charge after an initial growth. In order to assess the severity of multipacting, it is important to evaluate the saturated multipacting charge.

In this work, we focused on the less-explored problem of space charge induced saturation of multipacting, by including space charge in an in-house developed 3D code. This code computes the electrostatic repulsion within the multipacting bunch by solving Poisson's equation using a finite-difference method. To advance particles in the 3D space, the code employs an RK4 particle pusher. The code includes boundary effects, which are important in our case because multipacting trajectories lie very close to the cavity surface (~1 mm), as shown in Figure P.5.1. For improved accuracy, the code uses a smooth cavity boundary representation instead of a staircase approximation. The developed code was used for multipacting simulations following a rigorous mesh optimization study. The time evolution of multipacting charge at 12 MV/m is shown in Figure P.5.2(a). The results show that the number of particles increases exponentially at the beginning because the electron population is small and mutual repulsion among them is weak. As the population increases, space charge repulsion becomes stronger, leading to many particles getting pushed out of synchronization and lost. Eventually, a saturated state is reached where particle loss per RF cycle equals the number of particles generated in the secondary emission process. The in-house code was benchmarked against CST-PIC, as shown in Figure P.5.2(b), and demonstrated better convergence. The developed code was subsequently used to estimate the saturated multipacting current over a range of accelerating gradients.

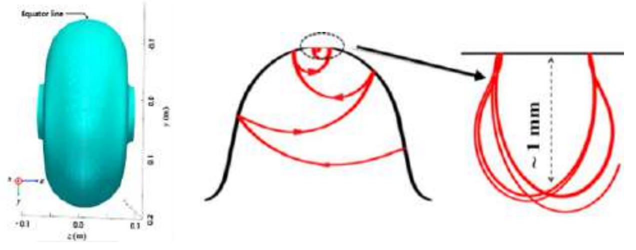

(a) (b)

Fig. P.5.1: (a) 3D view of the single cell of the β_g= , 650 MHz elliptic cavity, and (b) a sample particle trajectory corresponding to the 2-point 1st order multipacting shown on a 2D plane in the elliptic cavity.

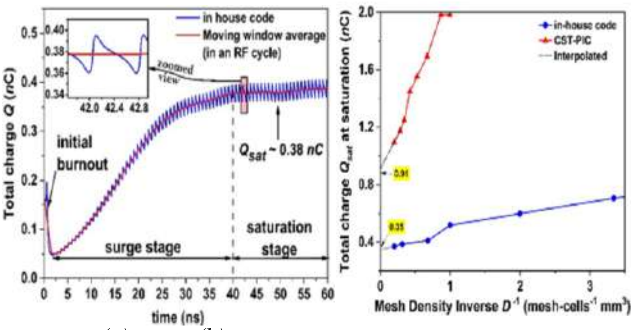

(a) (b)

Fig. P.5.2: (a) Saturation of multipacting charge due to space charge effects at the gradient of 12 MV/m. (b) Comparison of the results from the in-house developed code and results from CST-PIC.

Development of this code improves our physical understanding of multipacting and strengthens our efforts toward developing indigenous computational tools as a reliable alternative to imported commercial software.

Reported by:
Ram Prakash (rprakash@rrcat.gov.in)

P.6: Absorbing material development for RF and Microwave systems

Electromagnetic interference (EMI) and electromagnetic compatibility (EMC) represent significant challenges in contemporary high-power Radio-Frequency (RF) systems. As RF power levels increase, unintended radiation and signal reflections can adversely affect system performance, induce instability, and disrupt the operation of adjacent electronic devices. Electromagnetic absorbing materials offer an effective mitigation strategy by attenuating stray electromagnetic waves. These materials are essential for ensuring compliance with EMI/EMC standards and for maintaining the stability of RF amplifier systems. However, conventional microwave absorbers are often bulky and exhibit limited efficiency due to suboptimal impedance matching. This limitation has motivated the development of advanced magneto-dielectric composites, which provide advantages such as reduced weight, mechanical flexibility, and enhanced broadband absorption, making them highly suitable for applications in electromagnetic shielding, anechoic test chambers, and RF amplifier integration. This work was carried out under a BRNS-funded project through a collaborative effort between CMET Trissur (MeitY) and RRCAT, highlighting the strength of interdisciplinary and inter-institutional cooperation. The project was successfully completed in December 2025 and received favorable evaluation and commendation from the BRNS review committee, underscoring its technical merit and application relevance.

This article presents a magneto-dielectric composite absorber laminate engineered for EMI/EMC mitigation in RF systems. The composite incorporates carbonyl iron, barium hexaferrite, and polyaniline within a silicone matrix to achieve combined magnetic and dielectric loss mechanisms. Surface functionalization of the fillers using silane coupling agents enhances interfacial compatibility, environmental stability, and hydrophobicity. Barium hexaferrite was synthesized via solid-state reaction and sintering, followed by nanoscale size reduction through ball milling at CMET Thrissur (Fig. P.6.1)

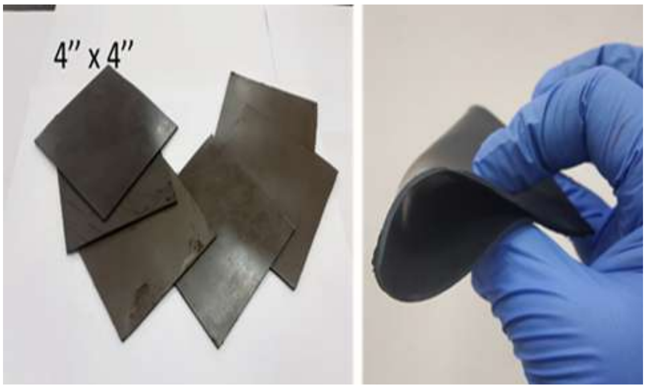

Fig. P.6.1: The developed microwave absorber

Polyaniline was prepared by oxidative polymerization. The silane-treated fillers exhibited improved dispersion within the matrix. Composite laminates were fabricated using controlled mixing, two-roll milling, and thermo-lamination, resulting in uniform and structurally robust materials.

The laminates were characterized using XRD, Raman spectroscopy, SEM, and IR analysis to confirm structural integrity and surface modification. Its electromagnetic performance was evaluated using an automated RF test bench (Fig.P.6.2). Two identical 1-5/8″ EIA coaxial airline test jigs were designed and fabricated, with the absorber sample positioned between them for measurement. The average insertion loss (S21) and return loss (S11) were measured as 0.35 dB and 23.53 dB, respectively, over the DC to 4 GHz frequency range. High-power RF characterization was conducted using indigenously developed solid-state amplifiers. The calculated absorption exceeded 88%. The material exhibited no signs of degradation under both low-power and high-power excitation. During high-power operation, the sample temperature remained stable in the range of 28–30 °C, indicating good thermal stability.

Fig. P.6.2: Automated RF Test bench for testing absorber sample at high power

This work demonstrates the potential of advanced composite materials to significantly enhance the reliability and operational stability of RF and microwave systems while effectively mitigating electromagnetic interference across diverse RF applications within DAE environment. The proposed approach offers a robust and scalable solution for EMI/EMC management, with clear advantages in terms of performance, adaptability, and material efficiency. Furthermore, the developed composites exhibit strong potential for deployment in both defense and commercial sectors, where stringent electromagnetic compliance and high-power handling capabilities are critical.

Reported by:
Akhilesh Jain (ajain@rrcat.gov.in)

P.7: Installation and commissioning of compact Digital Low Level RF System for RF stations 5 & 6 of Indus-2

The Digital Low Level Radio Frequency (DLLRF) system is crucial part of the RF accelerating system in a synchrotron radiation source. In the Indus-2 storage ring, precise control of cavity voltage amplitude and phase at 505.8 MHz is essential for maintaining longitudinal beam stability, minimizing synchrotron oscillations, and ensuring reliable injection and stored beam operation. The DLLRF system continuously senses the cavity field, compares it with a reference, and dynamically corrects deviations through high-speed digital feedback implemented in FPGA hardware.

During the long shutdown period of December 2025- January 2026, a compact upgraded DLLRF system was installed and commissioned for RF Stations 5 and 6 of Indus-2. The upgrade involved replacement of discrete units with a compact and indigenously developed RF signal processing, automated synchronization features and enhanced protection mechanisms. The complete installed system is shown in Fig. P.7.1.

Fig. P.7.1: Compact DLLRF for Station 5 & 6 Installed in Indus-2

The cavity pickup signal at 505.8 MHz is first down-converted to an intermediate frequency (IF) of 21.075 MHz. For this purpose, a local oscillator (LO) frequency of 526.875 MHz is generated by the LO & Clock generation unit. The down-converted IF signal is digitized using high-speed ADCs, and digital IQ sampling is implemented within the FPGA.

In-phase (I) and quadrature-phase (Q) components are processed through a CORDIC algorithm to determine instantaneous amplitude and phase of the cavity field. Detected amplitude and phase are compared with the reference set values and Proportional – Integral (PI) controller is implemented in FPGA to generate the correction signals using DAC. This correction signal is up converted using I/Q modulator that drives RF amplifier and subsequently to the accelerating cavity, thereby closing the feedback loop and maintaining the required stability.

Key feature of the upgraded system is the integration of indigenously developed multi-channel up-down converter modules with high dynamic range and low phase noise performance. The LO & Clock unit, also developed indigenously, provides automated programming capability and synchronized clock distribution. This ensures low phase noise reference generation and flexible configuration. Digital filters are implemented in FPGA to suppress noise components present in the reference signals. This has significantly improved the amplitude and phase stability (Fig. P.7.2).

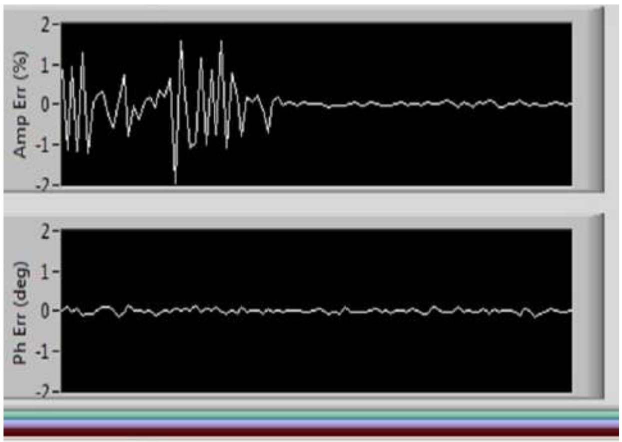

Fig. P.7.2: Screenshot of DLLRF GUI showing improved Amplitude error with filter switching

To ensure the operational safety, system reliability and enhanced fault detection capabilities a redundant interlock system and multi-channel power monitoring boards have been installed along with the DLLRF upgrade. These boards, developed indigenously, are capable of monitoring forward power, reflected power, cavity sense power, and reference power through multiple channels. It also has a pair of RF switches to enable rapid isolation of the drive in case of abnormal conditions. Few firmware upgradations have also been carried out including the calibration and auto synchronization feature.

The successful commissioning of the compact DLLRF systems for RF Stations 5 and 6 demonstrates improved amplitude and phase stability, enhanced noise immunity, updated firmware and strengthened protection mechanisms. The indigenous development of the up/down converter units, LO & Clock board, interlock modules, and monitoring electronics represents a significant technological achievement.

Reported by:
Nitesh Tiwari (nitesh@rrcat.gov.in)

L.1: Development of GaAs detectors for fast response hard X-ray detection

High-speed detection of hard X-rays requires higher-Z materials such as GaAs to meet the competing demands of high X-ray absorption and fast response. Owing to its higher absorption coefficient, GaAs requires a much smaller thickness than silicon for the same absorption, reducing carrier transit time and enabling faster response. Figure L.1.1(a) shows the electron transit times in Si and GaAs for X-ray energies from 10 to 30 keV, assuming 90% absorption, justifying GaAs-based hard X-ray detectors with nanosecond response. In this context, the Semiconductor Lasers and Devices Division, RRCAT, has already demonstrated GaAs p-i-n X-ray detectors, where the X-ray response is maximum at around 12 keV. [1] At higher energy, the response falls because of decrease in absorption coefficient. Thus, to extend the measurable X-ray energy range, a thicker absorption region is required. Accordingly, detectors based on a 350 µm-thick semi-insulating (SI) GaAs have been developed with optimized planner Ohmic contact and circular Schottky contact of diameter 2 mm on either side of GaAs. Prior to metallization the semiconductor is thoroughly cleaned chemically. Ohmic contact is made with sequential deposition of Au-Ge/Ni/Au followed by rapid thermal annealing at 450 °C. On the other hand, Schottky contacts of diameter 2 mm are made using Ti/Au metallization through a shadow metal mask. [2] Figure L.1.1(b) shows the detector mounted on a custom-designed printed circuit board. Reverse-bias measurements up to 100 V yield a leakage current of 15 nA at room temperature, which reduces to 0.8 nA at 280 K (Fig. L.1.2c and inset). A total of six such detectors are made with all of them showing room temperature leakage current below 15 nA.

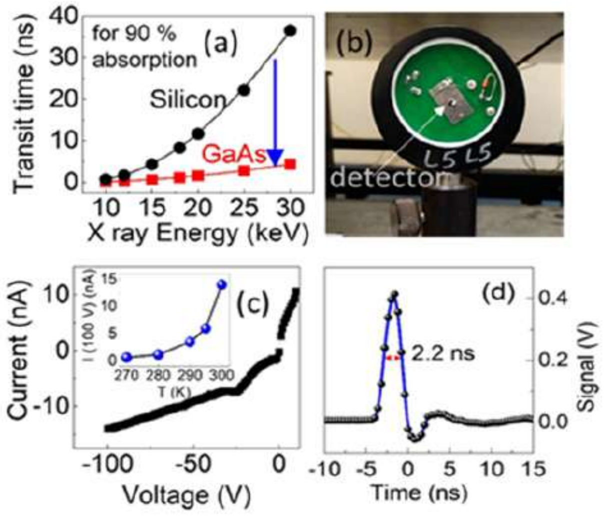

Fig. L.1.1 (a) Electron transit time in Si and GaAs Vs X-ray energy, (b) Photograph of mounted detector, (c) Room temperature I-V of the detector and leakage current as a function of temperature, (d) Temporal response of the detector

The detector operational properties are readily assessed using visible and near-IR illumination. A peak responsivity of 0.15 A/W at 870 nm, along with a spectrally flat response in the 600–800 nm range, is observed, which is typical for GaAs-based photodetectors. To measure the temporal response of the detector, a readout circuit is developed and the voltage signal is measured across 100 Ω resistance using a fast oscilloscope following incidence of Ti:Sapphire femtosecond laser pulse (pulse duration ~35 fs). The detector response was measured to be 2.2 ns, as shown in Fig. L.1.1(d), validating the fast carrier extraction capability of the device. The temporal response for X-ray detection is expected to be similar.

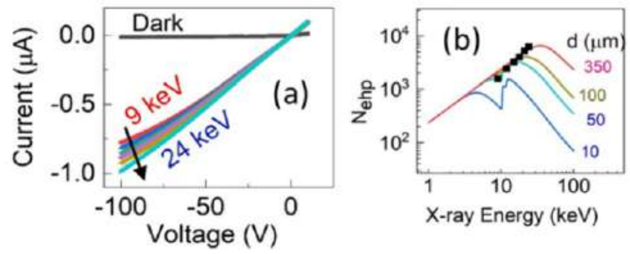

Fig. L.1.2 (a) I-V in dark and in presence of X ray with increasing energy, (b) Comparison of normalized current (black dots) with calculation (solid lines), N_{ehp} is the total number of electron hole pair created under x-ray illumination.

The detector response in the 9–24 keV range was measured in 3 keV steps at beamline-4 (imaging beamline) of Indus-2. A key observation is that at 9 keV the signal magnitude saturates at high bias, whereas at 24 keV it increases linearly with voltage. This is explained by invoking the partial absorption of 24 keV X–ray within the depletion region. [2]

The spectral response of the detector is estimated by normalizing the current at 100 V for each X-ray energy with respect to the measured flux at that energy. In Fig. L.1.2b, these normalized results are shown and the magnitude of signal is observed to increases with X-ray energy. The calculated spectral responses for detector with different thickness are also plotted as solid lines for direct comparison. [2] In summary, we have developed and characterize GaAs based hard X-ray detector operating in the energy range of 9 to 24 keV, which has a time response of 2.2 ns. Cooling of the device by ~30 °C is shown to further improve the device performance.

References:
1. Geetanjali et al., Nucl. Inst. Meth. Phys. Res. A, 1084, 171184 (2026)
2. Harsh Tiwari et al., Proceedings of Solid-State Physics Symposium, IIT Roorkie-2025, p-74

Reported by
Shailesh K. Khamari (shaileshk@rrcat.gov.in)

L.2: Growth of Nd:$LuVO_4$ single crystals and demonstration of CW Lasing

The rare earth doped $LuVO_4$ crystal shows excellent lasing property due to its higher absorption at pump wavelength and larger emission cross-section in comparison to the other orthovanadate (YVO_4 and $GdVO_4$) crystals. It also exhibits high damage threshold and better thermal properties. Particularly, Nd-doped $LuVO_4$ is considered as one of the excellent laser materials for generating laser emission near 1 μm.

In the present work, single crystals of 0.5 at% Nd doped $LuVO_4$ were grown by optical floating zone (OFZ) method using the [100]-oriented seed. The growth rate was optimized and kept 12-15 mm/h for obtaining good quality crystal. During the growth of the single crystals, a mixture of 20% of O_2 and 80% of N_2 was used at a flow rate of 1 l/min (LPM). Crystals of length ~15-30 mm and diameter 4-6 mm were grown (Fig. L.2.1(a)). The rocking curve of (200) plane exhibited a FWHM of ~130 arc-sec, and the nearly straight fringes observed in the birefringence pattern (Fig. L.2.1(b)) further confirmed the good crystalline quality.

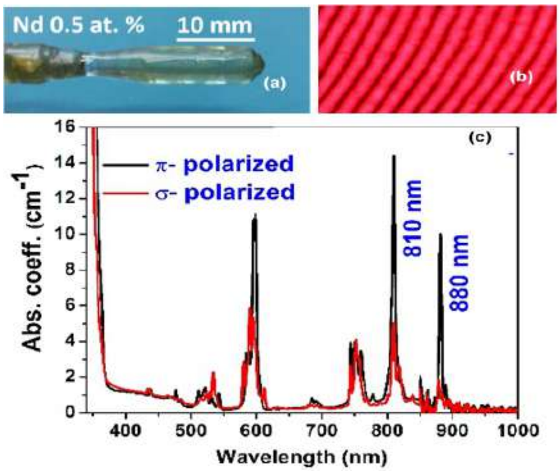

Fig. L.2.1 (a) Photograph of an as-grown crystal, (b) Birefringence pattern, (c) Absorption spectra.

Further, optical absorption was found to be polarization sensitive with higher absorption coefficient for π–polarized light. The coefficient at 810 nm is ~14.8 and 5.1 cm^{-1} for π- and σ- polarization, respectively (Fig. L.2.1(c)). Emission spectra for excitation at 810 and 880 nm resulted peaks at ~916, 1065, 1087 and 1342 nm with highest emission intensity for 1065 nm (Fig. L.2.2).

Further, 'a'([100])-oriented laser elements of dimension ~4x4x7 mm^3 were fabricated [inset of Fig. L.2.3] from the grown crystals using Laue diffraction pattern (inset of Fig. L.2.3). The [100] direction was chosen as vanadates exhibit better absorption and emission characteristic along this direction.

These elements were precisely polished, achieving surface parallelism within 20-40 arc-seconds. Subsequently, to relieve the mechanical stress induced during cutting and polishing and to mitigate oxygen vacancies, the elements were annealed at 1100°C for 24 hours in a flowing oxygen atmosphere at 1 LPM. To minimize cavity losses, an anti-reflection (AR) coating of SiO_2, optimized for 808 and 1065 nm, was applied on both the entrance and exit faces using the Ion-assisted electron-beam evaporation.

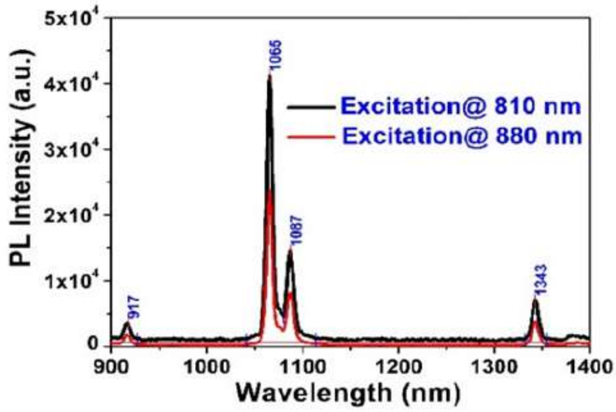

Fig. L.2.2: Emission spectra of 0.5 at% Nd:$LuVO_4$

To demonstrate the laser performance, a plane-parallel resonator with a cavity length of 35 mm was designed. Testing of lasing was conducted using an 808 nm diode laser as a pump source, along with an output coupler mirror with 89% reflectivity. Continuous-wave (CW) laser emission at 1065 nm was achieved, delivering an output power of ~10 W with a high slope efficiency of ~48.5%.

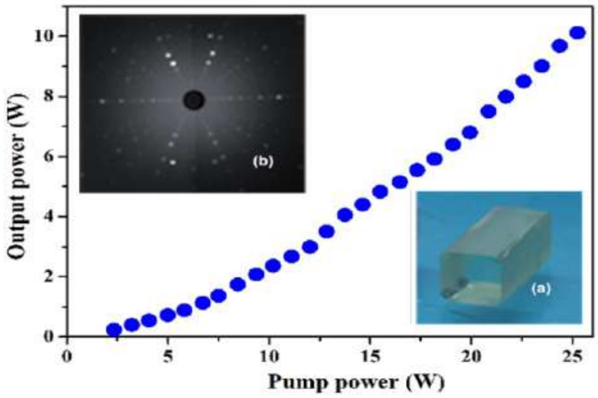

Fig. L.2.3: Laser output [Inset: (a) A fabricated laser element and (b) Laue pattern].

This work is significant for the development of diode pumped compact solid-state laser used for marking and engraving applications. This crystal also has a potential use in the laser ignition systems for Indian space programme.

Reported by:
Mohammad Soharab (sohrab@rrcat.gov.in)

L.3: Development of 7x1 pump combiner for high power fiber laser pumping

Fiber lasers are the state-of-the-art solid-state lasers having all fiber integration and compact foot print with lower thermal problems and single mode output. It consists of rare earth doped double-clad fiber as the gain medium, which is end pumped by fiber coupled laser diodes and in-line fiber Bragg grating mirrors form laser resonator. As gain fiber has two free ends, it can be end pumped from both sides. However, pumping is limited by available pump power from single diode laser. Thus, for power scaling of fiber lasers, output power from several fiber coupled diode lasers is combined using Nx1 or (N+1)x1 pump and signal combiner. Thus, pump combiners are important passive fiber optic components for high power fiber laser development. In this direction, a fiber optic pump and signal combiner fabrication facility has been created and using this facility 7x1 pump combiners having 7 No. of pump input ports and one output port has been developed.

Fabrication of fiber optic pump combiner involves following steps: 1) Fiber preparation, 2) Bundle formation/fiber stacking, 3) Tapering of bundle, 4) Cleaving of tapered bundle, 5) Splicing with output fiber, and finally 6) Recoating and thermal packaging of the combiner for integration with fiber laser. For achieving higher transmission efficiency from pump combiner, brightness needs to be conserved during evolution from N input beams to single output beam. The brightness conservation is described by the ratio of integrated brightness of the total input of a pump combiner to the total integrated brightness of the output beam and is given by:

$$D_{out}^2 . NA_{out}^2 \geq N . D_{in}^2 . NA_{in}^2$$

where, D_{in} and D_{out} are core diameters of input and output fibers; NA_{in} and NA_{out} are numerical aperture of input and output fibers; and N is the number of input fibers. Figure L.8.1(a), (b), (c) and (d) show cross-section of 7x1 fiber bundle, schematic of fiber tapering and cleaving, 7x1 combiner cross-section after tapering and cleaving and splicing of cleaved tapered bundle with output fiber.

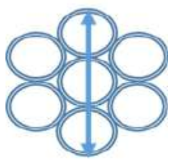

(a)

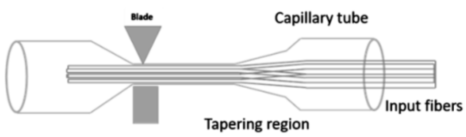

(b)

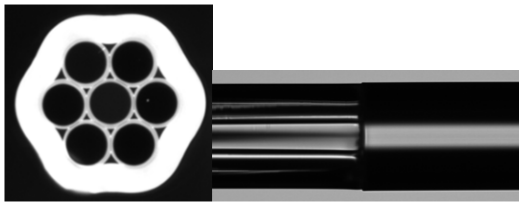

(c) (d)

Fig. L.3.1: (a) Cross-section of 7x1 fiber bundle, (b) schematic of fiber tapering and cleaving, (c) 7x1 combiner cross-section after tapering and cleaving, and (d) splicing of cleaved tapered bundle with output fiber.

Fabrication of a 7x1 pump combiner having 7 input pump input fibers each of 100/125 µm core/clad diameter and 0.22 NA and 20/400 µm double clad fiber with NA of 0.46 as the combined output port has been carried out using in-house fiber optic pump and signal combiner fabrication workstation facility for high power fiber laser activity. Process parameters such as taper ratio, taper length, fusion power, etc. were optimized for tapering of fluoride glass tube containing fiber bundle. Further, this pump combiner has been thermally packaged (Fig. L.3.2) for utilization in high power fiber laser. Laser diodes at 915 nm wavelength were spliced at the pump input ports of pump combiner and pump combiner was tested up to combined output power of 500 W (~70 W per pump port) with a pump combining efficiency of ~99.2%, which is close to reported in literature. Figure L.3.3 shows testing of pump combining efficiency of the fabricated pump combiner. Further optimization of pump combiner fabrication process for enhancement in number of pump input ports and pump power handling capability per port is underway.

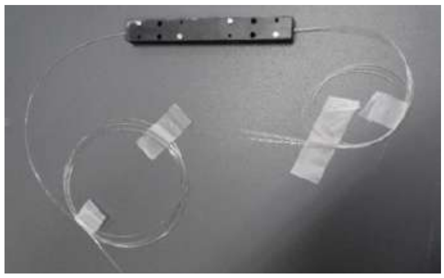

Fig. L.3.2: In-house fabricated thermally packaged 7x1 fiber optic pump combiner.

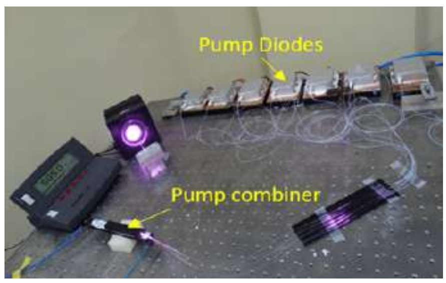

Fig. L.3.3: Testing of 7x1 pump combiner at 500 W of input pump power from 7 diodes.

Reported by:
B. N. Upadhyaya (bnand@rrcat. gov.in)

L.4: Ultrastable high harmonic generation from a semi-infinite gas cell with a thermally insulated exit endcap

High harmonic generation (HHG) is well known technique for generation of coherent and ultrashort extreme-ultraviolet (XUV) radiation. These unique characteristics enables the source to be used in wide areas of scientific research application. HHG is a highly nonlinear process, in which the characteristic of the radiation is crucially dependent on the interaction of ultrashort intense laser pulse with atoms in a nonlinear medium. Several nonlinear media, such as gas jets, small length cells, gas filled waveguides and semi-infinite gas cell (SIGC) etc., has been explored to achieve high flux, high coherence, good spatial profile along with small pulse width, which may extend to tens of attosecond. The study of source stability remains least explored. Several applications of this source, such as pump-probe experiments (for time resolved studies of ultrafast phenomena) need high source stability, together with high flux, however the source stability remains a prime criterion. We present our study on HHG from a SIGC with a prime focus on achieving ultrahigh stability (rms stability ⩽ 1%) together with high photon flux. Due to high nonlinear nature of HHG, this criterion is difficult to achieve. We have selected SIGC for HHG and carefully optimized parameters like gas pressure, cell position relative to laser focus and more importantly the design of exit endcap plate. We have used two plate configurations a) the aluminium endcap (0.5 mm thick), called SIGC(M) and b) thermally insulated endcap SIGC(I) for the study.

Fig. L.4.1 shows the experimental setup used for HHG using a 450 mm long SIGC. In SIGC, the cell is vacuum shielded with a glass window at laser entry and with a thin aluminium (0.5 to 1 mm) sheet at the exit. For HHG, the laser pulse is focused in the cell using 600mm focal length plano-convex.

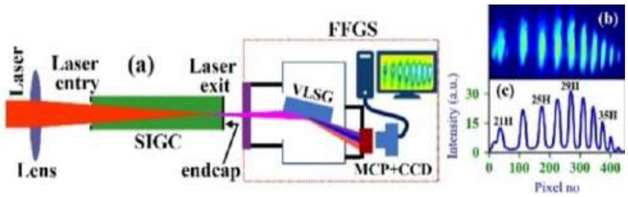

Fig. L.4.1: Experimental setup for generation and detection of high order harmonic radiation from SIGC

The laser pulse drills orifice in the endcap plate (marked in Fig. L.4.1), through which the high-harmonics and laser pulse comes out. The high-harmonics are dispersed and detected using in-house developed flat field grating spectrograph (FFGS). From the recorded FFGS spectra of high-harmonics, the vertical binning was performed to get the intensity profile. For estimation of root-mean-square (rms) intensity stability, we recorded ten consecutive spectral images of same exposure time. A separate background frame was recorded under the same condition (except without laser pulse) and was subtracted from these spectra before further processing. The integrated high-harmonic intensity (I_i) was calculated by summing the intensity of all the harmonic orders present in the spectrum recorded using FFGS. The coefficient of variation (CV) is calculated from the ratio of standard deviation (σ) and mean value (μ) of integrated high-harmonic intensity and given by

$$CV\ (\%) = \sqrt{\frac{1}{N}\sum\left(\frac{I_i}{\bar{I}} - 1\right)^2} \times 100 \qquad (1)$$

In Eq. 1, $\bar{I}$ is the mean value of intensities I_i, and N is the number of data points. A smaller CV value indicates better rms stability. We have first used SIGC (M) and optimized parameter to achieve minimum CV. Figure L.4.2 a) shows the CV and intensity of high-harmonics at optimum pressure (20 mbar). The CV is smaller on laser defocusing regime (cell position > 0) and is very localized, whereas the intensity peak is close to zero. This shows that the CV minima and intensity maxima are not coinciding. We have performed numerical simulations to understand the observation and found that during self-drilling of laser pulse in SIGC exit endcap, full beam is not able to transmit and the blocked laser part heats the endcap plate, which increases its temperature. This affects the gas flow through the exit end cap and creates density fluctuation, which is detrimental in deteriorating the source stability. To overcome this, we have used thermally insulated endcap plate.

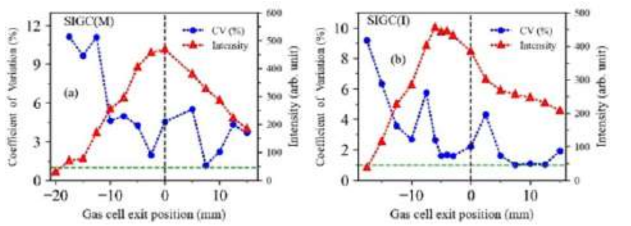

Fig. L.4.2: a) Variation of CV (left) and intensity (right) of high-harmonics in SIGC (M) with cell position, and b) variation of CV and intensity with cell position in SIGC(I), at optimum gas pressure of 20 mbar

Fig L.4.2 b) shows the CV and high-harmonic intensity at 20 mbar in SIGC(I). It can be seen that the CV improves to ~ 1% and it is not localised as in SIGC(M). The high-harmonic intensity also slightly increases as compared to Fig L.4.2 a). This shows an improvement in source stability as well as high harmonic intensity in SIGC(I). In this condition, the photon flux of > 5×10^{10} photons/laser shot in ~20 – 40 nm range (23rd to 39th harmonic order) was measured. The intensity stability was continuously monitored over duration exceeding 12 hours and average CV ⩽ 1% was maintained. The high stable HH source will be extremely useful for applications such as study of thermal transport, ultrafast demagnetization etc., where the source stability is very important to observe small changes.

Reported by:
M. Kumar (mukund@rrcat.gov.in)

L.5: Development of 200 mm diameter AR coated optics with high LIDT for high energy laser

Nd:glass (phosphate) optimally fulfils the requirements for being considered as material for developing high energy high peak power lasers mainly for the generation of intense x-rays, study of materials at extreme temperatures, pressures etc. RRCAT, Indore has embarked on the challenging programme of building such a laser indigenously.

Nd:glass disc amplifier and vacuum spatial filters of the high energy laser chain require large (dia, 200 mm) anti-reflection (AR) coated windows with high transmission and high laser induced damage threshold in nano-second regime. As such large windows with high transmission and high LIDT are not readily available from the OEMs, it is imperative to develop these windows indigenously.

Indigenous development of these crucial optical components has been carried out at High Energy Laser and Optics Division, RRCAT. This includes substrate fabrication, super-smooth optical polishing, coating design, deposition of AR coating and characterization.

To achieve this, substrates should have an ultra-low roughness, surface with minimum cosmetic defects e.g., scratches, digs and pits. Ultra-low roughness substrates significantly reduce scattering and absorption of radiation, thereby enhancing transmission and the LIDT of the optical components.

Super smooth optical polishing of fused silica (FS) substrates was carried out using bowl-feed Chemical Mechanical Polishing technique. The process is extremely slow. Surface figure ≤ λ/10 @ 589 nm, roughness better than 0.3 nm and scratch/dig ~ 20/10 were achieved as the process was optimized for 200 mm optics as shown in Fig. L.5.1.

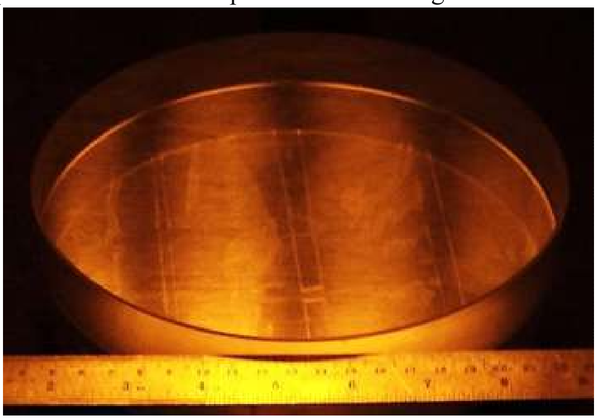

Fig. L.5.1: 200 mm super-polished FS substrate after super smooth polishing, flatness better than λ/10, scratch-dig ~ 20/10 and r.m.s. roughness 2.2Å.

Subsequently optical thin-film coating was deposited on both the substrates. A 3-layer anti-reflection coating was designed and optimized in such a way that electric field at the first SiO_2/HfO_2 interface is reduced while maintaining high transmission. Deposition of alternate SiO_2 and HfO_2 layers was carried out by dual ion beam sputtering technique. Before making the final coating on 200 mm optics trial coating runs were made for validation of the design optimization. 3 layers have been deposited in a single run of 3 hours. Same process was repeated for coating of the reverse side. Process parameters were meticulously monitored and controlled. Coated optics (Fig.L.5.2) were characterized by transmission and laser damage threshold measurements.

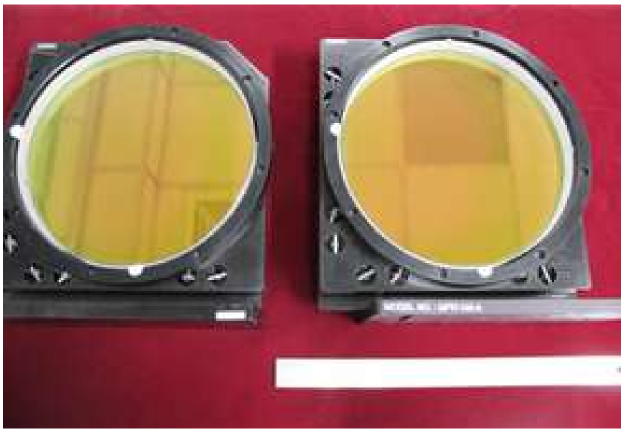

Fig. L.5.2: High transmission, high LIDT AR coated optics with T= 99.4%, LIDT = 15.8 J/cm² @ 5 nsec.

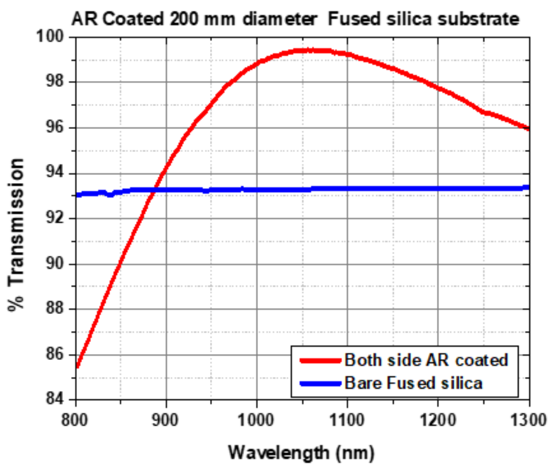

Fig. L.5.3: Transmission spectra of 200 mm dia. AR coated optics and bare substrate.

99.5 % transmission @ 1053nm and an uniformity of 0.1% are measured. Transmission 99.2 % over a wavelength band of 80 nm is obtained (Fig. L.5.3). Laser induced damage test was performed on AR coated samples with the standard 10-ON-1 method as per ISO Standard procedure (ISO-11254-1). Laser damage threshold of 15.8 J/cm² @ 5 ns (10-ON-1) and 20.6 J/cm² @ 5 ns (1-ON-1) are measured with in-house developed LIDT test set up.

Reported by:
C. Mukherjee (cmukh@rrcat.gov.in)

L.6: Demonstration of 20 MeV proton beam with laser driven ion acceleration at PW Laser Facility, RRCAT

There has been growing interest in laser-driven ion acceleration using ultra-short, ultra-intense laser pulses due to its potential applications in high-energy-density physics, medical science, and materials research. When ultra-intense laser pulses interact with thin solid targets, extreme plasma conditions are generated at target surface leading to efficient ion / electron acceleration. Proton acceleration experiments were carried out using the petawatt (PW) Ti:Sapphire laser facility at the Laser Plasma Division, RRCAT. When an ultra-short, high-intensity laser pulse is focused onto a thin metal foil, it creates a hot plasma on the target surface and generates a population of energetic electrons. These electrons propagate to the rear surface of the target, forming a strong sheath electric field, typically of the order of a few TV/m. This field ionizes and accelerates surface contaminants, primarily hydrogen and carbon, resulting in a beam of energetic protons and ions. This mechanism is known as Target Normal Sheath Acceleration (TNSA). The resulting ion beam exhibits unique features such as ultra-short pulse duration (~ps), short source size, laminar flow, and high peak current.

The experimental arrangement is shown in Fig. L.6.1. Laser pulses of ~ 9 J energy (~370 TW) were focused using an f/3 off-axis parabolic (OAP) mirror (focal length 60 cm) to a spot size of ~5 µm × 6 µm (FWHM), achieving an on-target intensity of ~2 × 10^{20} W/cm². Thin foil targets of aluminium (0.8 µm and 3 µm) and copper (1 µm and 2 µm) were used.

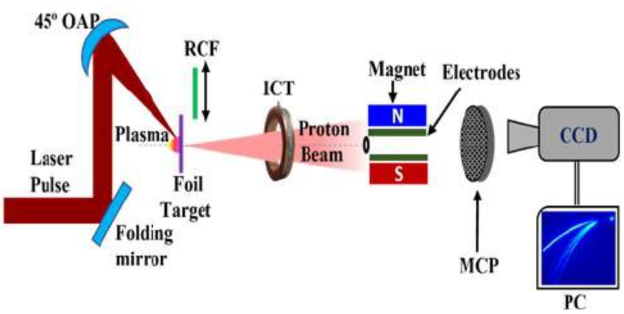

Fig. L.6.1: Schematic of experimental setup for laser-driven proton acceleration with diagnostics.

The accelerated ion beam was characterized using an in-house developed high energy Thomson Parabola Ion Spectrometer (TPIS) placed along the target normal direction. In the TPIS, crossed electric and magnetic fields separate ion species based on their charge-to-mass ratio, producing distinct parabolic traces. These were recorded using a microchannel plate (MCP) coupled with a phosphor screen and imaged using a 14-bit CCD camera. The spatial profile of the proton beam was recorded using a stack of radiochromic films (RCF) placed ~3.5 cm behind the target and covered with an 11 µm thick Aluminium foil to filter out low-energy ions. An Integrated Current Transformer (ICT) was used to measure the total proton beam charge.

The ion emission was observed to originate from a small region (tens of micrometres) on the rear surface and within a cone angle of ~10°–15°. The accelerated ion species mainly consisted of protons and carbon ions. Fig. L.6.2(a) shows the TPIS image with distinct ion traces, while the corresponding proton energy spectrum, derived using a MATLAB-based reconstruction algorithm, is shown in Fig. L.6.2(b). The maximum proton energy achieved was ~23 MeV at ~0.37 PW laser power. Fig. L.6.2(c) shows the proton beam profiles recorded on different RCF layers, clearly indicating the presence of protons with energies exceeding 20 MeV. The total proton beam charge was estimated using the ICT. The integrated beam charge of ~100 nC is measured from the ICT signal.

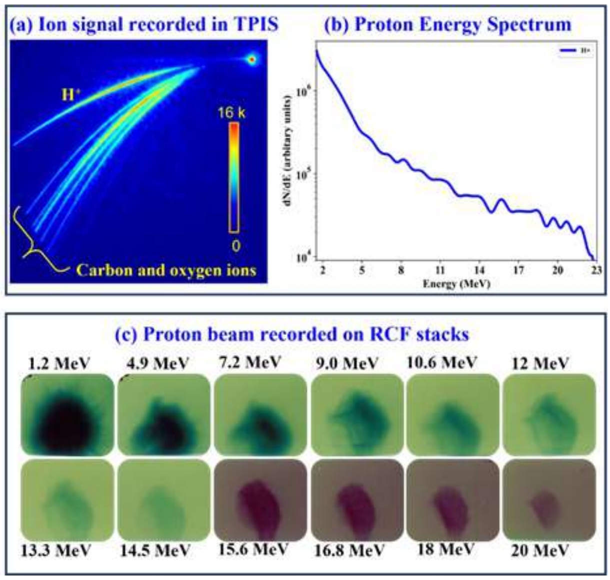

Fig. L.6.2: (a) TPIS image showing ion species separation, (b) derived proton energy spectrum, (c) proton beam profiles recorded on RCF stack with energy cut-offs.

This work demonstrates successful acceleration of protons to energies exceeding 20 MeV using the PW laser facility at RRCAT for the first time in the country. The combination of diagnostics such as TPIS, RCF, and ICT enables comprehensive characterization of the proton beam in terms of energy, spatial profile, and charge. These results establish a strong foundation for further studies on beam transport, control, and application-oriented developments / applications.

Reported by:
M. Tayyab (tayyab@rrcat.gov.in)

L.7: Enhancement of laser generated shock-pressure using low density coatings on Al-foil targets

The laser-driven dynamic compression of matter under extreme pressure conditions (on the order of tens of megabars to gigabars) is a subject of significant interest in various fields of physics, including phase transformations, materials science, astrophysics, geophysics, and high energy density physics applications. Such extreme conditions can be generated in laboratory environments using high-energy, high-power (HEHP) laser systems.

The low-density target was fabricated by depositing carbon aerogel (CA) onto an aluminium (Al) foil substrate using an air spray gun with a 0.3 mm nozzle aperture. The morphology of the resulting CA was characterized using field-emission scanning electron microscopy (FESEM) (Fig. L.7.1). The thickness of the coated film was measured using a profilometer and was approximately 20 µm. The density of the fabricated carbon on the Al-foil (density~2700 mg cm^{-3}) is approximately 300 mg cm^{-3}.

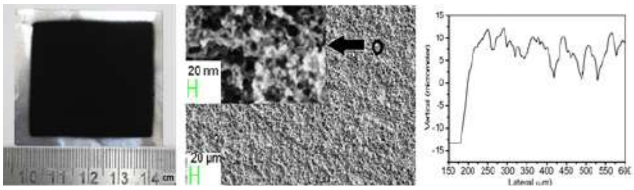

Fig. L.7.1 Morphology of the coated CA.

A schematic of the experimental setup is shown in Fig. L.7.2. The experiments were conducted using a high-energy, high-power Nd:glass laser system in the laboratory, delivering laser energies in the range of ~5–20 J. The laser (with pulse ~0.5 ns duration) was focused onto the target using a plano-convex lens (f = 55 cm), resulting in intensities on the order of 10^{13}-10^{14} W cm^{-2}. The targets were mounted on a motorized translation stage inside a plasma chamber maintained at a vacuum of ~5×10^{-5} mbar.

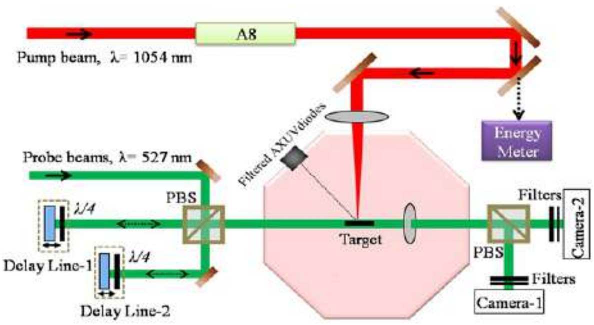

Fig. L.7.2 The experimental setup.

The probe beam was derived by tapping a portion of the main beam and converting it to its second harmonic using a KDP crystal. Two temporally separated second-harmonic probe beams were then generated via polarization discrimination, producing orthogonally polarized components (Fig. L.7.2). The relative optical delays between the main beam and the two probe pulses were independently controlled using delay lines 1 and 2. A plano-convex lens (f = 5 cm) was used to image the plasma plane. The orthogonally polarized probe beams were separated using a polarizing beam splitter and directed onto DSLR cameras positioned at the image plane.

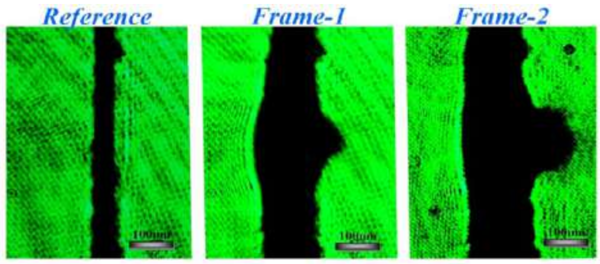

Fig. L.7.3 Typical shadowgrams of a reference, frame-1(2ns) and frame-2(3.5ns).

The particle velocities in both the targets were measured using two-frame shadowgraphy. Experiments were conducted over a range of laser intensities (~7.5×10^{13} to 2.3×10^{14} W cm^{-2}). Fig. L.7.3 shows typical shadowgrams obtained for the CA-coated Al-foil targets. Similar shadowgrams were also recorded for Al-foil targets.

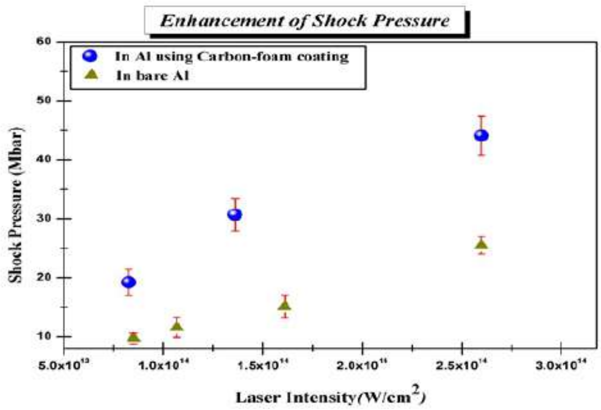

Fig. L.7.4 Variation of shock pressure with laser intensity in Al and CA coated Al.

The shock pressure (P) in the foil target of initial mass density (ρ_0) was estimated from measurements of particle velocity (U_p) using the Hugoniot relation, $P=\rho_0(a+bU_p)U_p$, where a and b are material-specific constants. Fig. L.7.4 illustrates the variation in shock pressure as a function of laser intensity. As a laser-driven shock propagates from a low-density medium to a higher-density material, shock amplification occurs due to the impedance mismatch between the two media. The results indicate that the CA coating on the Al-foil enhances the laser-driven shock pressure by approximately a factor of two compared with the uncoated Al-foil.

Reported by:
Atul Kumar (katul@rrcat.gov.in)

M.1: Operation of the IR-FEL facility in the 'User Mode'

The Infra-red Free Electron Laser (IR-FEL) based user facility, which is the first of its kind in the country, was formally inaugurated in December 2024 for outside users by Dr. A. K. Mohanty, Secretary, DAE and Chairman, AEC. The light from the IR-FEL is regularly delivered at the user facility for experiments. Two experimental stations are presently available for the users: (i) Frequency domain spectroscopy in low temperature and high magnetic field environment, and (ii) wavelength selective scanning, imaging and absorption studies at room temperature using pyro-electric detectors and a home-built Michelson interferometer. A third user port has been commissioned for FEL Physics experiments, which is also available for users to set up experimental stations for studies in Chemistry, Biology or other areas. More user stations will be available in the near future.

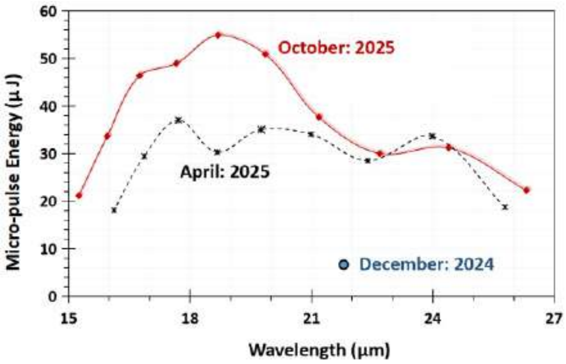

Fig. M.1.1: Improvement in peak micro-pulse energy at a user station through machine optimization.

The IR-FEL provides continuously tunable radiation from 12.5 - 50 micron wavelength with a CW average photon flux ~10^{14} photons/s and a peak photon flux of ~10^{18} photons/s over 10 ps micropulses at the user stations. The facility has been operated in the 'User Mode' for more than 750 hours in the year 2025. Repeatable and stable (5%) operation of the machine over typical user cycles of 8 hours, with machine start-up time ~15 minutes after initial conditioning, have been established. At the request of users from TIFR and IIT Bombay for their proposed studies of nonlinear phenomena using IR-FEL light, the energy per micropulse at the user stations has been enhanced from ~7 μJ/micropulse in December 2024 to more than 30 μJ/pulse at present over the wavelength range from 16- 26 microns, with a peak of >50 μJ/micropulse at 19.12 microns (Fig. M.1.1).

Using the IR-FEL light, user experiments have been performed to study the wavelength dependencies of photo-currents in bulk narrow gap semiconductor and absorption in a silver black sample received from CEERI Pilani. Wavelength dependent absorption spectroscopy and imaging studies in both transmission and reflection modes (see Fig. M.1.2) were performed on two Ti-V alloy thin film based superconducting radiation detector structure samples (consisting of a meander structure and inter-digitated capacitor) designed and developed in-house. The experimentally obtained absorption characteristics matched reasonably well with the results of electromagnetic (CST) simulation. The first results of this study were presented at the Low Temperature Detectors Conference LTD-2025, New Mexico, and the sharp tunability of IR-FEL is crucial for these studies.

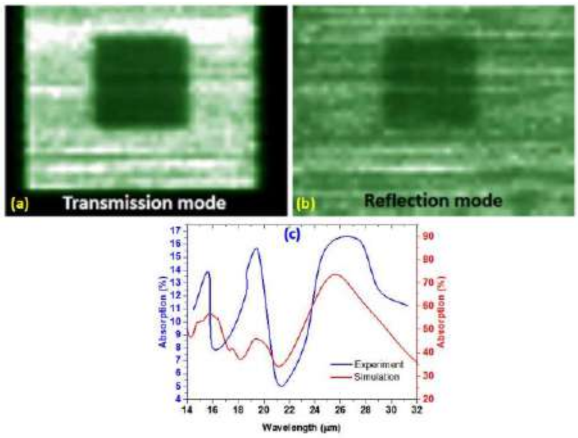

Fig. M.1.2: Scanning measurements using IR-FEL light on superconducting Ti-V thin film radiation detector structure, and comparison with CST simulation.

Utilizing the fact that pure AlN has an absorption band between 11 and 18 micron wavelengths, the IR-FEL light was used to locate the sites of inhomogeneities in an AlN thin film (see Fig. M.1.3) through scanning-imaging experiments. The IR-FEL light was sequentially tuned at wavelengths within and outside the absorption band of pure AlN, and the disorder sites were located by scaling the measured reflectivities.

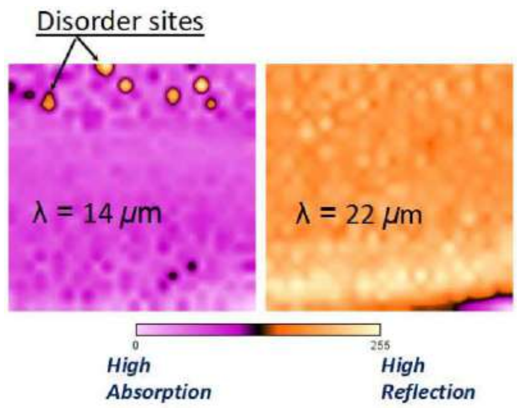

Fig. M.1.3: Wavelength selective scanning-imaging of AlN thin film using IR-FEL light revealing sample inhomogeneities.

For the non-destructive characterization technique presented above (Fig. M.1.3) the tunability and power of the IR-FEL are essential, and a spatial resolution of 300 microns is achieved.

Reported by:
M. K. Chattopadhyay (maulindu@rrcat.gov.in)

M.2: Development of thin wall dome structure for aerospace application using LAM-DED process

In aerospace, dome structures with diameter more than 300 mm are used as pressure vessels for spacecraft fuel tanks, and rocket engine components that demand high strength and thermal resistance. Dome structures are commonly developed using sheet forming, spinning, deep drawing, or segment-wise forming followed by welding. These traditional approaches require dedicated tooling, multiple forming stages, and extensive post-processing in addition to long manufacturing cycles. In thin sections, they are often associated with challenges such as dimensional inaccuracy, spring-back, residual stresses, weld-induced distortion, and material wastage. In contrast, the laser directed energy deposition based additive manufacturing (LAM-DED) process enables near-net-shape fabrication directly from a digital model, eliminating the need for complex dies and reducing the number of processing steps. Further, the layer-by-layer deposition approach provides precise control over heat input, bead geometry, and wall thickness, which is particularly critical for thin-wall dome structures. Furthermore, additive manufacturing minimizes material loss, enables rapid design modification, and facilitates in-situ repair of high-value aerospace components capabilities that are limited in conventional methods.

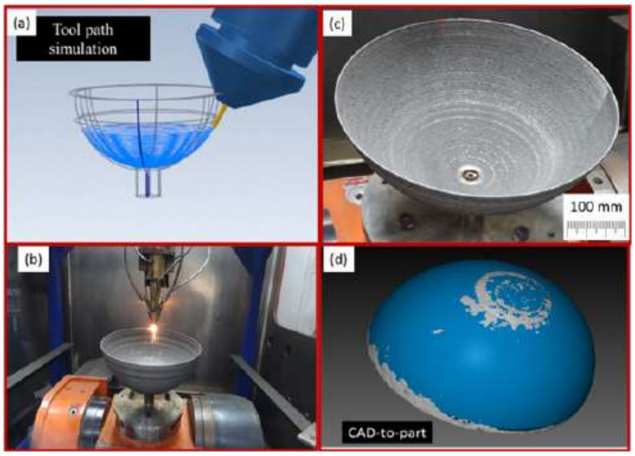

Fig. M.2.1: (a) Photograph of tool path simulation, (b-c) photograph of actual dome structure during and after deposition process, (d) CAD to part comparison

In the present study development of dome structure of SS 304 L steel with diameter ~400 mm is undertaken using LAM-DED process. A novel methodology has been developed in this study for developing a thin-walled hemispherical dome of SS 304L steel with diameter approximately ~400 mm using LAM-DED without the need for support structures. A custom-designed 5-axis kinematic system is employed to overcome challenges associated with large overhang angles, thereby enhancing slicing precision and deposition accuracy. The process incorporates meridional slicing to ensure melt-pool stability and circumferential rotation for uniform layer deposition. A unique slicing algorithm is introduced, which incrementally adjusts slice height along the meridian axis, enabling dome fabrication on a cylindrical substrate. Process parameters such as laser power, powder feed rate, and scan speed are optimized, and novel toolpath simulations (Fig. M.2.1a) confirm collision-free deposition. Using the optimized parameters laser power of 750-850 W, a constant linear scan speed of 600 mm/min, and a powder feed rate of 8.6 g/min, a hemispherical dome structure with a diameter of ~425 mm and wall thickness of 2.5 mm is successfully developed. Photographs captured during and after deposition are shown in Fig. M.2.1 (b & c). Geometrical characterization of the as-built dome includes surface roughness analysis, CAD-to-part comparisons. The CAD-to-part comparison (Fig. M.2.1d), based on 3D scanning, indicates an average wall thickness of 2.49 ± 0.08 mm, with outer and inner diameters measured at 425.08 ± 0.15 mm and 422.43 ± 0.29 mm, respectively. The dimensional deviation from the nominal diameter is only 0.41%, well within acceptable tolerance limits, indicating high dimensional accuracy and geometrical stability. Surface roughness measurements over a 2 mm scan length show average R_a values of 2.35 ± 0.17 µm for the outer surface and 9.51 ± 0.63 µm for the inner surface, as depicted in Fig. M.2.2(a & b). Optical microscopy (Fig. M.2.2(c)) reveals a defect-free microstructure comprising of cellular, columnar, and equiaxed dendritic grains. Additionally, Pulse-Echo ultrasonic testing under submerged conditions confirms the absence of porosity and cracks in the as-built dome structure. This approach offers a scalable and support-less manufacturing solution for complex hemispherical geometries, with potential applications in the aerospace and energy sectors.

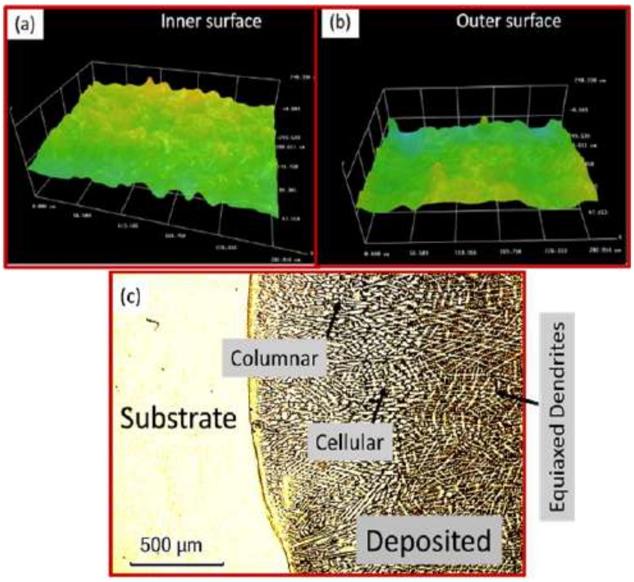

Fig. M.2.2: (a-b) 3D surface profile of outer and inner surfaces, (c) Optical micrograph of the as built dome structure.

Reported by:
C. P. Paul (paulcp@rrcat.gov.in)

M.3: Development of Chromox ceramic for Hydrogen ion beam detection

Chromium-doped Al_2O_3 (Chromox) scintillator ceramic screens are extensively used for electron and proton beam diagnostics in accelerator programs. At present, such screens are largely imported. The present activity at Photonic Materials Technology Section, carried out in collaboration with Proton Linac Development Division, RRCAT, aims to develop indigenous Chromox scintillator screens with a diameter of 70–75 mm and a thickness of 3-4 mm for hydrogen ion beam detection.

Chromox powder with 0.5 at.% Cr^{3+} doping was synthesized via a conventional solid-state reaction route using high-purity aluminium oxide and chromium oxide. The powders were calcined at 1200 °C, compacted into pellets of 90 mm diameter, and sintered at 1650 °C under high vacuum (~5 × 10^{-6} mbar). Dense ceramic disks with a diameter of ~72 mm and thickness of ~3.0 mm were obtained (Fig. M.3.1a). The sintered samples exhibited well-defined grains with an average grain size of ~5 µm (Fig. M.3.1b). The sintered pellets were lapped and optically polished prior to detailed structural and optical characterization.

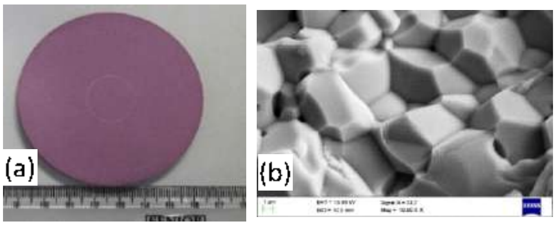

Fig. M.3.1: (a) As sintered Chromox ceramic screen (b) SEM of fractured surface

X-ray diffraction analysis confirmed the formation of a single-phase hexagonal close-packed α-Al_2O_3 structure with no detectable impurity phases (Fig. M.3.2). Photoluminescence measurements exhibited two prominent emission peaks at 694.3 nm and 692.7 nm, corresponding to the characteristic ^2E to $^4A_2$ transition of Cr^{3+} ions (Fig. M.3.3a). The measured luminescence lifetime for this transition was approximately 3 × 10^{-3} sec (Fig. M.3.3b). The

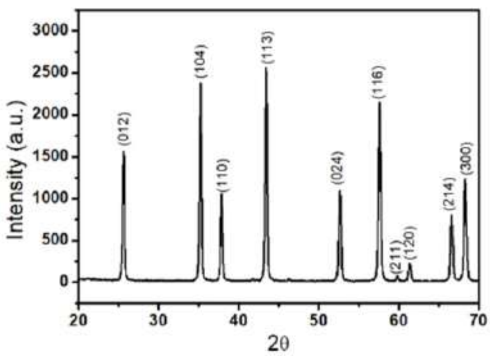

Fig. M.3.2: Powder X-ray diffraction of sintered ceramic

observed emission wavelengths and lifetime closely match reported literature values, thereby validating the optical quality of the synthesized Chromox ceramics.

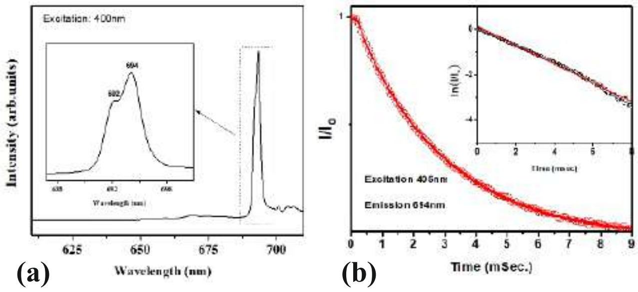

Fig. M.3.3: (a) Photo-luminescence spectra and (b) Plot of intensity versus time for Chromox.

For beam diagnostics, the Chromox scintillator screen was mounted inside a diagnostics chamber under vacuum at a distance of 300 mm from the last ground electrode. A hydrogen ion beam generated using an ECR plasma source was accelerated to an energy of 25 keV and directed onto the Chromox screen mounted at an angle of 45° using a CF100 flange. The scintillation image was transmitted through a quartz window and recorded by a high-sensitivity camera positioned at 90° to the beam axis outside the chamber.

Beam images recorded using the Chromox scintillator screen at microwave powers of (a) 200 W, (b) 500 W, and (c) 800 W, at a fixed hydrogen gas pressure of 1.6 × 10^{-5} mbar and beam energy of 25 keV, are shown in Fig. M.3.4. Visible scintillation emission was first observed at a microwave power of ~200 W.

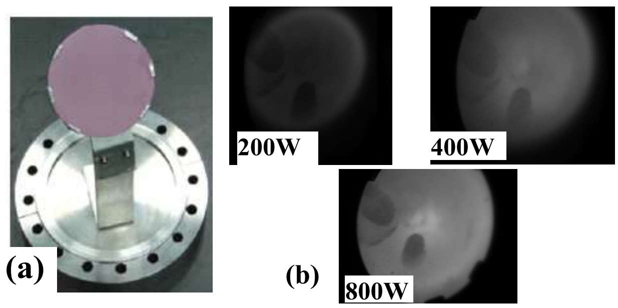

Fig. M.3.4: (a)Mounting arrangement of the Chromox scintillator screen on the CF100 flange. (b) The images captured using Chromox scintillator screen at varying microwave power

With increasing microwave power, the beam spot exhibited enhanced brightness and improved sharpness, consistent with an increase in beam current and ionization efficiency. The Chromox scintillator screen produced stable and reproducible signals over the entire range of tested operating conditions and duty factors, demonstrating its suitability for hydrogen ion beam diagnostics in accelerator applications.

Reported by:
Gurvinderjit Singh (gjit@rrcat.gov.in)

M.4: Development of flexible triboelectric nanogenerator for vibration energy harvesting

The rapid expansion of sensors, wearable electronics, and Internet-of-Things (IoT) technologies has intensified the demand for sustainable and maintenance-free power sources. In many real-world applications such as remote sensing and wearable systems, frequent battery replacement is impractical. Harvesting ambient mechanical energy available abundantly in the form of vibrations, human motion, airflow, and surface contact offers a promising alternative. Triboelectric nanogenerators (TENGs) have emerged as efficient devices capable of converting low-frequency mechanical energy into electrical energy, enabling self-powered electronic systems.

TENGs operation is based on the combined effects of triboelectrification and electrostatic induction. When two dissimilar materials come into contact, charge transfer occurs depending on their relative triboelectric polarity. Upon separation, an electric potential difference is generated, driving electrons through an external circuit. Repeated contact-separation cycles produce alternating electrical output. In the present work, a contact–separation mode flexible TENG was developed for vibration energy harvesting applications and tested under a periodic mechanical force of 30 N at a frequency of 4 Hz, representative of low-frequency ambient vibrations.

Zinc oxide (ZnO) thin film was employed as the tribopositive layer and polydimethylsiloxane (PDMS) as the tribonegative layer. ZnO is a multifunctional semiconductor with good flexibility, chemical stability, and tunable electronic properties, while PDMS offers high electronegativity, flexibility, and biocompatibility. Both layers were deposited on ITO-coated PET substrates, resulting in a fully flexible device architecture suitable for wearable and vibration-based applications. To overcome the limited output of conventional ZnO-PDMS TENGs, three systematic material-engineering strategies were adopted. First, ZnO was doped with 2 at.% aluminium (Al) to increase free electron concentration and reduce its work function. This enhanced the tribopositivity of ZnO, leading to improved charge transfer during contact electrification. Second, a thin SiO_2 interlayer was introduced between Al-doped ZnO and the ITO electrode to suppress electron diffusion from ZnO into ITO. Kelvin probe force microscopy measurements confirmed that an optimized SiO_2 thickness of ~100 nm effectively blocked electron loss and further reduced the effective work function of ZnO, resulting in enhanced output performance. Third, MoS_2 nanoflowers were incorporated into the PDMS matrix to improve its charge storage capability. An optimized MoS_2 concentration of 6 wt.% formed a nanocapacitor network within PDMS, increasing its dielectric constant without inducing electrical leakage. The schematic of flexible TENG and the corresponding band diagram showing triboelectrification are shown in Fig. M.4.1 a and b respectively.

By combining Al-doped ZnO, an optimized SiO_2 interlayer, and MoS_2 enhanced PDMS, the flexible TENG exhibited a significant improvement in electrical output. The optimized device generated an open-circuit voltage of ~369 V and a short-circuit current of ~28 μA (Fig. M.4.1 c), compared to ~112 V and ~7.8 μA for the pristine ZnO-PDMS TENG. The maximum instantaneous power density reached ~1.8 mW/cm^2 at an optimized load resistance (Fig. M.4.1 d). The device demonstrated excellent mechanical robustness and operational stability, maintaining stable output over 10,000 contact-separation cycles and showing negligible degradation over six months. The harvested energy was successfully used to charge commercial capacitors (1–10 μF) and directly power array of 400 LEDs (Fig. M.4.1 e), showing its capability for low-power electronic applications.

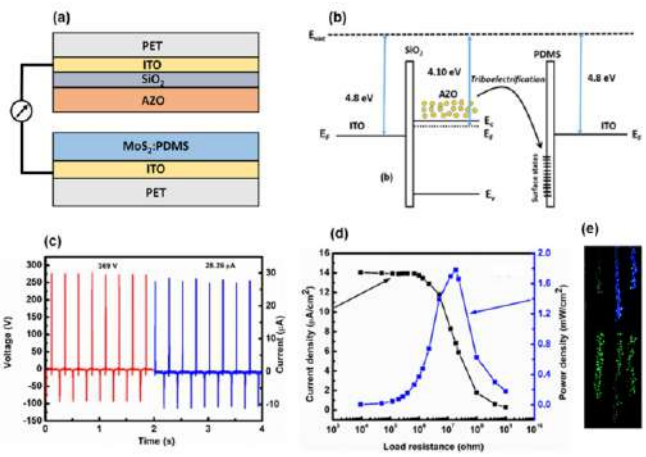

Fig. M.4.1: (a) Schematic of ZnO TENG, (b) band diagram showing triboelectrification, (c) open-circuit voltage & short circuit current, (d) current and power density with the load resistance and (e) flashing of 400 LEDs using the rectified output of TENG

This work highlights a systematic approach to enhance flexible TENG performance through electronic and interfacial engineering. The developed ZnO-based flexible TENG shows strong potential for self-powered sensors, wearable electronics, smart flooring, and low-power IoT systems, contributing toward sustainable and battery-free energy solutions.

Reported by:
Pankaj Misra (pmisra@rrcat.gov.in)

M.5: Development of a multimodal microscopic imaging system capable of hyperspectral and multi-wavelength time-lapse imaging for biomedical applications

Optical microscopy techniques play a crucial role and have been widely employed in biomedical research. Fundamentally, these techniques exploit various aspects such as morphological feature, transmittance, fluorescence, scattering, and phase, enabling a deeper insight of the intricate structures and functions in the biological systems at the cellular and subcellular level. Although conventional microscopy enables real-time visualization of cells, tissue, and extracellular matrices, it often relies on chemical-staining or fluorophore tagging. Moreover, the information is typically limited to colour contrast, which lacks sufficient spectral specificity to distinguish biomolecules with closely overlapping spectral signatures. Such difficulties can be addressed by integrating spectral information into the microscopic images, yielding rich spatio-spectral content and thereby elucidating more precise biochemical characterization of biological specimens. In addition, integrating time-lapse imaging facilitates temporal-spectral image acquisition, enabling visualization and analysis of dynamic biological processes. Since temporal morphological changes are the aftermath of the intrinsic biochemical alternations, hence, temporal-spectral imaging is crucial for comprehensive monitoring of dynamic biological phenomena.

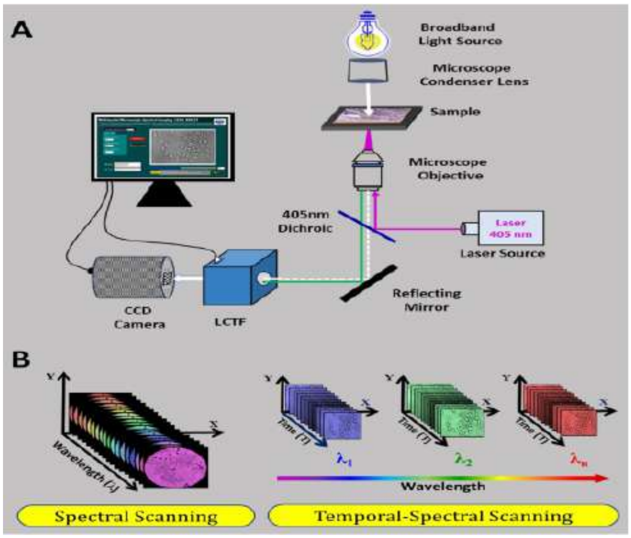

Fig. M.5.1: (A) Schematic diagram and (B) schematics of Hyperspectral data cube generation through Multimodal Microscopic Spectral Imaging system.

Recently, we have developed an imaging system (fig. M.5.1) employing liquid crystal tunable filter (LCTF) as spectral decomposition element that offers flexible waveband selection without compromising spatial resolution. A Graphical User Interface (GUI) software was developed for hardware control of the system to offer user-friendly spectral data acquisition and analysis platform. The main GUI of the system comprises six dedicated modules: configuration settings module, single wavelength spectral image acquisition module, multi and hyper-spectral image acquisition module, multi-wavelength time-lapse image acquisition module, spectral image analysis module, temporal image analysis module (fig. M.5.2). Developed system was calibrated and systematically characterized for all domains: spatial, spectral, and temporal. Further, multi-wavelength time-lapse fluorescence images of resected breast tissue were acquired and analyzed.

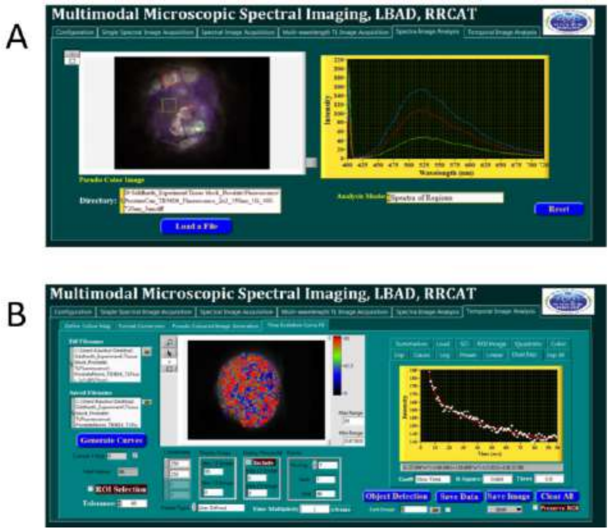

Fig. M.5.2: GUI for spectral image analysis: (A) Hyperspectral and multispectral image analysis, (B) time-lapse spectral image analysis

Multimodality of the developed imaging system was demonstrated through Transmission Hyper-Spectral Imaging (THSI) and Fluorescence Hyperspectral Imaging (FHSI) as well as spectral and temporal-spectral scanning mode. Systematic calibration and characterization of the system in the spatial and spectral domains ensured its accuracy, reliability, and reproducibility. The linearity of its response to exposure time and emission intensity further confirmed its suitability for quantitative imaging. Validation experiments conducted on real biological samples and model systems highlights its potential for a wide range of biomedical applications. The performance of the system was evaluated for delineation of cancer margin in resected tissue samples. The fluorescence photobleaching characteristic measured via time-lapse fluorescence imaging at multiple wavelength bands was found to be a potential biomarker in breast tissue characterization. Further, the supremacy of state-of-the-art machine learning algorithms over the conventional parametric model-based approach were established in semantic image segmentation of interrogated samples.

Reported by:
Hemant Krishna (hkrishna@rrcat.gov.in)

M.6: Detection of urea adulteration in packaged milk samples using spatially offset Raman spectroscopy

Milk is a nutritional food item that is frequently adulterated with urea. Water is routinely added to maximise milk volume for commercial gain. In order to account for density reduction in diluted milk, urea is added to compensate the lactometer reading. Further, urea is added to mimic the nitrogenous content of protein in diluted milk, which is generally estimated using the Kjeldahl method. However, consumption of urea-adulterated milk samples can pose several health hazards.

Over the years, many techniques have been used to detect urea in milk (conductometric, potentiometric, electrochemical, MS, GC, and chemical assays), but they often require tedious sample preparation, multiple extraction steps, have utility to the limited concentration ranges, and are unstable. Optical methods such as diffuse reflectance, ATR-FTIR and Raman spectroscopy have emerged as attractive alternatives, with Raman offering molecular specificity and robust quantitative performance. However, there is an urgent need for a non-invasive method for detecting adulteration in packaged milk, especially in India and other South Asian countries, where even packaged milk is often found to be adulterated with urea. This motivates to explore the depth-sensitive Raman technique like spatially offset Raman spectroscopy (SORS) for detection of urea adulteration in packaged milk. The technique is well suited for measuring depth sensitive Raman signal beyond the probing depth of confocal technique.

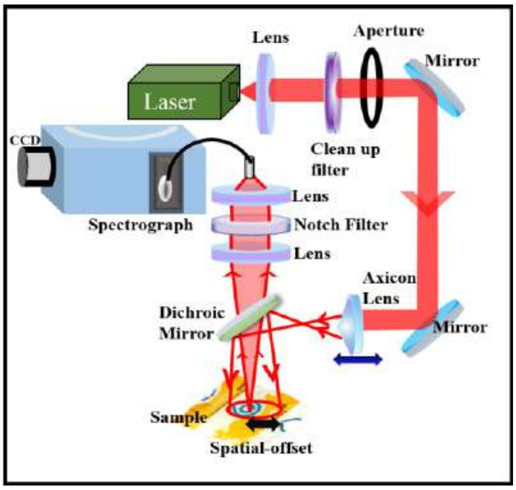

Fig. M.6.1: Optical setup of the inverse SORS system.

We report here, the development of a setup which employed inverse configuration of SORS measurement. The setup uses a 785 nm multimode diode laser for excitation, an axicon lens for ring illumination, and backscattered Raman photons are collected from the centre of the ring, thereby providing a spatial offset between illumination and collection. This configuration helps in preferentially recovering sub-surface Raman signals from milk beneath low-density polyethene (LDPE) packaging. The Raman spectra from urea-spiked cow milk samples (0.25–5.0 g/L) in 60 µm LDPE were measured at an optimised spatial offset of 6.5 mm, which maximises the relative contribution of milk compared to the surface polythene.

Various processing steps were performed on the measured spectra such as Savitzky–Golay smoothing, range-independent background subtraction and SNV normalization. These processed data are then used as input for the chemometric analysis, such as least squares regression and partial least squares regression to quantify the adulteration. It was found that PLSR with the optimized number of variables performed best in estimation of the adulterant concentrations. The root mean square error (RMSE) in predicting adulterant concentration was estimated to be 0.243 g/L for previous unseen data used to build the regression model. The limit of detection (LOD) and limit of quantification (LOQ) were found to be 0.22 g/L and 0.67 g/L, respectively. The method reliably detects all urea concentrations above the 0.70 g/L, a limit set by FSSAI for safe use of the milk. The Fig. M.6.2a shows the correlation plots between reference and predicted urea concentrations, which show $R^2 = 0.99$ and RMSE=0.243 g/L.

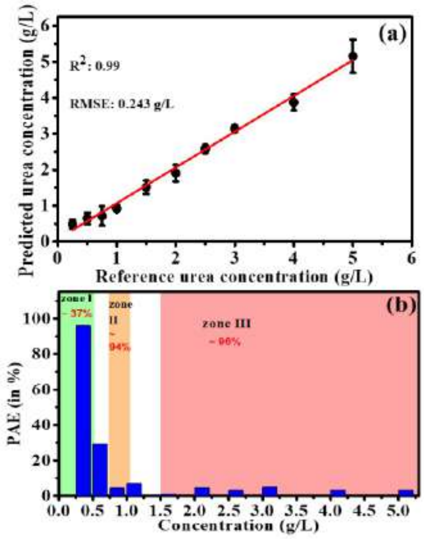

Fig. M.6.2: (a) Correlation plots between the reference and predicted concentrations. (b) Plot of the percentage absolute error at each adulteration.

The percentage absolute error (PAE) at each measured concentration is shown in Fig. M.6.2b and are organized into three zones: a safe green zone (⩽ 0.50 g/L) with low regulatory concern but higher relative error, an orange zone (0.75–1.0 g/L) and a red zone (1.5–5.0 g/L) where prediction accuracies are more than 94% and 96% respectively. To conclude, the developed inverse spatially offset Raman spectroscopic technique demonstrates the ability of quantitative detection of urea concentration in packaged milk samples without opening the packet and without the need of tedious sample preparation procedure.

Reported by:
Anita (anitadalal@rrcat.gov.in)

I.1: Developments for IT infrastructure

AI-Powered Fire and Smoke Detection for Critical IT Infrastructure: AI-powered fire and smoke detection system has been developed for critical IT infrastructure. There was a need for a system capable of accurate and rapid fire and smoke detection using AI-based techniques, with a target of 95% accuracy and a detection time of under two seconds. The system's architecture was designed for compatibility with edge devices and existing fire alarm systems. Publicly available datasets were explored and evaluated, and a scalable system architecture was drafted. Pre-trained models were benchmarked, hardware and software requirements were finalized, and findings and architecture plans were presented to stakeholders. Models were trained on these datasets, focusing on performance metrics, and validated using robust techniques. Pre-trained models were fine-tuned and optimized for real-time performance. Testing of the system was conducted under both real and simulated conditions. The system was also demonstrated to fire and safety personnel, and feedback was gathered for further improvements.

Fig. I.1.1: AI-Powered Fire and Smoke Detection System

Commissioning of new RRCAT computing cloud: IAAS (Infrastructure As A Service) based Computing Cloud to meet short term requirement of users for small and medium capacity server machines has been successfully completed. This computing cloud will enable scientists and engineers to quickly establish computing environment as per their requirement. This Computing Cloud, deployed using open-source tools, comprises of Controller, Compute, Network and Storage node. The computing environment can be established using cloud OS images available for operating systems like Red Hat Enterprise Linux, OpenSUSE, Fedora, Ubuntu, FreeBSD, Scientific Linux, Rocky Linux. Users can quickly create virtual server with required configurations for their short-term computing requirement. These virtual servers will be accessible to the users through their desktop machine over RRCATNet.

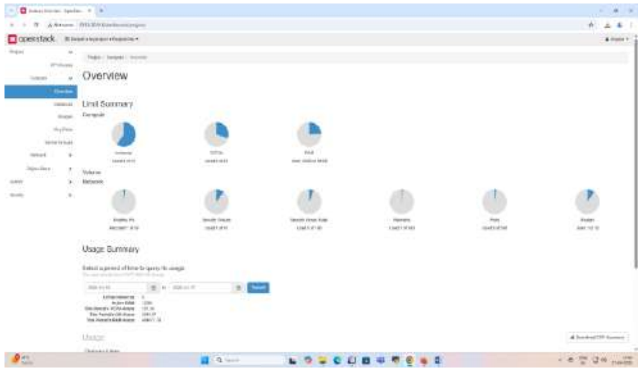

Fig. I.1.2: Dashboard of RRCAT Cloud

Design & development of secure PDF files Merge/Split facility – PDF-सहयोगी: PDF-सहयोगी is an in-house designed and developed solution for securely merging/splitting PDF files over Intranet. This ensures confidentiality of sensitive organizational data and solves the problem of unintentional exposure of organizational data on internet, by users. The system allows users to securely log in using email credentials and split/merge PDF files for meeting various documentation requirements. The web interface features an intuitive drag-and-drop interface that renders PDF thumbnails of uploaded files, enabling users to effortlessly reorder pages during both merging and splitting process. The system supports multiple concurrent users and secure communication protocols. Necessary configurations have been made in the system to protect against cross-site request forgery attacks. PDF-सहयोगी will be helpful in improving the security posture of RRCATNet, by solving the problem of exposure of organizational data by users who tend to use free tools in order to merge/split PDF documents.

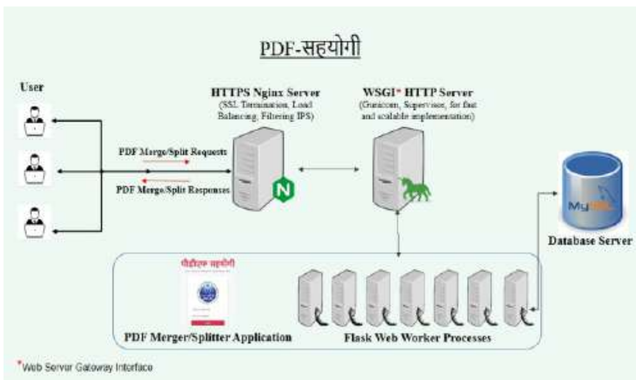

Fig. I.1.3: Diagram depicting workflow of secure PDF files Merging/Splitting facility – PDF-सहयोगी

Reported by:
Alpana Rajan (alpana@rrcat.gov.in)

I.2: Wax electroforming of Prototype Acceleration Grid (PAG) plate for IPR

Design and Manufacturing Technology Division of RRCAT initiated a project to develop ion extractor grids for Neutral Beam Injection (NBI) system for generating high-energy neutral hydrogen beams for the Institute for Plasma Research (IPR), Gandhinagar. A critical component of the NBI system is the ion extractor assembly, which consists of three OFE copper grids: (i) Acceleration Grid, (ii) Deceleration Grid, and (iii) Earth Grid. The acceleration grid experiences a heat load of approximately 1.75 MW/m^2, necessitating efficient heat removal through a dense network of wavy semi-circular cooling channels (radius $\approx$ 1.1 mm) embedded between the rows of beam apertures.

Fabrication of the ion extractor grid is technologically demanding and involves several specialized processes, including: (i) joining of dissimilar metals—SS304L rods to an OFE copper plate—for fabrication of the water manifold; (ii) electroforming of OFE copper to a thickness of about 3 mm to form embedded cooling channels; and (iii) precision CNC machining of the grid plate. Only a few manufacturers worldwide possess electroforming capabilities, and their services are available at very high cost. Indian industry is still in the process of developing the electroforming technology.

To address this challenge, DMTD developed the cold additive manufacturing capability for copper electroforming up to 3 mm thickness on CNC-milled OFE copper plates to fabricate embedded cooling channels. Machined grooves were initially filled with wax and coated with silver to provide electrical conductivity for subsequent electrodeposition. Copper deposition was carried out in an acidified bath at a current density of ~2 A/dm^2 using periodic reversal mode, followed by thermal removal of wax.

Fig. I.2.1: Machined wavy grooves on the grid plate

Fig. I.2.1 shows the Prototype Acceleration Grid (PAG) plate after machining and chemical cleaning. The machined grooves were first filled with wax, followed by silver coating on the wax to impart electrical conductivity, enabling subsequent copper electrodeposition, as illustrated in Fig. I.2.2 and I.2.3. Fig. I.2.4 shows electrodeposited PAG plate with about 3 mm thick uniform copper plating on the entire plate surface including silver coated wax.

The final PAG plate contains 214 apertures of 8 mm diameter, with a 0.4 mm clearance from the adjacent cooling channels arranged in a dense network of 2 mm wavy semi-circular channels (Fig. I.2.5). Channel continuity was verified using LCD, volumetric, and radiographic inspection methods. Helium leak testing at the Ultra High Vacuum Technology Section of RRCAT confirmed leak-tightness below 1×10^{-9} mbar·lit/s after 8 bar pressure testing and vacuum baking at 180 °C for four hours.

Fig. I.2.2: Wax filled wavy grooves on the grid plate

Fig. I.2.3: Wax filled wavy grooves coated with silver

Fig. I.2.4: Copper deposited on the silver coated wax

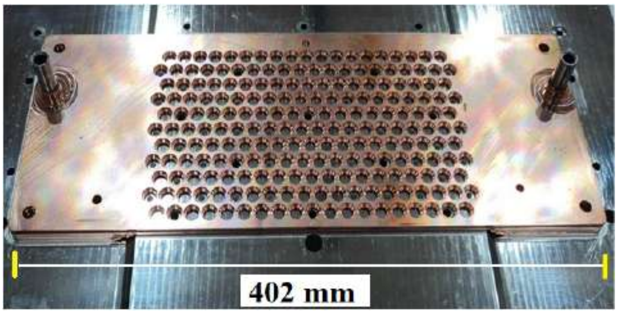

Fig. I.2.5: PAG plate with embedded cooling channels

This development demonstrates strong potential for the indigenous fabrication of critical components with fine embedded cooling features required for advanced accelerator and fusion applications.

Reported by:
Abhay Kumar (abhay@rrcat.gov.in)

I.3: Accelerator Subsystem Development Facility

The Lake Side Workshop, constructed approximately 30 years ago to support the accelerator-based program in technical area of RRCAT, required extensive modifications to meet the institution's current needs. The project aimed to adapt the existing rectangular building—with low bay areas on both sides and a high bay in the centre to accommodate three modern lab facilities. Renovation plans include incorporating a mezzanine steel structure, installing essential utilities, and reconfiguring spaces to optimize functionality. Following the renovation, the facility was renamed as the Accelerator Subsystem Development Facility.

Design Vision: To transform the aging structure into a contemporary facility, the core intent focused on maximizing usability, ensuring functional segregation, enhancing accessibility, and upgrading services to meet current standards. The planning strategy emphasized multi-user accommodation, spatial optimization, and inclusive infrastructure upgrades to create a versatile, efficient, and accessible environment.

Sustainability approach:

Design Philosophy: The Non-Destructive Testing (NDT) investigation of the Lakeside Workshop was carried out to evaluate concrete uniformity, corrosion risk, and overall structural health. The assessment used Ultrasonic Pulse Velocity (UPV) Test (80 locations), Rebound Hammer Test (80 locations), Half-Cell Potentiometer Test (22 locations), Carbonation Depth Test (11 locations), and Concrete Core Test (3 samples) along with visual inspection. UPV values ranged from 3968 m/s to 4156 m/s, while Rebound Hammer values ranged from 38 to 42, indicating consistent surface hardness. Carbonation depth ranged from 51 mm to 71 mm, particularly in few columns, where visible cracks were also observed. The half-cell potentiometer test (22 locations) showed a higher probability of reinforcement corrosion in these columns and in bathroom beams. Most roof beams and slabs showed no major visible defects during inspection.

The core test results (3 samples) showed equivalent corrected cube compressive strength ranging from 21.73–23.65 N/mm^2 (average ≈ 22.8 N/mm^2), indicating satisfactory concrete strength at the tested locations. All test results were found to be within the permissible limits of relevant IS codes. Overall, the structure was assessed to be mostly in sound condition, except for a few columns requiring rectification and suitable repair measures to address localized deterioration. The report recommended structural repair of the deteriorated columns and corrosion protection treatments, particularly in moisture-affected areas such as bathroom, and restoration works have been carried out accordingly.

Seismic Requalification: The Lakeside Workshop was taken up for detailed structural assessment as part of the redevelopment planning. Over the past decades, there have been significant revisions in Indian seismic design codes, making it necessary to undertake seismic requalification of existing structures to ensure their continued safety and compliance with current standards. Accordingly, a comprehensive structural evaluation was carried out using Finite Element (FE)–based analysis software. Both static and dynamic analyses were performed in accordance with the latest IS seismic codes to evaluate the structural response under updated loading conditions. In addition, static nonlinear analysis was conducted to better understand the structural behaviour under potential extreme loading scenarios and to assess the reserve strength and deformation capacity of the structure. Based on the results of these analyses, the structure was found to be structurally adequate and qualified for continued use under the revised seismic requirements.

Renovation strategies: Renovation strategies included reconfiguring the building layout to accommodate three modern laboratory facilities with updated flooring, partitions, and ceilings. Provisions were made for lab sinks, ventilators, split AC units, grid false ceilings, cable duct wiring, and aluminium partitions at designated locations. A steel mezzanine structure was integrated within the building to increase usable laboratory space, along with a steel staircase for internal access to the mezzanine level. Additionally, the existing structure was modified to suit the proposed layout, including selective removal and addition of walls as required by different Science groups to optimize space utilization.

Construction Aspects: The scope of works broadly included dismantling and demolition of old finishes, earthwork, structural steel work for the mezzanine floor, Reinforced Cement Concrete (RCC), reinforcement, brickwork, plastering, painting, various floorings, waterproofing treatments, removal of old wooden doors, rolling shutters, and windows, and provision and fixing of new steel doors, PVC doors, aluminium fabrication including Aluminium Composite Panel (ACP) work, installation of galvalume roofing sheets, installation of a deck slab system for the mezzanine floor as well as structural repair and strengthening of concrete members.

Electrical system & HVAC upgradation: To improve electrical safety, operational reliability, and energy efficiency, the laboratory electrical infrastructure has recently undergone a comprehensive upgrade. The major improvements implemented are outlined below:

- *Advanced Distribution Protection System:* The earlier SFU-based Power Distribution Boards (PDBs) have been upgraded to microprocessor-based MCCB/MCB protection systems**.** This provides enhanced protection, better fault detection, improved reliability, and easier monitoring of electrical loads.

- *Improved Fire-Safe Electrical Wiring:* The existing PVC wiring has been replaced with FRLSH (Flame Retardant Low Smoke Halogen) copper wiring**.** This upgrade significantly enhances fire safety by minimizing smoke generation and toxic emissions in case of electrical faults.

- *Energy-Efficient Lighting System:* The previous Fluorescent Tube Light (FTL) based illumination has been replaced with LED lighting. The new system provides better illumination quality, reduces energy consumption, and requires lower maintenance.

- *Installation of Energy-Efficient Air Conditioning:* Five-star rated split air conditioning systems have now been installed to maintain a stable working environment for both personnel and sensitive laboratory equipment while ensuring high energy efficiency.

- *Electrical Panel Capacity Enhancement:* The electrical panels have been upgraded to accommodate the increased power demand resulting from new equipment installations and the addition of air-conditioning systems, ensuring reliable and safe power distribution.

- *Benefits of the Upgrade:*
  - ➢ Improved electrical safety and protection
  - ➢ Enhanced reliability of power distribution
  - ➢ Increased energy efficiency
  - ➢ Better environmental control within the laboratory.
  - ➢ Provision for future load expansion.

Cost & time saving: This adaptive reuse project was completed at a cost of Rs. 310 lakhs compared to an estimated Rs. 1320 lakh for equivalent new construction, resulting in nearly 75% cost savings. In addition, the project was delivered within 1.5 years whereas new construction would have taken approximately 2.5 years resulting in 40 % of Time saving.

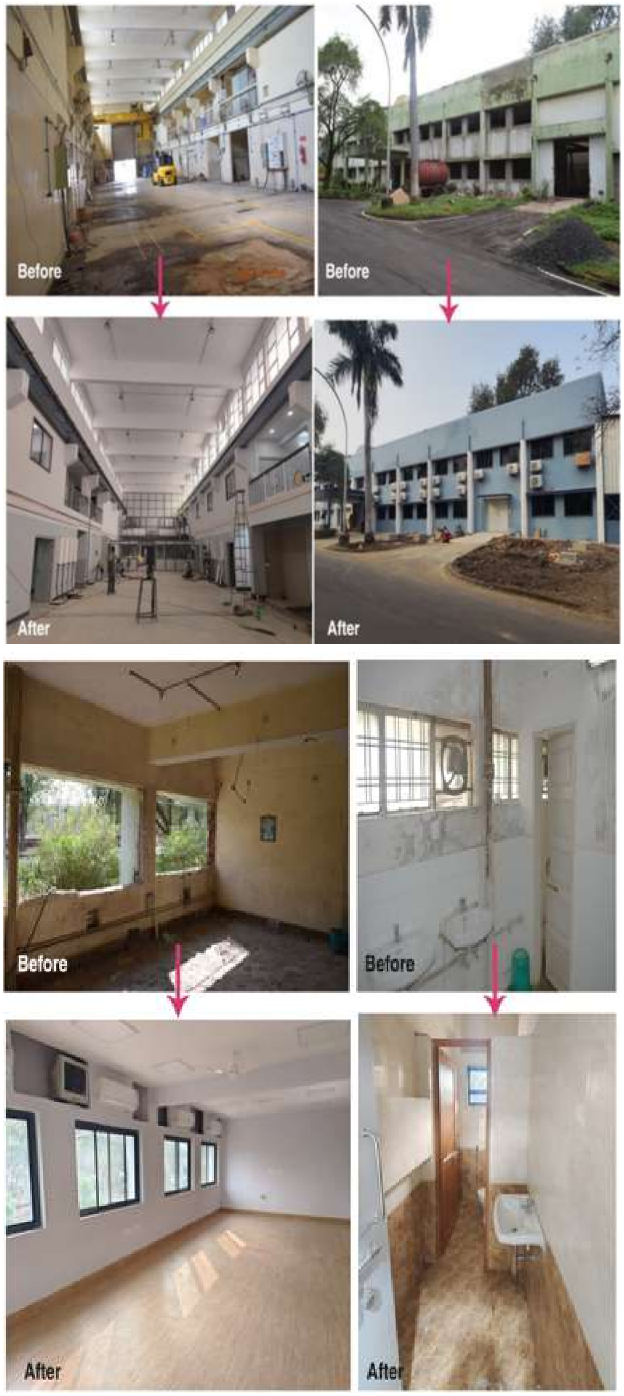

Before and after renovation of the facility

Reported by:
Bharat Kumar Rawlani (rawlani@rrcat.gov.in)

T.1: Unlocking the infrared frontier: Development of IR-FEL user facilities

L.S. Sharath Chandra, Shilpam Sharma, Ashish Khandelwal, Anudeep Singh and M. K. Chattopadhyay*

Free Electron Laser & Utilization Section
**Email: maulindu@rrcat.gov.in*

Abstract

The Raja Ramanna Centre for Advanced Technology (RRCAT), Indore houses a Free Electron Laser (FEL) developed in-house to lase in the wavelength region 12-50 μm, where the conventional sources fail to deliver a reasonable power. This region of electromagnetic spectrum is suitable for the study of resonant absorption of optical phonons, defects in semiconductors, non-linear dynamics, plasma resonances, low dimensional materials, polymers and their composites, etc. At present, macropulses of light coming from this FEL with a pulse repetition rate (PRR) 1-4 Hz and CW average power in excess of 5 mW (at 2 Hz PRR), with each macropulse consisting of about 200 micropulses of width 10 ps and separation about 33 ns, is available at the user laboratory for doing experiments. In the user laboratory, a Michelson interferometer has been developed to determine the wavelength of the FEL radiation. An infrared imaging set up has been developed to visualize the variation in the refractive index over the sample volume. The tunability of the FEL allows mode-selective imaging of samples for chemical finger printing within a solid. The pulsed nature of the FEL radiation can be utilized to perform time dependant experiments. In this article, the progress made in this direction is highlighted.

1. Introduction

Studies on the material properties in the mid and far infrared (IR) regions of the electromagnetic spectrum for wavelengths greater than 10 μm has been limited due to the lack of powerful sources. In this region of the electromagnetic spectrum, most of the commonly used materials either completely absorb the radiation through the n-phonon processes and/or optical phonon modes as in the case of non-metals, or completely reflect the radiation as in the case of metals. Over the past few decades, the development of FELs [1-3] and Synchrotron Radiation Sources (SRSs) delivering bright radiation in the IR regime has stimulated newer interest to unravel the novel properties in the fields of physics, materials science, chemistry, biology and medical sciences [4-8]. Several materials, e.g., the small gap semiconductors, polymers, low dimensional materials such as 2D-quantum materials and heterostructures are being explored both for photonic applications [9-12] and for their novel properties [13-17]. The refractive index of many of such materials in this wavelength range is quite large, which gives the scope for understanding the defect structure in the semiconductors and insulators. The FELs are the brightest sources for IR radiation with the added advantages of tunability of wavelength and ultra short pulse width. In this article, the experimental stations developed or being developed to study materials using the IR-FEL in RRCAT is presented.

2. Overview of FEL based IR sources

Conventional sources such as the black body or mercury arc lamp, radiate largely in the IR regime. These sources are widely used for spectroscopy experiments. Due to the lack of brightness, these sources offer a low signal to noise ratio [18], hindering, for example, the microscopic imaging at IR wavelengths. The SRSs offer white radiation at about three orders of magnitude higher brightness as compared to the conventional sources. In this case, the radiation is diffraction limited indicating that the spatial resolution can reach down to the size of the wavelength [18]. The IRFELs on the other hand, provide pulsed radiation with a pulse width down to a few ps at about three orders of magnitude higher brightness as compared to the SRSs. This allows a higher spatial resolution, beyond the diffraction limit [18]. Only a handful of such facilities are known to be available around the world, e.g, the FELIX in the Netherlands, FHI-FEL and FELBE in Germany, the Novosibirsk FEL in Russia, CLIO in France, FELiChEM in China, etc. [19]. In India, RRCAT is the first institute to develop a FEL working in the IR region, and it lases in the wavelength region 12-50 μm [19].

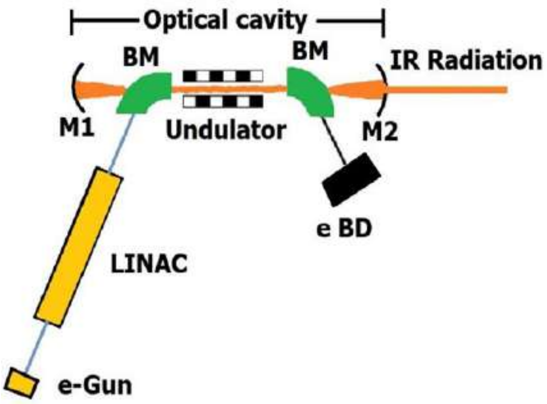

Fig. T.1.1: Schematic of an infrared free electron laser. e-Gun: electron gun; LINAC: linear accelerator; BM: bending magnet; M1, M2: mirrors; e BD: electron beam dump.

The schematic of an IRFEL is shown in Fig. T.1.1. The free electrons are generated using an electron gun (e-Gun) which is either a thermionic gun or a photo cathode gun [20, 21]. Then the free electrons in bunches are accelerated using a linear accelerator (LINAC) to about 10-30 MeV. Using bending magnets, these high energy electrons are made to pass through an undulator in which a series of alternating permanent magnets are placed. The electrons wiggle through these magnets due to the Lorentz force which alters their velocity. The change in the velocity of the electrons results in the spontaneous emission of IR radiation. In order to achieve the coherence or the lasing action, an optical cavity using one 100% reflecting mirror (M1) and a partially reflecting (~90%) mirror are introduced across the undulator. The length of the cavity is adjusted such that the incoming second electron bunch is in phase with the back-reflected radiation emitted from the first bunch. At the exit of the undulator, another bending magnet is used to take out the electrons from the optical path to dump them in a multilayered target (e BD). Details of the relation between the undulator parameter and the emitted radiation can be found in ref. [19].

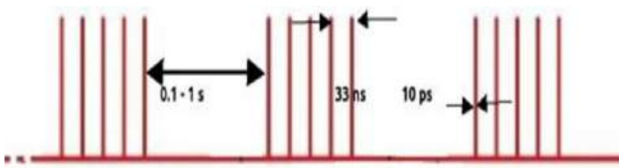

Fig. T.1.2: Pulse structure of an infrared free electron laser. Bunches of pulses are emitted at typically 1-10 Hz PRR.

Figure T.1.2 shows the typical pulse structure of the IR radiation emitted from an FEL. Due to the bunching of electrons in the LINAC and micro-bunching due to the interaction of the electric field of the wiggling elections bunches with that of the IR radiation inside the optical cavity, the IR output of the FEL consists of a series of bunches of pulses (macropulses) at 1-10 Hz PRR. Each macropulse thus consists of several micropulses of IR radiation.

3. Details of the IR-FEL functional at RRCAT

Figure T.1.3 shows the photograph of the IR-FEL developed at RRCAT [22]. The free electrons are accelerated to 18-25 MeV using a LINAC before feeding it to the undulator. The micropulse repetition rate can be selected between 29.75 MHz, 59.5 MHz or 119 MHz. The macropulse duration is 4-6 μs at present, with a PRR 1-4 Hz. The undulator for this FEL consists of 50 periods along its length, with a period length of 50 mm. The gap between the upper and lower jaws of the undulator can be varied between 27-40 mm [22] to vary the undulator parameter K_u from 1.2-0.5.

The wavelength of the radiation from the IR-FEL at RRCAT can be tuned in the wavelength range 12-50 μm by varying the undulator gap and the accelerated electron energy as shown in the Fig. T.1.4. It can be seen that two different electron energies viz., ~24 MeV and ~18 MeV are sufficient to cover the entire range of wavelengths. The brightness of the emitted radiation is in the range of 10^{14} photons/s/mm^2/mrad^2/0.1% BW which, for this wavelength range, is four orders of magnitude higher than the Indus SRS at RRCAT [23].

Fig. T.1.3: Photograph of the IR-FEL at RRCAT which lases at 12-50 μm.

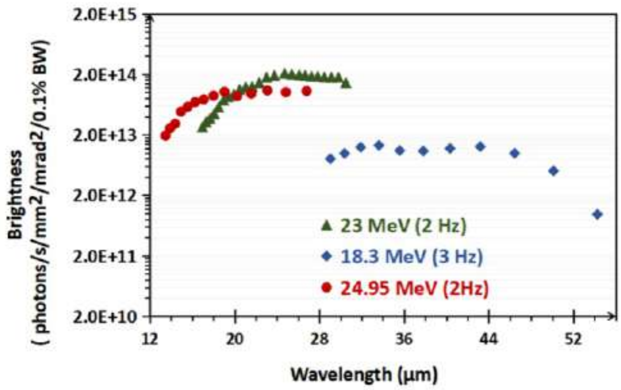

Fig. T.1.4: Brightness of IR-FEL radiation in the wavelength range 12-50 μm.

The stability of the radiation power over the duration of the user experiments has been ascertained by measuring the power delivered at the user laboratory over 6 hours. Figure T.1.5 shows this measured IR power at the user laboratory as a function of time. It is seen that the variation of power over 6 hours is less than 4% [23].

4. The IR-FEL beamline at RRCAT

The IR radiation emitted from a 3.5 mm aperture of the IR-FEL is transported over 60 m to the user laboratory through reflective optics (plane and spherical gold coated mirrors). A small portion of the beam is tapped at the exit port of the IR-FEL using a KRS beam splitter to measure the generated power. The beam lines are filled with dry nitrogen gas to avoid absorption due to atmospheric moisture. As shown in the Fig. T.1.6, six ports have been constructed for doing experiments using the radiation from the IR-FEL.

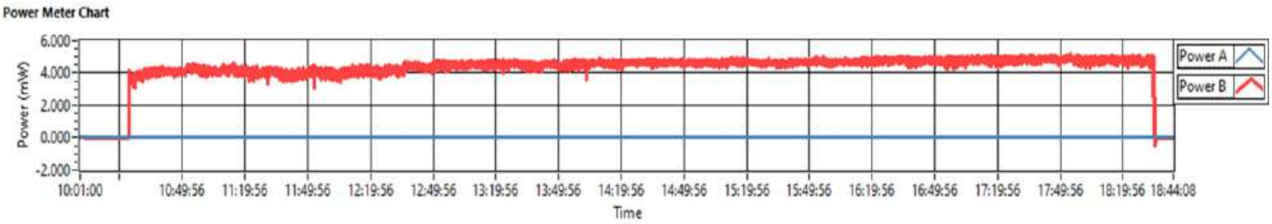

Fig. T.1.5: Stability of the radiation emitted from IR-FEL, as measured at the user laboratory.

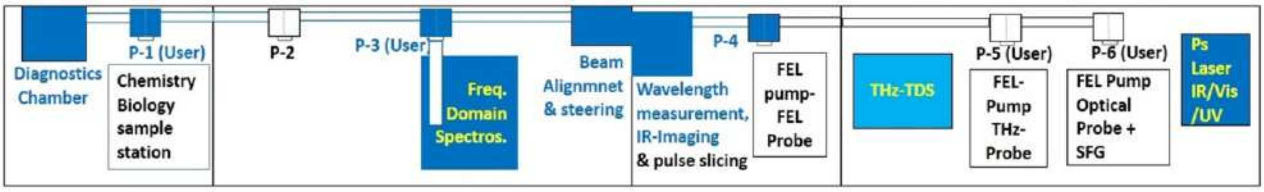

Fig. T.1.6: The IR beam line at the user laboratory rooms with exit ports. The blue colour indicates the facilities already in use.

5. Current and upcoming user facilities

A series of experimental platforms/stations are planned in the user laboratory. Some of them are completed, and are in use, while some of the others are under development, as discussed in the next subsections.

a. Michelson interferometer

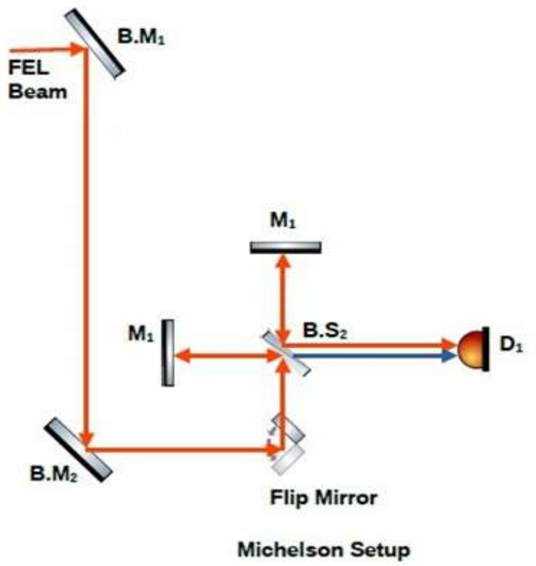

Fig. T.1.7: Schematic of the Michelson interferometer in the IR-FEL facility. B.M, M: Mirror; B.S: Beam splitter; D: detector.

An interferometer is an integral part of the optics laboratory where two beams of same source is made to superimpose to get the interference pattern. It is used to determine the spectral components of a white light source, as used for Fourier transform infrared (FTIR) spectroscopy, microscopic surface irregularity studies, or even for detecting gravitational waves. Since, the FEL emits monochromatic radiation, an interferometer is useful to know the central wavelength, wavelength spread, coherence length and side bands if any etc.

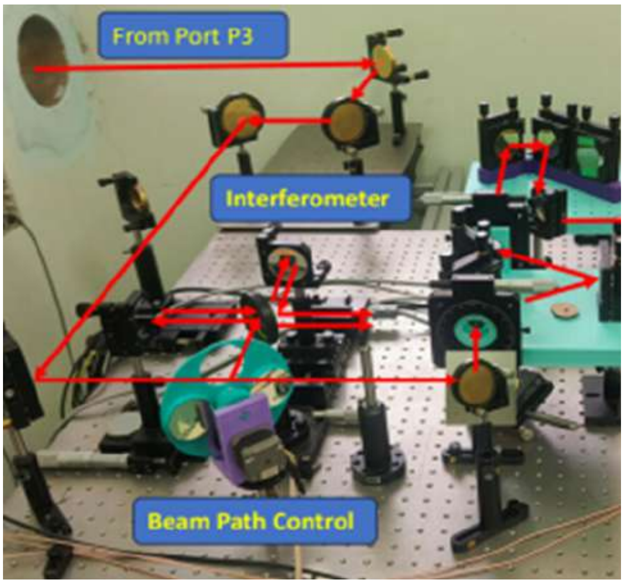

Fig. T.1.8: Michelson interferometer developed to characterize the IR-FEL radiation. Pyroelectric detectors are used for the detection of radiation. Double side polished high resistivity silicon is used as beam splitter. Gold coated copper mirrors are used as reflective optics.

One of the simplest interferometers to realize is the Michelson interferometer. Figure T.1.7 shows the schematic of the Michelson interferometer, where the mirrors M1 and M2 are placed at equal distance from the beam splitter. One of the mirrors is moved in small steps over a specified length around the mean distance. By moving the mirror, a path difference is created between the two beams reflected by mirror M1 and M2 to introduce a phase difference between these two radiations leading to interference. The intensity of the IR beam is measured in small steps of the mirror movement. Figure T.1.8 shows the photograph of the Michelson interferometer developed to characterize the IR-FEL radiation. Pyroelectric detectors are used for the measurement of the wavelength of the radiation. Double side polished high resistivity silicon is used as beam splitter. Gold coated copper mirrors are used as reflective optics.

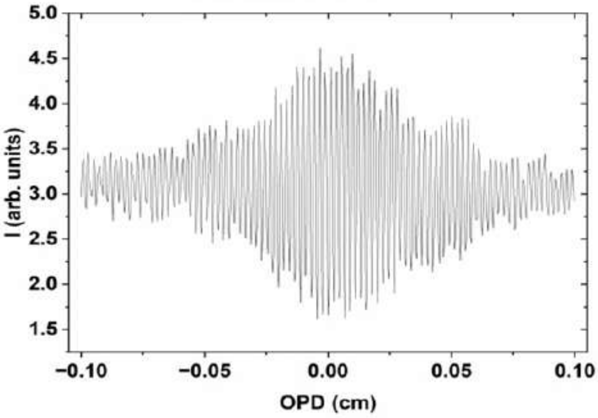

Fig. T.1.9: Interferogram from the IR-FEL radiation measured using Michelson interferometer.

The intensity as function of path difference is shown in Fig. T.1.9. The Fourier transform of the interferogram gives the IR-FEL light spectrum, which is shown in Fig. T.1.10. The central wavelength (λ) for this experiment is 22.26 μm. The full width at half maximum ($\Delta\lambda$) is 0.32 μm, which indicates the high monochromaticity of the IR-FEL light.

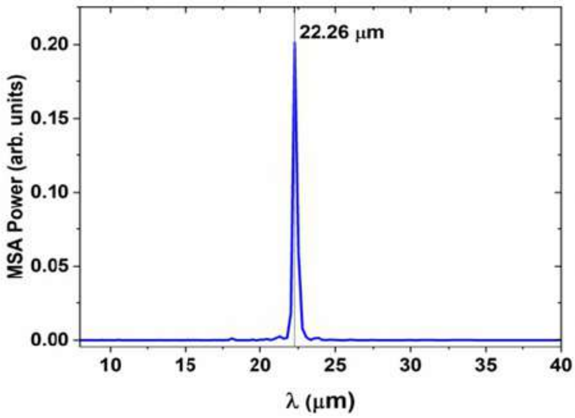

Fig. T.1.10: Fourier transform of the interferogram shown in Fig. T.1.9 showing a typical IR-FEL light spectrum that depicts its monochromaticity.

b. Temperature and magnetic field dependence in IR absorption spectroscopy

Non metallic solids often show strong broad band absorption in the 12-50 μm range, leading to poor signal to noise ratio in the transmission spectra measured in a FTIR spectrometer using conventional sources. Due to this, resonant transitions (if any) may be buried under the noise if the conventional sources are used. On the other hand, measurements under a pulsed magnet is impossible using a FTIR spectrometer. In such extreme conditions, radiation from FEL is valuable to study the novel properties of materials especially in the semiconductors and insulators [13, 14, 24].

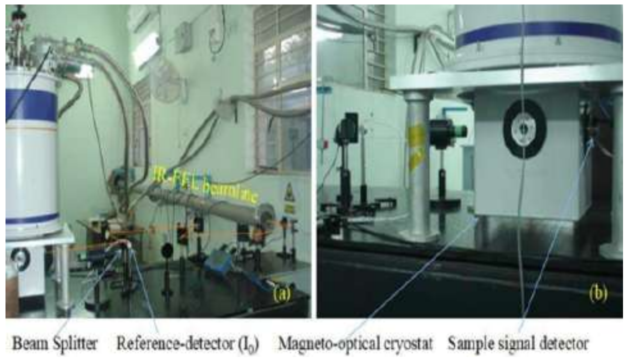

Fig. T.1.11: Experimental set up used to measure the IR-FEL light absorption as a function of temperature and magnetic field.

Figure T.1.11 shows the photograph of the set up used for measuring IR absorption as a function of temperature and magnetic field using the radiation from the IR-FEL at RRCAT. The temperature of the sample can be varied from 300 K to 10 K in the presence of magnetic field up to 7 T using a cryogen free magnet cryostat system.

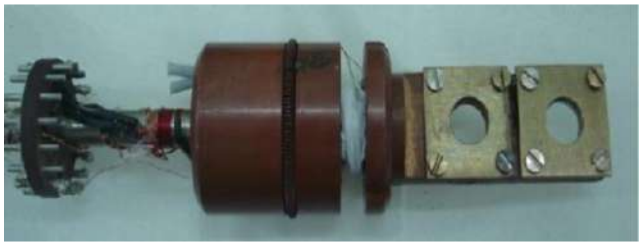

Fig. T.1.12: Photograph of the sample holder attached to the insert used for loading samples inside the cryostat shown in Fig. T.1.11.

Figure T.1.12 shows the sample mounting stage of the cryostat-insert used for measuring IR-FEL light absorption as a function of temperature and magnetic field. It consists of a copper plate with two circular apertures for mounting the sample and the reference. The reference for the bulk samples is the blank aperture. In the case of thin films, an identical substrate is used as the reference. A silicon beam splitter is used for dividing the IR radiation into the reference beam and the probe beam. A pyroelectric detector is used to measure the intensity of the incident radiation (reference detector). Another pyroelectric detector is used to measure the transmitted radiation through the sample as well as the through the reference aperture (sample signal detector). A stepper motor is used for moving the sample and the reference aperture across the beam path inside the cryostat. The transmittance is estimated as the ratio of intensities of transmitted radiation through the sample to that transmitted through the reference aperture. Before finding this ratio, both the intensities are normalised to the incident power.

V_2O_3 is a classic material studied over decades [25]. It undergoes a metal to an insulator transition (MIT) along with a structural transition when the temperature is decreased below 150 K [26]. It was observed that the MIT can also be tuned with pressure, composition, electric field and photon energy [27-30]. Figure T.1.13(a) shows the temperature dependence of electrical resistance across the MIT. The thermal hysteresis (between warming and cooling runs) near 150 K indicates that the transition is of first order.

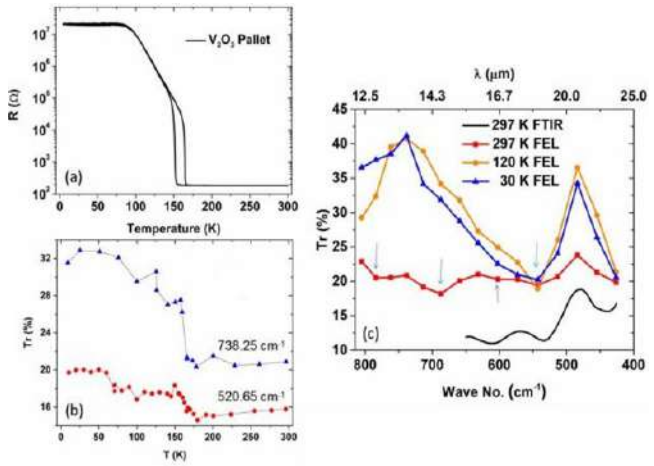

Fig. T.1.13: (a)Temperature dependence of electrical resistivity of V_2O_3. A first-order high temperature metal to low temperature insulator transition is observed near 150 K. (b) Transmission of IR-FEL light at 520.65 cm^{-1} and 738.25 cm^{-1} wave numbers through bulk V_2O_3 as a function of temperature. (c) Transmission spectra of bulk V_2O_3 as a function of wavelength (wave number) at different temperatures. For comparison, the data from FTIR spectroscopy are also plotted.

Figure T.1.13(b) shows the temperature dependence of transmittance at 520.65 cm^{-1} and 738.25 cm^{-1}. At both the frequencies, the transmittance changes across the MIT. However, the changes are minimal around 520.65 cm^{-1} and much larger near 738.25 cm^{-1} as the mode near the latter wave number is strongly dependent on temperature while that near the former wave number is not. This temperature dependence of the modes is clearly seen in Fig. T.1.13(c). The transmittance curve(s) in Fig. T.1.13(b), however, nearly mimic the temperature dependence of electrical resistivity as expected.

Figure T.1.13(c) shows the frequency dependence of IR-FEL light transmission at different temperatures. For comparison, the data obtained from the conventional FTIR spectrometer is also shown. One can observe that the transmission at a given frequency is higher for the FEL radiation in comparison with that measured using conventional FTIR spectrometer. This may be due to the interaction of the high electric field of the IR-FEL radiation with the sample. The high electric field may induce partial phase transformation to the insulating phase, or it may also induce nonlinear effects in the sample. Further studies are required to ascertain the origin of the excess transmission of FEL radiation. In this figure, various absorption modes are marked by arrows. As the temperature is decreased below the MIT, the transmittance increases due to the development of the insulating phase. These results suggest that in systems undergoing phase transitions, the temperature (and similarly magnetic field) dependence of transmittance can provide valuable information on their physical characteristics.

c. Infra-red imaging

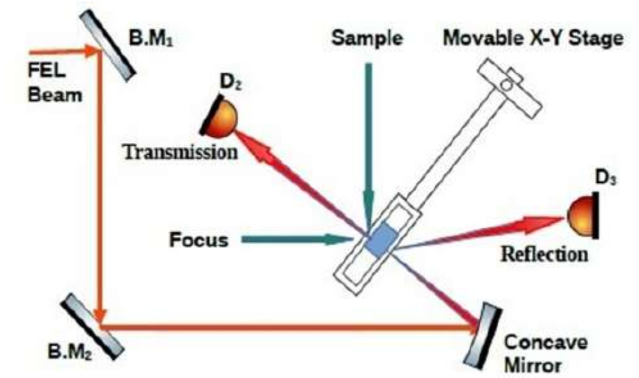

Fig. T.1.14: Schematic of the imaging set up. Images can be obtained both in the transmission and reflection modes.

Imaging using IR radiation is useful in studying composite materials. Use of FEL has two major advantages in imaging studies. (a) The brightness of the FEL light is several orders of magnitude higher than that of the conventional sources: this enhances the signal to noise ratio [18]. (b) The precise wavelength selectivity [31]: the wavelength can be tuned to specific characteristic excitations of the different compositions of the composites. For example, different pollutants present in soil [31], carbon-fibre reinforced polymers [10], interaction of reactive materials with a substrate [32], can be imaged to study the composition, defects, and/or reactions. Another advantage of imaging using IR-FEL light is that the materials that are opaque to the visible light, but transparent to IR radiation, can give information about the microstructures buried inside the sample [33]. Keeping such applications in mind, an IR-FEL light based imaging facility has been developed in the user laboratory.

Figure T.1.14 shows the schematic of the imaging set up. The IR beam is focused on the sample using spherical concave/parabolic mirrors. The sample is scanned in X and Y direction using stepper motor controlled mechanical stages. The images can be obtained both in the transmission and reflection modes. The resolution of the image depends on how tightly one can focus the light. Figure T.1.15 shows the convergence of the IR-FEL light from a spot size of (a) 17 × 13 mm to (b) 0.8 × 1 mm.

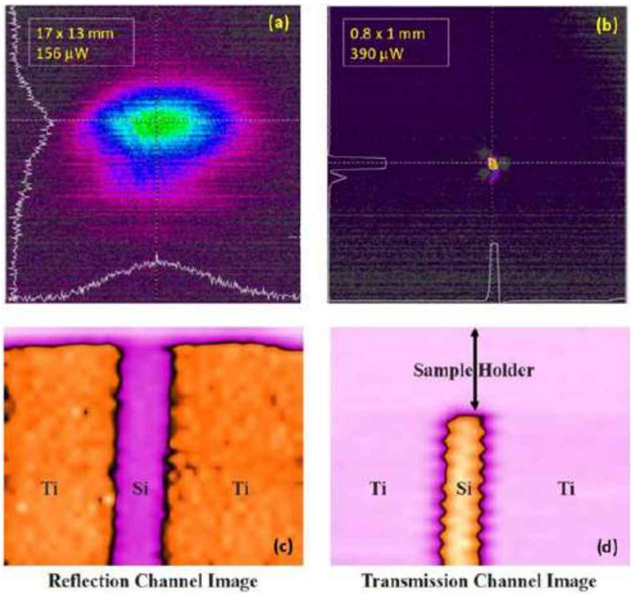

Fig. T.1.15: Focusing of the IR-FEL light from a spot size of (a) 17 × 13 mm to (b) 0.8 × 1 mm. (c) & (d) IR imaging of 100 nm thick, patterned Ti thin film on silicon substrate.

An example of imaging using this set up is shown in Fig. T.1.15. The sample under study is a 100 nm thick, patterned Ti thin film on silicon substrate. The image is obtained both in the (c) reflection and (d) transmission modes. Orange colour represents the maximum intensity measured, while pink represents the lowest measured intensity. A spatial resolution ~300 μm has been achieved in this set-up. The contrast seen in the panels (c) and (d) is due to the reflection of IR radiation from the free electrons within the Ti layer.

While the above-mentioned experimental facilities are already available for the users, more experimental stations are being developed for future use. In the following subsections, some of these activities are discussed.

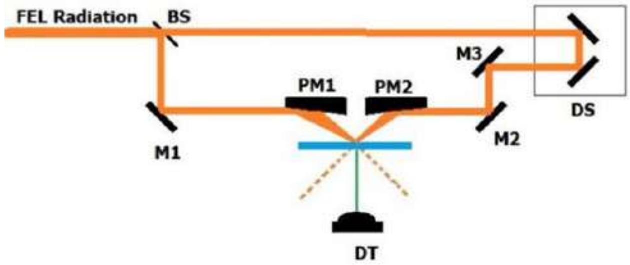

Fig. T.1.16: Schematic of the set up for second harmonic generation. BS: beam Splitter; M: Mirror; DS: Delay stage; PM: Parabolic mirror; DT: Detector; Blue rectangular slab: the sample.

d. Second harmonic generation using IR-FEL light

The high power of the IR-FEL can be used to explore the non-linear dynamics of small gap semiconductors and nano-structures [11, 12], e.g, CdSe, CdTe, ZnTe, Te, GaSe, $AgGaSe_2$, $AgGaTe_2$, $LiGaTe_2$, etc. Using second harmonic generation, CdTe may also be used in future as an autocorrelator device to study the IR-FEL pulse shape and thereby to tune the IR-FFL for increased monochromaticity. Figure T.1.16 shows the schematic of the set up required for second harmonic generation using a non-linear crystal (blue slab). The radiation is equally divided into two arms using a beam splitter such as high resistivity Si or a wire grid polarizer. A delay stage is attached to one of the arms. Both the beams are focused on the same location of the sample making equal angle to the normal of the sample. Both the beams are blocked after transmitting through the sample. The detector is placed at the plane normal to the radiation spot. The maximum intensity is obtained when the delay between two arms is zero. Such an experimental set up serves two purposes. Firstly, the nonlinear properties of new crystals can be studied, and secondly, it can be used to experimentally study the IR-FEL light pulse structure as stated above. The experimental set-up required for this is currently being built.

e. Pump-probe spectroscopy

A variation to the second harmonic set-up can be used to study the time evolution of a particular excitation [34-38] using the IR-FEL light. The measurements can be either one-colour [39-41] or two-colour [37, 41]. The choice of the method (one-colour or two-colour) and the energy of the pump beam is selected on the basis of the excitation to be studied. A relatively simple pump-probe set up being developed for the IR-FEL light is for FEL-pump FEL-probe spectroscopy (one-colour). In the case of two-colour pump-probe spectroscopy, a conventional pulsed laser and the IR-FEL need to be synchronized. This requires corrections for the phase error and very low timing jitters.

(i) IR-FEL-pump IR-FEL-probe spectroscopy

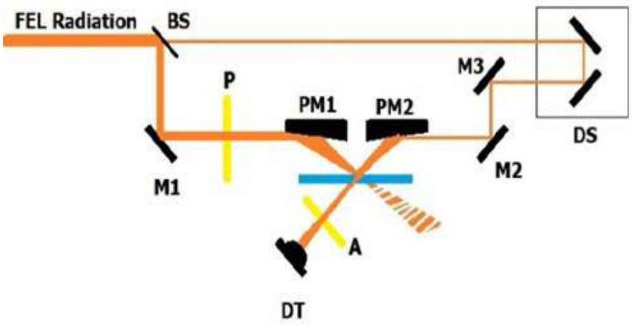

Fig. T.1.17: Schematic of the set up for FEL-pump FEL-probe spectroscopy. BS: beam Splitter; M: Mirror; DS: Delay stage; PM: Parabolic mirror; P: Polarizer; A: Analyser; DT: Detector; Blue rectangular slab: the sample;

Figure T.1.17 shows the schematic diagram of the one-colour pump-probe spectroscopy set up using the IR-FEL light. In this case most of the radiation (>90%) is used for pumping the sample, while a small amount of radiation (< 10%) is taped out using a beam splitter to probe the transmittance or reflectance from the sample as a function of the time delay between the probe beam and the pump beam incident on the sample. The set up is mostly ready, where qualifying experiments are currently being conducted.

(ii) IR-FEL-pump THz-probe spectroscopy

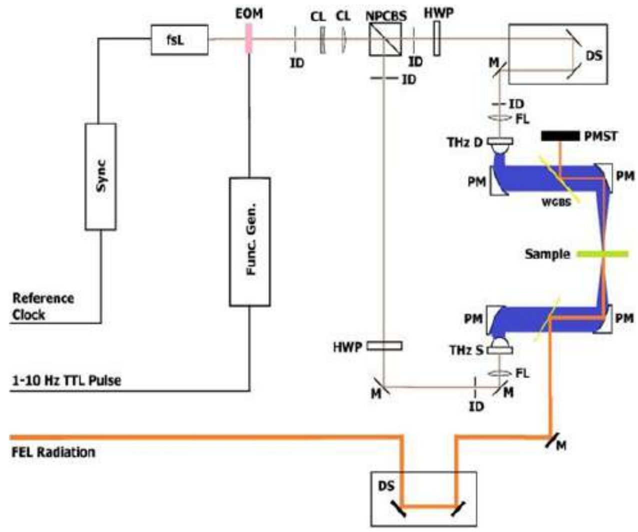

Fig. T.1.18: Schematic of the set up for IR-FEL-pump THz-probe spectroscopy. Sync: Synchronization (optoelectronic); fsL: femto second laser; Func. Gen: Arbitrary function generator; EOM: electro-optical modulator; ID: Iris disk; CL: collimating lens; NPCBS: non polarising cube beam splitter; HWP half wave plate; THz S: Terahertz source antenna; THz D: Terahertz detector antenna; PM: parabolic mirror; M: plane mirror; WGBS: wire grid beam splitter; PMST: Beam stopper.

Figure T.1.18 shows the schematic of the set up to be used for the IR-FEL-pump THz-probe experiments. This two-colour pump-probe spectroscopy requires the synchronization of a femto second laser (fsL) with the master clock of the FEL using optoelectronic synchronization system (Sync). The fsL light shall be used for THz (probe) generation and detection using antenna structures. Employing electro-optic modulation, a reference trigger pulse from the IR-FEL timing system shall be used to select a time window for THz generation and detection. Such a setup is presently being conceptualized at the IR-FEL user facility, and is expected to be developed by the end of 2029.

f. Photo-conductivity experiments using IR-FEL

The intense nature of the radiation from the IR-FEL can also be utilized to study the light induced electronic excitations in materials [13, 16]. In this case, the DC transient current will be measured as a function of time after irradiation with the IR-FEL light. In most of the cases, the induced current persists over few tens of μs or even up to a few seconds. Photoconductivity in the small gap semiconductors such as doped GaAs, doped Si and Ge, $Hg_{1-x}Cd_xTe$, $Pb_{1-x}Sn_xTe$, Kondo insulators such as SmB_6 and YbB_{12} have been studied using IR radiation from FEL sources [13, 16]. The photo-current is measured as a function temperature, magnetic field, wavelength and/or with respect to a specified time delay from the time of incidence of the radiation. In some samples such as graphene, transients may be quite fast so that the current may reach background levels within a few ps [17, 42]. Since, the decay of the photocurrent is fast, the current needs to be converted to voltage using a RF transimpedance amplifier and needs to be measured using a high-speed oscilloscope. A schematic of the required set-up is shown in Fig. T.1.19. This experimental set up is currently under development and will be available for measurements in near future.

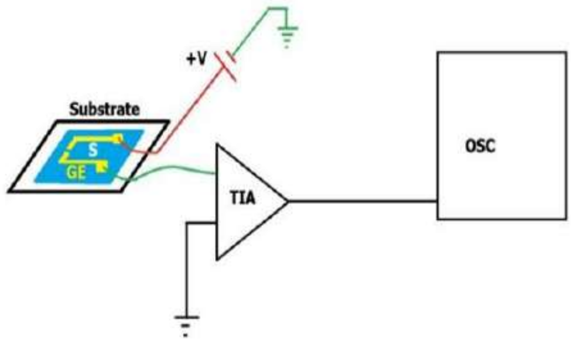

Fig. T.1.19: Schematic of the set up for the photo-conductivity experiments. S: Sample; GE: Gold contacts; TIA: RF Transimpedance Amplifier; OSC: Oscilloscope.

6. Conclusion

An IR-FEL lasing in the mid-far IR range (12-50 μm wavelength), is functional at RRCAT. Experimental measurements performed over more than six hours show that the power stability of the IR-FEL radiation in the user laboratory is better than 4%. The wavelength characterization of this radiation has been performed using a Michelson interferometer developed in-house. A Single peak with less than 1.5% full width at half maximum has been observed, indicating the monochromaticity of the IR-FEL light. Two experimental stations developed and commissioned at the IR-FEL users facility have been used for studies by in-house as well as outside RRCAT users. A set up to measure the wavelength selective absorption/transmission as a function of temperature and magnetic field is in regular operation, and results of preliminary studies indicating photon induced excess transmission in V_2O_3 is presented. The features of the IR-FEL based imaging facility developed in-house to study composite materials for distinguishing differences in chemical composition, changes in the dielectric constant and for detecting buried layers of polymers opaque to visible radiation but transparent to IR have also been discussed. Several upcoming facilities such as second harmonic generation, time domain and photoconductivity measurement set ups are discussed in detail. With these developments, the IR-FEL establishment in RRCAT is shaping up into a unique experimental facility for research in different fields of science, including physics, materials science, chemistry and biology.

References

[1] B. N. Murdin, Contemporary Phys. 50, 391 (2009)

[2] J. E. Walsh, Proc. SPIE, 666, 22 (1986)

[3] C. A. Brau, Science 239, 1115 (1988)

[4] W. M. Dennis, J. Optical Soc. Ame. B 6, 1045 (1989)

[5] D. D. Dlott, and M. D. Fayer, IEEE J. Quanum Electron. 27, 2697 (1991)

[6] G. S. Edwards, S. J. Allen, R. F. Haglund, R. J. Nemanich, B. Redlich, J. D. Simon, and W. C. Yang, Photochem. Photobio. 81, 711 (2005)

[7] F. Vatansever, M. R. hamblin, Photonics Lasers med. 4, 255 (2012)

[8] T. Kawasaki, A. Nagase, K. Hayakawa, F. Teshima, K. Tanaka, H. Zen, F. Shishikura, N. Sei, T. Sakai, and Y. Hayakawa, ACS Omega 10, 13860 (2025)

[9] H. Chen, L. Gao, Z. Qin, Y. Ge, K. Khan, Y. Song, G. Xie, S. Xu, H. Zhang, Appl. Mater, Today 21, 100800 (2020)

[10] L. Senni, S. Laureti, M. K. Rizwan, P. Burrascano, D. A. Hutchins, L. A. J. Davis, and M. Ricci. NDT and E Inter. 102, 281 (2019)

[11] H. Zen, R. Hajima, and H. Ohgaki, Sci. Rep. 13, 6350 (2023)

[12] W. Schollkopf, S. Gewinner, H. Junkes, A. Paarmann, G. v. Helden, H. Bluem, A. M. M. Todd, Proc. SPIE, 9512, 95121L (2015)

[13] J. Kaminski, J. Spector, W. Pretti, and M. Weispfenning, Appl. Phys. Lett. 52, 233 (1988);

[14] A-L. Barra, M. Goiran, R. Sessoli, and S. A. Zvyagin, Comp. Ren. Phys. 14, 106 (2013);

[15] S. P. Horvath, J.-P. R. Wells, A. F. G. van der Meer, and M. F. Reid, Optical Mater. 66, 8 (2017);

[16] M. A. W. van Loon, N. Stavrias, N. H. Le, K. L. Litvinenko, P. T. Greenland, C. R. Pidgeon, K. Saeedi, B. Redlich, G. Aeppli, and B. N. Murdin, Nat. Photon. 12, 179 (2018);

[17] M. Mittendorff, J. Kamann, J. Eroms, D. Weiss, C. Drexler, S. D. Ganichev, J. Kerbusch, A. Erbe, R. J. Suess, T. E. Murphy, S. Chatterjee, K. Kolata, J. Ohser, J. C. K. Otto, H. Schneider, M. Helm, and S. Winnerl, Optics Express 23, 28728 (2015)

[18] T. I. Smith, Nucl. Instrum. Methods Phys. Res. A 483, 565 (2002)

[19] S. Chandran, R. S. Saini, S. Lal, T. Dave, B. Biswas, A. Kumar, U. Kale, S. K. Gupta, S. Sharma, A. Singh, K. K. Pant, V. Kumar, Nucl. Instrum. Methods Phys. Res. A 1084, 171214 (2026)

[20] S. Krishnagopal and Vinit Kumar, Rad. Phys. Chem. 70, 559 (2004)

[21] T. Asaka, H. Ego, H. Hanaki, T. Hara, T. Hasegawa, T. Hasegawa, T. Inagaki, T. Kobayashi, C. Kondo, H. Maesaka, S. Matsubara, S. Matsui, T. Ohshima, Y. Otake, T. Sakurai, S. Suzuki, Y. Tajiri, S. Tanaka, K. Togawa, and H. Tanaka, Phys. Rev. Accel. Beams 20, 080702 (2017)

[22] K. K. Pant, V. Kumar, B. Biswas, A. Kumar, S. Lal, S. Chandran, S. K. Gupta, Md. Khursheed, P. Nerpagar, A. K. Sarkar, R. K. Pandit, K. Ruwali, K. Sreeramulu, S. Das, R. S. Shinde, S. Chouksey, J. K. Parate, V. Bhanage, P. P. Deshpande, S. Tiwari, M. Joshi, L. Jain, A. Valecha, A. Pathak, M. A. Ali, H. R. Bundel, P. Shrivastava, T. Reghu, U. Kale, Y. Wanmode, P. Mohania, J. Mulchandani, A. Patel, M. Acharya, A. Mahawar, M. Lad, M. K. Jain, N. Tiwari, P. S. Bagduwal, V. G. Sathe, S. Joshi, R. Shiroman, A. S. Yadav, R. Kumar, A. Singh, V. K. Dwivedi, M. Borage, and S. R. Tiwari, Cur. Sci. 114, 367 (2018)

[23] M. K. Chattopadhyay, B. Biswas, S. Sharma, A. Khandelwal, S. Chandran, L. S. Sharath Chandra, T. Dave, R. S. Saini, S. Lal, A. Kumar, U. Kale, S. K. Gupta, R. K. Pandit, H. N. Sidam, P. Nerpagar, A. Chakraborty, R. K. Meena and K. K. Pant, Curr, Sci. 128, 710 (2025)

[24] C. J. G. M. Langerak, L. Li, L. Van Bockstal, A. Ardavan, M. J. van de Pol, A. F. G. van der Meer, F. Herlach, H. U. Mueller, R. J. Nicholas, and J. Singleton, Physica B 246-247, 400 (1998)

[25] S. Y. Kim, M.-C. Lee, G. Han, M. Kratochvilova, S. Yun, S. J. Moon, C. Sohn, Je-G. Park, C. Kim, and T. W. Noh, Adv. Mater. 30, 1704777 (2018)

[26] C. Huang, A. Rakshit, G. Janka, Z. Salman, A. Suter, T. Prokscha, B. A. Frandsen, and Y. Kalcheim Adv. Electron. Mater. 11, 2500028 (2025)

[27] I. Valmianski, J. G. Ramirez, C. Urban, X. Batlle, and I. K. Schuller, Phys. Rev. B 95, 155132 (2017)

[28] P. Homm, M. Meghini, J. W. Seo, S. Peters, and J. P. Locquet, APL Mater. 9, 021116 (2021)

[29] P. Hansmann, A. Toschi, G. Sangiovanni, T. Saha-Dasgupta, S. Lupi, M. Marsi, and K. Held, Phys. Status Solidi B 250, 1251 (2013)

[30] F. Giorgianni, J. Sakai, and S. Lupi, Nat. Commun. 10, 1159 (2019)

[31] Y. Cheng, H. sun, E. Yang, J. Lv, B. Wen, F. Sun, L. Luo and Z. Liu, J. Hazard. Mater. 411, 125129 (2021)

[32] S. G. Kazarian, and K. L. A. Chan, Macromolecules, 37, 579 (2004)

[33] D. M. Mittleman, Opt. Exp. 26, 9417 (2018)

[34] N. Mori, The Rev. Laser Engg. 31, 818 (2003)

[35] J. Kono, A. H. Chin, A. P. Mitchell, T. Takahashi, and H. Akiyama, Appl. Phys. Lett. 75, 1119 (1999)

[36] M. A. Zudov, A. P. Mitchell, A. H. Chin, and J. Kono, J. Appl. Phys. 94, 3271 (2003)

[37] G. A. Khodaparast, D. C. Larrabee, J. Kono, D. S. King, J. Kato, T. Slupinski, A. Oiwa, H. Munekata, G. D. Sanders, and C. J. Stanton, J. Appl. Phys. 93, 8286 (2003)

[38] G. A. Khodaparast, D. C. Larrabee, J. Kono, D. S. King, S. J. Chung, and M. B. Santos, Phys. Rev. B 67, 035307 (2003)

[39] M. Broquier, H. Dubost, R. Kolos, J. Lefevre, and A. Tramer, J. M. Ortega, J. M. Berset, A. Peremans, AIP Conf. Proc. 364, 154 (1996)

[40] H. A. Hafez, S. Kovalev, K.-J. Tielrooij, M. Bonn, M. Gensch, and D. Turchinovich, Adv. Optical Mater. 8, 1900771 (2020)

[41] S. P. Horvath, J.-P. R. Wells, A. F. G. van der Meer, and M. F. Reid, Optical Mater. 66, 8 (2017); J. M. Ortega, Nucl. Instrum. Methods Phys. Res. A 507, 8 (2003)

[42] M. Mittendorff, S. Winnerl, J. Kamann, J. Eroms, D. Weiss, H. Schneider, and M. Helm, Appl. Phys. Lett. 103, 021113 (2013)

T.2: LIBS: A laser based tool for elemental analysis of materials

Sunita Ahlawat*, **Diksha Garg, B. N. Upadhyaya, and P. K. Mukhopadhyay**

Advanced Laser Development & Applications Division, RRCAT

**E-mail: rsunita@rrcat.gov.in*

Abstract

Laser-Induced Breakdown Spectroscopy (LIBS) is a versatile technique used for elemental analysis. It works by focusing a high-energy pulsed laser on a sample surface to create a tiny plasma, and the spectral analysis of light emitted from this plasma provides information about the elements present in the material. LIBS can detect almost all elements in the periodic table, including low atomic number (low-Z) elements, and requires a little to no sample preparation. It enables rapid, real-time analysis and also allows stand-off measurements from several meters away. The technique is quasi-non-destructive, as it removes only a very small amount of material (~100's of micron), and it can be used for solids, liquids, and gases under ambient, vacuum, or controlled environments. In addition, LIBS systems can be made portable and used with fiber-optic probes, making them suitable for field applications. In ALDAD, RRCAT, several LIBS setups have been developed, each suitable for specific applications including in-situ measurements, stand-off analysis over several meters, and for use in difficult-to-access or hazardous environments. In this theme article, an overview of the various LIBS systems and analysis approaches for material characterization developed at RRCAT, has been presented.

1. Introduction

Laser-Induced Breakdown Spectroscopy is an optical emission spectroscopy technique that enables direct elemental analysis of samples through spectroscopic analysis of laser induced plasma. In this technique, an energetic pulsed laser is focused on a sample surface, producing irradiance of the order of 10^{10}-10^{11} W/cm^2. When this irradiance exceeds the breakdown threshold of the sample material, the rapidly deposited energy leads to intense localized heating, causing melting and vaporization of the surface, followed by ionization of the ablated vapor. This results in formation of a transient plasma composed of atoms, ions, electrons, and clusters. The plasma is very hot in the beginning and emits broadband light called continuum. As the plasma cools down, distinct atomic and ionic spectral lines begin to appear in the plasma emitted light. The spectroscopic analysis of this radiation provides elemental information about the sample.

Although the early demonstrations of LIBS dates back to 1960s [1], soon after the invention of laser, but its initial applications mainly utilized the plasma as a source for spark-based methods. Interest in LIBS was revived in the 1980s with advancements in laser and spectroscopic technologies. However, still the laser and spectrometer systems used in early LIBS systems were bulky and suitable for laboratory applications. In addition to hardware limitations, difficulties in handling and interpreting the LIBS data, which is often huge and complex, made LIBS analysis challenging and limited its wider use. Recent technological advancements have led to the development of compact and efficient flash lamp pumped lasers. Further, alternate laser sources such as diode-pumped solid-state (DPSS) lasers, fiber lasers, and microchip lasers, which require less cooling, consume less power, and reduce overall LIBS system size, are also being explored. Similarly, improvements in spectrometers have made it possible to use compact single or multi-channel Czerny–Turner spectrometers that can detect the required wavelength range with sufficient resolution. In addition, the use of machine learning techniques has made it easier to analyse complex LIBS data, enabling faster and more reliable results. All these technological advancements have transformed LIBS from a laboratory-based technique into a robust and portable tool suitable for field use.

When compared to other conventional elemental analysis techniques, LIBS offers several advantages. For example, inductively coupled plasma optical emission spectroscopy (ICP-OES) usually requires extensive sample preparation, such as digestion and dilution, and is a bulky laboratory instrument, making it difficult to use in the field. Similarly, X-ray fluorescence (XRF) has poor sensitivity for low atomic number elements. Further, both techniques generally require the sample to be placed close to the instrument and cannot perform analysis of remotely placed samples. In contrast, LIBS requires minimal or no sample preparation, and can detect almost all periodic table elements, including low atomic number elements. It can also perform remote (stand-off) measurements over distances of several meters, allowing its use in harsh or hazardous environments and making it highly suitable for field applications. These advantages have enabled LIBS applications across diverse fields, including environmental monitoring of heavy metals and trace elements, geological and planetary exploration for elemental characterization, and industrial process monitoring for alloy identification and quality control [2]. More recently, it has gained attention in nuclear field for fuel characterization and radioactive waste analysis[3].

In this article, we will first outline the basic working principle of LIBS, including plasma generation and spectral emission processes. We will then present an overview of the different LIBS systems developed at RRCAT and the analytical approaches used for elemental analysis, highlighting their capabilities and application areas.

2. Basics of LIBS

When a high energy laser pulse is focused onto a material surface, the initial interaction begins with absorption of laser energy by free electrons present in the material. In this process, free electrons absorb photons from the laser field while undergoing collisions with ions or neutral atoms via a process known as Inverse Bremsstrahlung (IB). These energetic electrons then transfer their energy to the lattice, resulting in rapid lattice heating within the irradiated region. As the lattice temperature increases, the material begins to undergo phase transitions, first reaching the melting point, and forming a thin molten layer at the surface. When the rate of energy deposition exceeds the rate with which energy can be dissipated through thermal conduction and evaporation, deeper layers of the material may also melt. Under sufficiently rapid heating, the temperature of the superheated liquid can approach the critical temperature, resulting in phase explosion. In this process, the molten material undergoes an explosive transition into a mixture of vapour and fine droplets, ejecting atoms, ions, clusters, and free electrons that form a plasma plume. Since the plasma consists of atoms and ions ejected from the sample, therefore, it carries information about the sample's elemental composition.

Such conditions of rapid energy deposition, are typically achieved with nanosecond or shorter (picosecond/ femtosecond) laser pulses. Among these, nanosecond lasers are most commonly preferred in LIBS due to their simpler design, lower cost, and ability to generate sufficient plasma emission for reliable detection compared to picosecond and femtosecond laser systems. For longer pulse durations (e.g., microsecond), the rate of heat deposition is lower and can be balanced by thermal diffusion and evaporation. In this case, material removal occurs primarily through thermal evaporation, which may result in elemental fractionation due to differential vaporization of elements and thus reducing the possibility of producing a stoichiometric plasma plume. As a result, accurate composition analysis becomes difficult.

The mechanisms of laser energy absorption and subsequent plasma formation vary significantly depending on the type of material. In metals, there is already a sea of free electrons present to absorb the laser radiation. However, in case of semi-conductors, the laser energy is initially absorbed by conduction electrons which then undergo impact ionization, leading to avalanche multiplication and formation of large free electrons. In insulators, the initial seed electron may be provided by some impurities or field enhancement at defects or multi-photon ionization. Eventually, all materials start behaving optically like metals leading to plasma formation. However, the laser breakdown threshold differs for metals, semiconductors, and insulators, mainly due to differences in initial carrier density and band structure.

The laser induced plasma is initially very hot and dense, with temperatures of the order of ~10,000 K and electron densities around ~10^{17} cm^{-3}. At this early stage, the emission is dominated by continuum radiation arising mainly from free-free (Bremsstrahlung) and free-bound (radiative recombination) transitions. Free-free transition occurs when energetic electrons are decelerated in the Coulomb field of ions, while free-bound emission results from recombination of free electrons with ions. These processes produce a strong broadband emission known as continuum emission, which does not consist of any element specific information and hence is of no use from elemental analysis point of view. Once the laser pulse has ended, the plasma expands rapidly and generates a shock wave. As plasma expands and cools, its temperature and electron density decreases, causing excited atoms and ions to relax to lower energy states and emit characteristic spectral lines. This line emission is used for elemental analysis in LIBS. The entire process of nanosecond laser material interaction and plasma emission is shown schematically in Figure T.2.1.

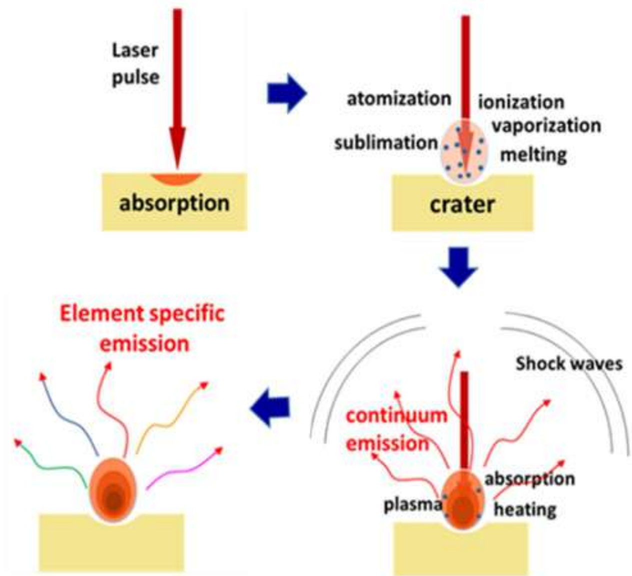

Fig. T.2.1: A schematic showing absorption of a nanosecond laser pulse in a material, leading to plasma formation, and continuum light emission followed by characteristic or element specific light emission.

The initial plasma emission is dominated by strong continuum radiation that can obscure characteristic spectral lines, and therefore, is not desired. To overcome this, time-gated detection is used, where the detector is triggered after a short delay of a few μs, allowing for the continuum to decay and the characteristic spectral lines to become prominent. A schematic of the time evolution of plasma emission is shown in Figure T.2.2.

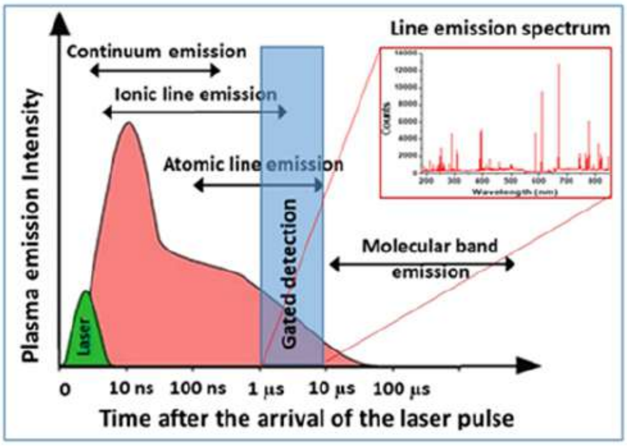

Fig. T.2.2: A schematic showing time evolution of plasma emission produced by a nanosecond pulse. Inset shows the LIBS spectrum of a soil sample recorded 1 μs after the laser pulse, where the nearly flat background indicates that continuum emission has largely decayed.

At further later stages of plasma evolution, i.e., several 10's of microsecond, the plasma temperature becomes even lower and recombination processes occur, where molecular species may form through recombination of ablated atoms or interaction with the surrounding atmosphere. This can lead to the appearance of molecular band emissions, e.g., CN, C_2, AlO, CaO, which appear as band structures and can provide additional information about the sample.

Although LIBS offers many advantages, several issues make the interpretation of its spectral data quite complex. One major issue is strong matrix effects, where variations in the composition and physical properties of the sample influence the laser matter interaction and consequently, the plasma temperature and emission. As a result, even for the same concentration of an element, the emitted intensity can vary from one matrix to another. This leads to poor transferability of calibration models across different sample types. The second important issue is self-absorption, a phenomenon in which photons emitted by the excited atoms or ions within the plasma are reabsorbed by the same species in lower energy states. This occurs when the radiation emitted by the hotter inner regions of the plasma gets reabsorbed by the outer colder layers, which contains a higher population of ground-state or low energy atoms or ions. This effect is more pronounced for strong resonance lines of major elements. As a result, the emitted line intensity does not increase proportionally with concentration, leading to reduced line intensity, distorted peak shapes, and deviation from linear calibration behaviour. Further, different spectral lines of the same species undergo different degree of self-absorption making the analysis further challenging. Another important factor which affects the LIBS signal is shot-to-shot fluctuation, where the spectral signal varies significantly between successive laser pulses. This variation arises from small changes in laser energy, beam profile, and sample surface conditions, which affect plasma formation and hence the emission intensity. In addition, spectral interference and overlapping emission lines make it difficult to identify and quantify elements in complex samples. All these factors collectively make the spectral interpretation challenging and necessitates the use of advanced data analysis techniques.

3. Analysis techniques

The analysis of LIBS spectra can be broadly categorized into qualitative and quantitative analysis. In qualitative analysis, the primary objective is to identify the elements present in the sample. This is achieved by matching the observed spectral lines with known atomic or ionic emission lines available in standard spectral databases such as those provided by National Institute of Standards and Technology (NIST) [4]. Each element emits radiation at characteristic wavelengths corresponding to electronic transitions between energy levels. By comparing the measured wavelengths with reference values, the presence of specific elements in the sample can be confirmed.

Quantitative analysis is commonly performed using calibration-based methods, where the intensity of selected emission lines is correlated with known concentrations of reference standards to generate calibration curves. However, the univariate calibration, which is based on analysis of single spectral line, is often limited by factors known to complicate the LIBS analysis, i.e., matrix effects, self-absorption, plasma fluctuations, and spectral line overlap, etc. These factors can alter line intensities and lead to a non-linear relationship between spectral intensity and elemental concentration, making it difficult to perform reliable analysis on the basis of individual spectral lines. To overcome these challenges, multivariate approaches, including machine learning (ML) techniques such as principal component analysis (PCA), random forest (RF), support vector machines (SVM), and artificial neural networks (ANN), are increasingly being employed. Unlike univariate methods, which rely on an individual spectral line, ML approaches utilize information from a large number of spectral lines or entire spectrum simultaneously, allowing them to capture subtle correlations and complex patterns within the data. Methods such as PCA reduce data dimensionality by transforming the original high-dimensional spectral data into a smaller set of principal components that capture most of the variance in the dataset. PCA not only helps in noise reduction and feature extraction but also allows to visualize underlying patterns, trends, and clustering of samples leading to better understanding of similarities or differences within the dataset. ML models such as RF, SVM, and ANN can model complex, non-linear relationships among multiple spectral features and can be applied to LIBS data for classification or quantitative analysis. RF works by building an ensemble of decision trees, each of which learns a series of rules from the training data to make predictions. Randomness is introduced during tree construction to ensure diversity, improve accuracy, and reduce overfitting. SVM works by finding the best hyperplane to separate classes in the data, maximizing the margin between them. It can use kernel functions to handle non-linear separation, making it effective for classifying samples with overlapping or subtle spectral differences. ANN emulate the structure and function of the human brain, consisting of interconnected layers of artificial neurons. Each neuron receives inputs, applies weights and a bias, and passes the result through an activation function to produce an output. By adjusting these weights during training, the network learns complex patterns and relationships in the data, enabling it to make accurate predictions or classifications. Thus, ML techniques can handle the complex LIBS data and provide fast and reliable elemental analysis.

4. LIBS configurations: A general overview

LIBS offers high versatility in configuration, allowing systems to be customized according to specific sample requirements and operational environments. For example, laboratory-based LIBS systems are typically designed for high sensitivity and spectral resolution, often incorporating high energy nanosecond Nd:YAG lasers, free-space beam delivery optics, and high-resolution spectrometers coupled with intensified detectors such as intensified charge coupled devices (ICCDs) for time-resolved measurements. LIBS setups based on picosecond or femtosecond lasers produces reduced thermal effects and improved spatial resolution[5]. Industrial and field-deployable LIBS systems require compactness and robustness, and therefore prefer compact laser systems, fiber-optic beam delivery and compact spectrometers [6]. Other more advanced LIBS systems include, double-pulse lasers for enhancing plasma characteristics and improving analytical performance [7], imaging and micro-LIBS for spatial mapping [8].

5. LIBS setups developed at RRCAT and their analytical performance

5.1 Benchtop LIBS setup: A benchtop LIBS setup (Fig. T.2.3) was developed using a flash lamp pumped 1064 nm Nd:YAG laser, with energy up to 150 mJ, pulse duration of ~ 6 ns and repetition rate of 10 Hz for plasma generation. The laser energy at the sample was controlled via a combination of a half wave plate and polarizer. The laser beam was focused over the sample surface using a 100 mm focal length lens. The samples were placed over a manual XYZ stage. The plasma emission was collected using a 10 mm focal length lens and coupled into a fibre. The other end of the fibre was coupled to a five-channel spectrometer. The spectrometer has a spectral range of 200–815 nm and resolution varying from 0.1 nm at lower wavelengths to 0.18 nm at longer wavelengths. The spectrometer software was used to trigger the laser pulse firing as well as to adjust the delay time after laser pulse to start spectrum acquisition. The delay time was set at 1 μs, as by this time most of the continuum background was found to get extinguished and the LIBS line spectra could be recorded with a good signal to noise ratio.

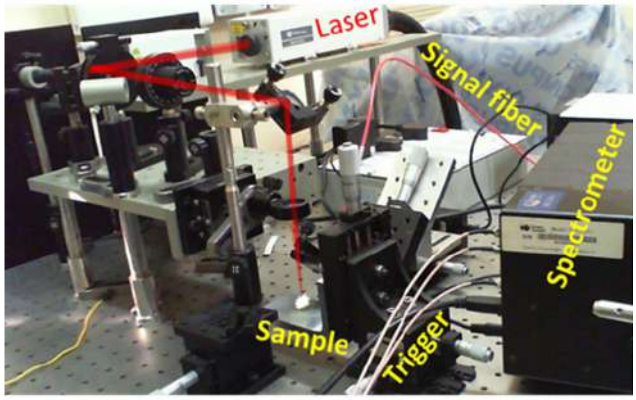

Fig. T.2.3: A view of the benchtop LIBS experimental setup.

5.1.1. Quantitative analysis of water-based samples: This setup was used to perform analysis of heavy element in water samples– [9]. One of the easiest methods to analyse liquid sample using LIBS is to solidify over some solid substrate. However, the main issue with this approach is the non-uniform deposition of solute particles over the substrate, due to the well-known coffee ring effect [10], which affects the repeatability of the LIBS spectra collected from different area of the solidified sample. To overcome such problem, we developed a laser textured silicon substrate. For laser texturing, an in-house built DPSS laser at 532 nm having nanosecond pulse duration was used [11]. The laser texturing imparted superhydrophilicity to the silicon surfaces, which resulted in uniform spreading and solidification of the water-based samples over the textured area. Although metals like steel, aluminium, and copper also become superhydrophilic after laser texturing but silicon was chosen for its stable superhydrophilic nature. The laser textured superhydrophilic metals start transitioning towards hydrophobicity soon after laser texturing due to the high reactivity of the metal oxides, formed during laser texturing, with ambient gases. In contrast, silicon does not react with ambient gases and remained superhydrophilic for a few months, and hence can be stored for later use.

To evaluate the uniformity of sample deposition over the laser textured area, a two-dimensional (2-D) LIBS scan was performed over the textured area at a step size of 0.5 mm in both the directions. Figure T.2.4(a) shows a laser textured silicon sample after it has been scanned by the LIBS DPSS laser. Uniformity of the samples solidified upon evaporation of water was determined by using the shot-to-shot relative standard deviation (RSD) of the LIBS spectra recorded from the central region of the textured area. The RSD for the solidified water samples containing Cr, Cd and Sr was found to be in the range of ~ 6.4–7.8% (Fig. T.2.4(b)) and that for the blank laser textured silicon, i.e., without any sample, was found to be ~ 4.5%. These results suggested that the water-based samples got solidified with good uniformity within the central region of the superhydrophilic textured area.

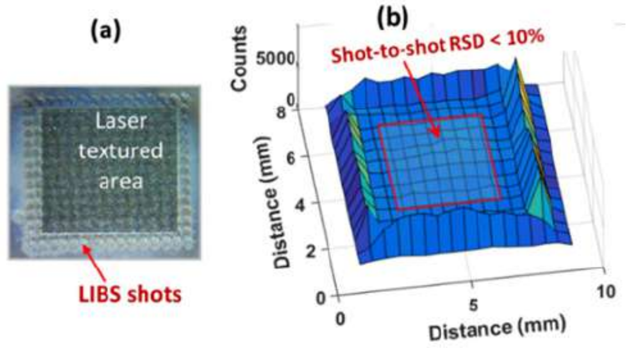

Fig. T.2.4: (a) A view of a laser textured silicon sample after it has been scanned by the LIBS laser and (b) 2-D LIBS scan for the Cr line at 425.44 nm over the laser textured area after 3 µL droplet of 10 ppm Cr solution was solidified.

The laser-textured area also helped in confining the liquid samples within the structured region due to its superhydrophilic properties. As a result of this confinement, even a small liquid volume of about 3 µL was sufficient to achieve ppm or sub-ppm level limits of detection (LOD), depending on the sensitivity of the selected LIBS spectral line. Furthermore, the LOD could be improved to ppb level by repeating the process of placing and drying small droplets over the textured area without significantly affecting the shot-to-shot RSD of LIBS spectral peaks for up to a few 100's of such repetitions. Table T.2.1 presents the LOD values obtained with different sample volumes for Cr, Sr and Cd.

Table T.2.1. Limit of detection (LOD) obtained for different elements with different volumes.

Element	Volume	LOD
Cr	3 µL	1.1 ppm
Cr	30 µL	0.41 ppm
Cr	100 µL	83.9 ppb
Cr	500 µL	14.9 ppb
Cd	3 µL	5.2 ppm
Cd	500 µL	16.8 ppb
Sr	3 µL	0.15 ppm
Sr	500 µL	13.4 ppb

5.1.2 Classification of steel samples

Steel grade identification is important in industrial quality control as well as efficient sorting of scrap during recycling processes. Considering the capability of LIBS for rapid, in-situ, and multi-element analysis with minimal sample preparation, we explored its use for steel grade identification [12]. Figure T.2.5 shows LIBS spectrum of a steel grade AISI 316. It can be noted that the spectrum is highly crowded due to the presence of multiple alloying elements, with major elements such as Fe, Cr, and Ni producing a large number of closely spaced spectral lines. This high line density leads to significant spectral overlap and interference, making it difficult to resolve individual element contributions. The challenge becomes even more pronounced when trying to distinguish between steel grades, which differ mainly in the concentrations of minor alloying elements. These subtle differences get masked by the dominant lines of major elements and by variations in plasma conditions, surface inhomogeneities, and shot-to-shot fluctuations. Therefore, ML techniques were employed for steel grade classification.

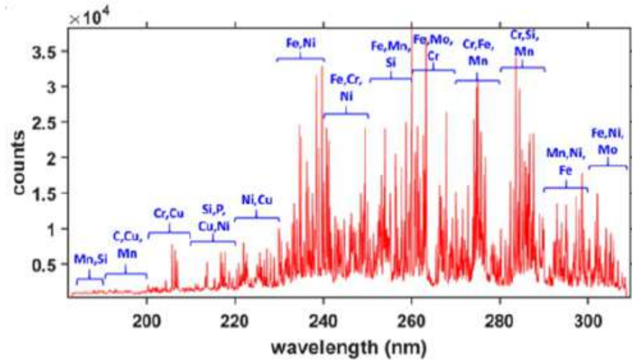

Fig. T.2.5: LIBS spectrum of steel grade 316 sample in the range of 185 nm to 310 nm.

When applying machine learning (ML) to LIBS data, proper pre-processing is essential. An important pre-processing step is feature scaling, e.g., min–max or standard scaling, which is done to bring all the spectral features to a comparable scale and avoid bias from highly intense peaks. In min-max (MM) scaler, each spectral feature x is normalized within a fixed scale using the formula $(x\text{-}x_{min})/(x_{max}\text{ -}x_{min})$; and in standard scaler (SS), features are scaled using $(x\text{-}x_{\text{mean}})/x_{\text{std}}$. Here, x_{min}, $x_{max,}$ x_{mean} and x_{std} are maximum, minimum, mean and standard deviation value of a feature x determined over all the spectra. In spectroscopy, another type of normalization is commonly practiced and this is called spectrum normalization (commonly area normalization). This is done to bring all the spectra to a common scale and thus compensating for the overall changes in spectral intensity among different spectra. For area normalization (AN), each spectrum is divided by total area under the spectrum. We combined both the normalization techniques and found that classification accuracy of ML techniques improved considerably. For this study, a total of 11 steel samples belonging to seven grades: 304, 304L, 316, 316L, 410, 4140 and 440, were used. Figure T.2.6 shows the results of SVM based classification of the samples into their respective grades. The grade prediction accuracy was highest when area normalization was followed by min-max feature scaling. The improved accuracy can be attributed to the complementary nature of the two normalization steps. In a data set consisting of multiple spectra arranged in different rows: area normalization operates row-wise reducing the effect of shot-to-shot fluctuations, while feature scaling operates column-wise, ensuring uniform contribution of all spectral features across multiple spectra. The grade identification accuracy with area normalization followed by min-max scaler was found to be 98.9%. It may be noted here that some of the grades to be identified were quite similar, e.g., 304 and 304L, which mainly differ in the concentration of carbon, which is present in quantity less than 0.08%. The high classification accuracy suggested that LIBS can be used for reliable grade classification of steel samples.

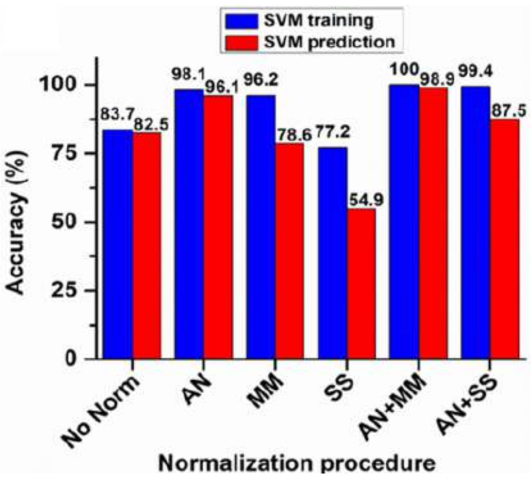

Fig. T.2.6: Classification accuracy of different steel grades during training of SVM models as well as for prediction made using the trained SVM models, when different normalization procedures were applied. AN: area normalization, MM: min-max scaler, SS: standard scaler.

5.2 Trolley mounted stand-off LIBS setup

In many practical scenarios, samples may be located in hazardous environments or at inaccessible locations, where direct contact or close-range analysis is not feasible. For such applications, stand-off LIBS provides an effective solution by enabling analysis of materials from a distance without the need for sample handling. We have developed a stand-off LIBS setup using a nanosecond pulse laser of 350 mJ pulse energy [13]. To focus the laser beam tightly up to several meter distances, it was first expanded by 4X using a combination of a plano-concave lens of −25 mm focal length and a plano-convex lens of 100 mm focal length. Laser focusing distance was changed by adjusting distance between the two lenses. For efficient collection of signal from such long distances, a 4″ Maksutov–Cassegrain telescope was used. The collected signal was coupled to a multi-channel Czerny Turner spectrometer via an optical fiber. The entire setup was mounted on a wheeled trolley and is capable of analysing the samples from a distance of ~10 m (Fig. T.2.7). Using the setup, investigation was performed on detection of Sr, which may be present as a radioactive contamination in nuclear reactors on stainless steel. For the study, residual dried spots left behind by 1 μL droplets of Sr solution were analyzed using LIBS from a distance of 6 m. Figure T.2.8(a) indicates the spectral features of Sr in the crowded steel spectrum, while Figure T.2.8(b) indicates the location of the LIBS shot fired over the dried Sr solution droplet. A calibration curve was prepared for intensity of Sr peaks at different concentrations of Sr (Fig. T.2.8(c)). From this calibration curve, the limit of detection of Sr was estimated to be ~ 30 ppb, which is equivalent to ~ 1.5 ng/cm^2.

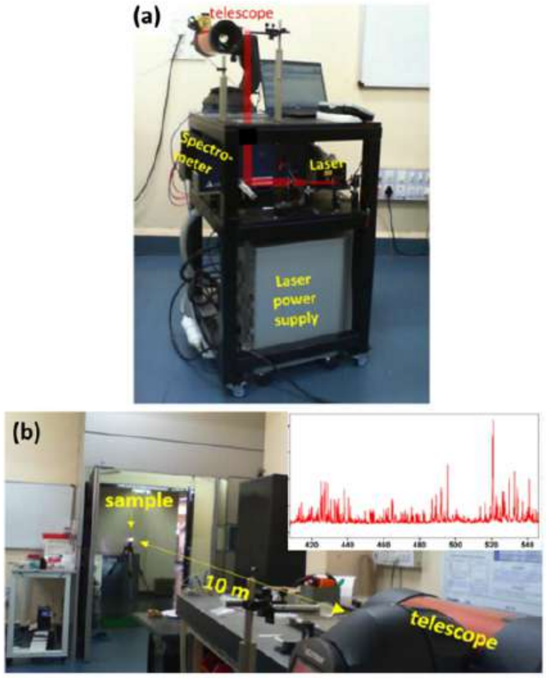

Fig . T.2.7 (a): A view of the trolley mounted stand-off LIBS setup and (b) a photograph showing working of the stand-off LIBS setup for steel sample located at a distance of 10 m away. Inset shows the spectrum recorded from the sample.

5.3. LIBS setup based on low energy high repetition rate DPSS laser

Both benchtop LIBS and stand-off LIBS setups were developed using a flash lamp pumped Nd:YAG laser with pulse energy in range of 150 mJ -350 mJ. This pulse energy is high enough to cause breakdown of the material and form a strong plasma signal using a single pulse. We observed that a weak plasma could also be formed by focusing in-house built DPSS Nd:YAG laser system with pulse energy of up to 2 mJ and repetition rates up to 80 kHz, on metallic samples.

Therefore, we explored the use of this laser system for LIBS— [14]. This system offers advantages such as requirements of reduced thermal management and longer operational lifetime. Further, due to the low pulse energy, the generated plasma and associated continuum emission was negligible, which allowed trigger-free spectral acquisition. This is an additional advantage as there is now no need for synchronization of spectrometer with laser. The plasma signal is also weak due to the low pulse energy, but by accumulating

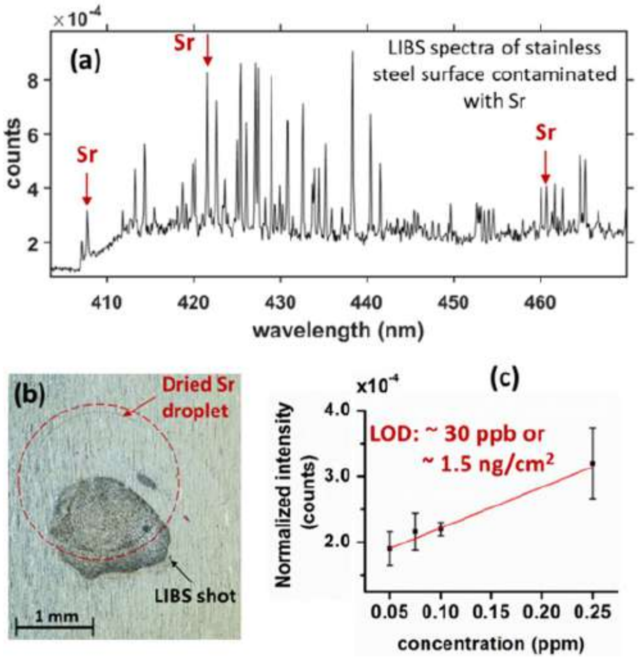

Fig. T.2.8: (a) LIBS spectra recorded from a distance of 6 m from the spot left behind by evaporation of Sr solution droplet on steel substrate, (b) image of the dried Sr droplet (dotted circle) along with the LIBS shot mark and (c) calibration curve prepared using Sr peak at ~ 421.5 nm.

signal over a large number of pulses, a good signal-to-noise ratio can be recorded. While this approach relaxes the need of synchronization, the high repetition rate of the laser introduces a new requirement of sample scanning. Due to kHz repetition rate of the laser, the laser pulses form a deep crater on the sample if allowed to hit at the same sample site during spectral acquisition. These deep craters disturb the laser focusing and hence weaken the laser matter interaction and the plasma intensity. Therefore, in this setup, the sample was mounted on a motorized XY stage and continuously moved during analysis to ensure deep craters are not formed. Figure T.2.9 shows a view of the experimental setup using the DPSS laser. By optimizing the experimental parameters like pulse energy, laser repetition rate and sample scanning velocity, LIBS spectra could be recorded with inter-spectrum variability similar to that obtained for conventional high pulse energy LIBS.

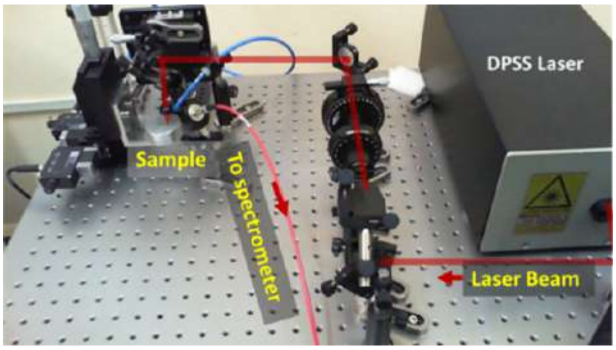

Fig. T.2.9: A view of the LIBS setup developed using the in-house built DPSS laser with 2 mJ of maximum pulse energy and 80 kHz of maximum repetition rate.

Analytical performance of this set up was evaluated by performing quantitative estimation of steel alloying elements. For the quantitative analysis, 19 steel samples were analyzed and ~1000 spectra were recorded from each sample. Figure T.2.10 shows LIBS spectra recorded from various steel grades, which look quite similar because of compositional similarity.

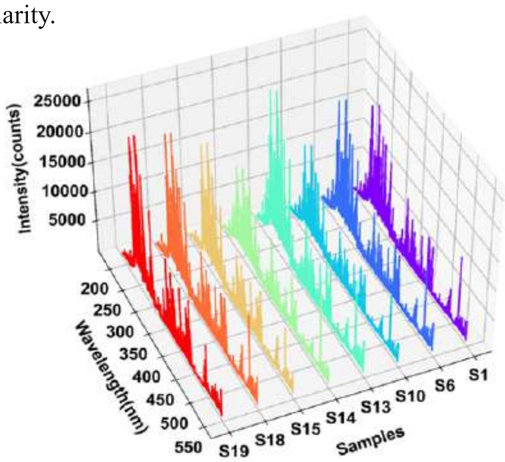

Fig. T.2.10: LIBS spectra of different steel samples recorded using DPSS laser-based LIBS setup.

The concentration of the various steel alloying elements was first determined using other methods like ICP-OES or Spark-OES and these values were used as reference standards for calibration. As an initial approach, a simple univariate (single spectral line) calibration method was employed by correlating the intensity of individual spectral peaks with increasing elemental concentration. However, the data points exhibited significant scatter, indicating poor correlation between the intensity and concentration. Therefore, the calibration curves derived from this method led to large prediction errors, with relative mean errors ranging from ~ 5% to 450% for different elements. The observed scattering of data points in univariate analysis is expected to be due to the factors such as self-absorption effect, matrix effect, etc., which make the LIBS spectra complex. Since single peak analysis did not perform satisfactorily, a machine learning approach based on the random forest algorithm was employed. During training, the model learns the optimal patterns in the data, which are then applied to new data for prediction. To improve robustness and reduce overfitting, randomness is introduced during tree construction, and the final prediction is obtained by aggregating the outputs of all trees. Figure T.2.11 shows the results of random forest regression for various steel elements, where 15 steel samples were used to train or calibrate the RF regression models. Thereafter, these RF models were used to predict the concentration of elements of 4 steel samples. The results of prediction are also presented in the figure. Table T.2.2 shows the tested range of elemental concentration, observed relative error (RME) between the actual concentration values and predicted concentration values. The benchmark range of RME obtained in LIBS for different range of elemental concentration are also listed in the Table, which suggests that the RME values are well within the benchmark range.

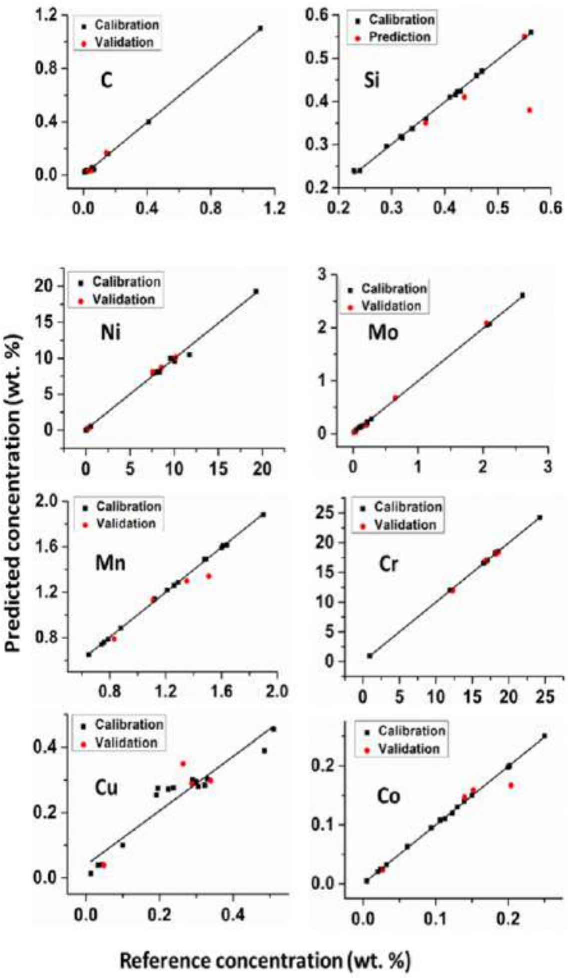

Fig. T.2.11: Random forest regression predicted values versus references values of concentrations of various elements for the calibration and validation of samples.

Table T.2.2. Relative mean error in predicted concentrations of various steel elements using random forest regression.

Element	Tested concentration range	Observed relative mean error (RME)	Benchmark RME range
Cr	12.32 – 18.38%	1.41 %	1-5 % (for element conc. >1%)
Ni	0.25-10.15%	2.08 %	
Mo	0.029-2.05%	5.45 %	
Mn	0.83-1.51%	5.40 %	
Si	0.36-0.56%	10.78 %	5-20% (for element conc. <1%)
C	0.026-0.14%	11.1 %	
Cu	0.05-0.34%	15.75 %	
Co	0.03-0.2%	9.71 %	

5.4 Fiber optics LIBS setup

As LIBS makes use of laser to obtain the spectra of plasma, therefore offers the possibility to deliver the laser beam through an optical fiber. Further, as the spectra is already being collected using an optical fiber, therefore, the configuration in which both laser delivery and signal collection is done using fibers is referred to as fiber-optic LIBS (FO-LIBS). A schematic of the developed FO-LIBS setup[15] is shown in Figure T.2.12(a). The advantage of this system is that it allows sensitive components of the LIBS setup such as the laser, spectrometer, and detector, to be positioned away from the sample, enabling remote analysis using a fiber-optic probe that incorporates both the laser delivery and signal collection using optical fibers. Figure T.2.12(b) shows a view of the developed FO-LIBS probe. Since FO-LIBS requires the delivery of energetic laser pulses through an optical fiber to generate plasma at the sample surface, a major challenge lies in transmitting these high-energy pulses without causing damage to the fiber itself. Therefore, to reduce the risk of damage, optical fibers of large core diameter of 1000 µm was used for beam delivery. However, such fiber delivery transformed the Gaussian-like input laser beam (Fig. T.2.12 (c)) into flat-top like beam (Fig. T.2.12(d)) due to excitation of multiple modes through the fiber. Figure T.2.12(e) shows the ablation spot formed on a steel sample using the fiber delivered beam.

Even when large core diameter of fiber is used, still to minimize the risk of laser-induced damage, it is preferable to use the lowest pulse energy that is sufficient to generate plasma on the sample surface. It was observed that a pulse energy of as low as 6 mJ (fluence ~1.86 J/cm^2) was sufficient to initiate plasma formation on the steel surface. However, the generated plasma could not be sustained over multiple shots as the emission intensity monotonically decreased when multiple pulses were fired at the same sample location and eventually vanished. This behaviour, as shown in Figure

T.2.13(a) was observed for energies up to 10 mJ (fluence ~3.11 J/cm²). Beyond this fluence, the plasma signal was found to be stable and could be sustained over hundreds of shots (Fig. T.2.13(b)).

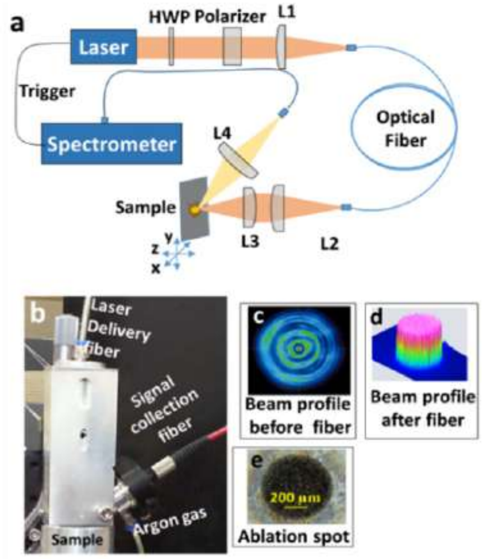

Fig. T.2.12: (a) A schematic of the Fiber-optics LIBS setup, (b) a view of the FO-LIBS probe, (c) laser beam profile before the fiber and (d) after the fiber, and (e) ablation spot formed on steel sample using the fiber delivered beam.

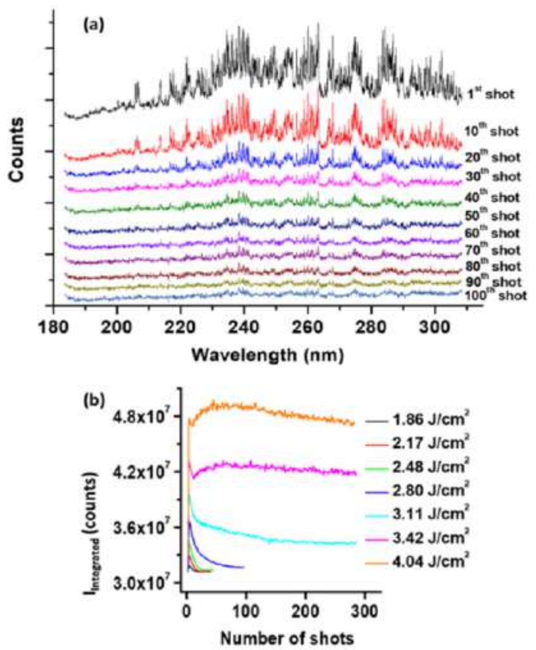

Fig.T.2.13: (a) The plasma spectral signal from a steel sample at a fluence of ~2.8 J/cm² at different laser shot numbers, (b) variation in plasma signal intensity integrated over entire spectra ($I_{Integrated}$) with increasing number of laser shots at various laser fluence.

Further investigations of surface morphology and chemistry indicated that at low fluence, the plasma mainly arises from ablation of the surface oxide layer, which has a lower ablation threshold than the base metal. As this layer is removed with successive shots, the plasma signal diminishes and eventually disappears. A stable and sustained plasma is achieved only when the fluence exceeds the threshold required to ablate the base metal. Unlike free-space LIBS, where a Gaussian beam ensures that some portion remains above the threshold even at low fluence, FO-LIBS produces a top-hat-like beam profile due to multimode fiber propagation. This results in uniform energy distribution, causing the entire spot to be either below or above the threshold, leading to the observed threshold-dependent behaviour.

Since the spectra became stable just above the threshold, quantification was performed at two fluence levels: 4.04 J/cm² (to ensure stable plasma across all samples) and 5.6 J/cm² (well above the threshold). A hybrid machine learning approach was used, with RF for feature selection followed by ANN regression for quantification, offering better accuracy than RF alone and faster performance than ANN alone. A comparison of different error metrics for both fluence values is given in Table T.2.3.

Results presented in Table T.2.3 suggested that there is slight decrease in performance, i.e., increase in the error values for most of the elements at the higher fluence level. This may be due to increase in plasma electron density and hence the associated complexities like self-absorption. Overall, these results suggested that using very high fluence does not prove to be beneficial for the quantitative analysis and using energy values just above the threshold fluence are sufficient to provide accurate quantitative analysis. These results are helpful to optimize the energy requirement of the laser used for FO- LIBS, which is important for development of FO-LIBS systems.

Table T.2.3. Performance metrics of RF-ANN models at two laser fluence values.

	4.04 J/cm²			5.6 J/cm²		
Element	RME (%)	RMSE (wt . %)	MAE (%)	RME (%)	RMSE (wt . %)	MAE (%)
Cr	1.05	0.199	16.95	1.16	0.213	16.97
Ni	5.61	0.286	22.3	8.10	0.192	13.22
Mo	10.18	0.059	4.4	16.58	0.069	4.49
Mn	3.03	0.041	3.43	3.31	0.044	3.71
C	11.89	0.009	0.68	14.07	0.01	0.81
Si	1.8	0.036	0.83	2.1	0.01	0.92
Cu	7.24	0.059	1.9	8.36	0.032	1.86
Co	7.58	0.015	1.12	8.87	0.02	1.38
P	3.32	0.002	0.11	3.6	0.0018	0.13

Abbreviations: RME: Relative mean error, RMSE: Root mean square error, MAE: Mean absolute error.

6. Future directions

Our future work will focus on making the LIBS systems more efficient, compact, and suitable for real world applications, with fully integrated designs that allow single-window operation of all components and data analysis. We are working to make the DPSS laser-based LIBS system compact and portable for field applications. In fiber-optic LIBS system, we are developing fiber-optics probes, which can analyze samples located several tens of meters away. This will allow their use in confined and harsh environments like hot cells, high-temperature areas, and difficult-to-access industrial locations, where remote and flexible analysis is needed. We also look forward to integrate other analysis techniques like Raman and fluorescence with LIBS to further enhance the scope of applications.

7. Summary

We have developed a range of LIBS systems, including bench-top setup, stand-off system for remote elemental analysis, setup based on low-energy DPSS laser, and fiber-optic LIBS setup. Each of these setup is designed to address specific application requirements. To effectively handle the complex and information-rich LIBS data, we have also developed advanced machine learning approaches that enable reliable qualitative analysis as well as accurate quantitative estimation of elemental composition of samples. Overall, the integration of LIBS hardware with machine leaning data analysis techniques has significantly enhanced the capability of LIBS as an analytical tool. These LIBS systems hold strong potential for applications in environmental monitoring, industrial process control, and remote analysis in hazardous or inaccessible environments.

Acknowledgment

Authors would like to acknowledge the support of Shri Amarjeet Singh and Shri Satish Sahu for providing DPSS laser and Shri Pravin Haedaoo and Shri Bhagwat Prasad for the development of LIBS setups.

References

[1] Brech, F.; Cross, L., Optical Microemission stimulated by a Ruby Maser, Appl. Spectrosc. 16 (1962).

[2] D.A. Cremers, L.J. Radziemski, Handbook of Laser-Induced Breakdown Spectroscopy, Wiley, 2006.

[3] M.Z. Martin, S. Allman, D.J. Brice, R.C. Martin, N.O. Andre, Exploring laser-induced breakdown spectroscopy for nuclear materials analysis and in-situ applications, Spectrochimica Acta Part B: Atomic Spectroscopy 74-75 (2012) 177-183.

[4] NIST LIBS database, (n.d.).

[5] V. Zorba, X. Mao, R.E. Russo, Femtosecond laser induced breakdown spectroscopy of Cu at the micron/sub-micron scale, Spectrochimica Acta Part B: Atomic Spectroscopy 113 (2015) 37-42.

[6] F.J. Fortes, J.J. Laserna, The development of fieldable laser-induced breakdown spectrometer: No limits on the horizon, Spectrochimica Acta Part B: Atomic Spectroscopy 65 (2010) 975-990.

[7] L. St-Onge, M. Sabsabi, P. Cielo, Analysis of solids using laser-induced plasma spectroscopy in double-pulse mode, Spectrochimica Acta Part B: Atomic Spectroscopy 53 (1998) 407-415.

[8] S. Živkovic, A. Botto, B. Campanella, M. Lezzerini, M. Momcilovic, S. Pagnotta, V. Palleschi, F. Poggialini, S. Legnaioli, Laser-Induced Breakdown Spectroscopy elemental mapping of the construction material from the Smederevo Fortress (Republic of Serbia), Spectrochimica Acta Part B: Atomic Spectroscopy 181 (2021) 106219.

[9] S. Ahlawat, P.K. Mukhopadhyay, R. Singh, S.K. Dixit, K.S. Bindra, Laser textured superhydrophilic silicon for uniform solidification and sensitive detection of water-based samples using laser induced breakdown spectroscopy, J. Anal. At. Spectrom. 38 (2023) 883-892.

[10] D. Mampallil, H.B. Eral, A review on suppression and utilization of the coffee-ring effect, Advances in Colloid and Interface Science 252 (2018) 38-54.

[11] S. Ahlawat, A. Singh, P.K. Mukhopadhyay, R. Singh, K.S. Bindra, Nanosecond laser induced glass particle deposition over steel mesh for long-term superhydrophilicity and gravity driven oil water separation, Materials Chemistry and Physics 263 (2021) 124343.

[12] S. Ahlawat, G. Saxena, P. K. Mukhopadhyay, A. Rajan, B. N. Upadhyaya, S. K. Dixit, Two-way normalization of LIBS data for improved machine learning based classification of steel samples, in: NLS-33, Indian Laser Association, Indore, 2025.

[13] S. Ahlawat, P. K. Mukhopadhyay, K.S. Bindra, Demonstration of a Stand-off Laser Induced Breakdown Spectroscopy setup, in: NLS-30, Indian Laser Association, Online, 2022.

[14] S. Ahlawat, A. Singh, S. Sahu, P.K. Mukhopadhyay, R. Arya, S.K. Dixit, Trigger-free LIBS using kHz and a few mJ laser in combination with random forest regression for the quantitative analysis of steel elements, J. Anal. At. Spectrom. 39 (2024) 1927-1937.

[15] S. Ahlawat, D. Garg, P. Tripathi, R.K. Sahu, S. Banik, P.S. Hedaoo, B. Prasad, R. Singh, P.K. Mukhopadhyay, B.N. Upadhyaya, Effect of laser fluence on signal sustainability and quantitative performance of fiber-optic LIBS for steel samples, Spectrochimica Acta Part B: Atomic Spectroscopy 235 (2026) 107362.

PUBLICATIONS (July 2025 – Dec. 2025)

A. Journal Articles

1. Agarwal A.*, Kumar A., Verma P.*, Singh M.N., Rajput P.*, Kumar S.*, Sharma R.K.*, Kamal C., Giri S.*
Amplification of self-sensitization at nanoscale in NIR-Upconverting $NaErF_4$ core-shell crystals: implications for energy applications
ACS Applied Nano Materials, 8, 20411 (2025)

2. Annadata H.V.*, Kamal C., Ghosh B.*
Combination of x-ray absorption spectroscopy and atomistic simulations reveals features of correlated disorder in quartz-like germanium oxide
Journal of Physical Chemistry C, 129, 12475–12485 (2025)

3. Arya R.*, Paulose R.*, Bijanu A.*, Agrawal V.*, Shil R.*, Mishra D.*, Banerjee K.*, Chatterjee S.*, Bhattacharyya S.*, Bhisikar A., Mondi P.*, Singh U.*, Pendam J.*, Salammal S.T.*
Inherent role of density on the gamma ray attenuation characteristics of red mud based shield
Radiation Physics and Chemistry, 234, 112757 (2025)

4. Bairagi M.*, Hinge V.K.*, Yadav N.*, Joshi S.K.*, Shrivastava B.D.*, Jha S.N., Bhattacharya D.*
XAFS study of mixed ligand ethylenediamine copper complexes having distorted octahedral coordination geometry
Indian Journal of Pure & Applied Physics, 63, 571-583 (2025)

5. Bhatt M.*, Gautam K.*, Sagdeo A., Sinha A.K.*
Exploration of pH-Driven morphology and defect evolution in Nickel Cobalt Carbonate Hydroxide nanomaterial for supercapacitor applications
Chemsuschem, 18, e202501348 (2025)

6. Bitra V.S.*, Verma S., Rao B.T.
HiT-IP Raman: An innovative high-throughput spectra acquisition system with interactive PCA combined machine learning for instant classification of various analytes and mixtures
Microchemical Journal, 219, 116054 (2025)

7. Bunkar R.P.*, Mulani S.R.*, Bimli S.*, Dohare A.*, Varshney M.*, Roy T.*, Jangir R., Thakare V.B.*, Devan R.S.*
Metal-organic framework-5 and graphene oxide (MOF-5@GO) composite for effective detoxification of highly hazardous sulfur mustard
Surfaces and Interfaces, 72, 107030 (2025)

8. Chaudhari S., Thakur A.*, Rajan A.
Anomaly detection for web attack prevention: analyzing web access logs for threat mitigation
Journal of the Indian Academy of Mathematics, 47, 427-439 (2025)

9. Dalal A., Krishna H., Khan K.M., Kumar N., Chourasia C., Sahu K., Satapathy S., Majumder S.K.
Detection of urea adulteration in packaged milk samples using spatially-offset Raman spectroscopy
International Dairy Journal, 168, 106307 (2025)

10. Das M.P.*, Dhar V.K.*, Singh A., Bhatt N.*, Yadav K.K.*
Development of source-dependent gamma-ray image parameters using Generative Adversarial Network (GAN) for the MACE telescope and its implications
Journal of High Energy Astrophysics, 48, 100416 (2025)

11. Dave T., Lal S., Pant K.K.
A novel methodology to tune the π mode RF parameters of a SW linac with full cell termination
Journal of Instrumentation, 20, P08032 (2025)

12. Deo R.K., Jain M.K., Kanyal G., Badapanda M. K., Bohrey A., Upadhyay R., Tripathi A., Tyagi R.K., Ntiwari N., Bagduwal P.S., Arora R.K., Gupta A.K., Sharma D., Jain A., Kumar R.
Review of multi-beam Klystron based RF power system of Indus-2
Asian Journal of Physics, 34, 625-642 (2025)

13. Deshmukh P., Sharma B., Chakraborty S., Srivastava H., Sahu K., Satapathy S., Majumder S.K.
NIR-Excited imaging of cervical cancer cells using biocompatible LaF_3:$Er^{3+}Yb^{3+}$ upconversion nanophosphors
Luminescence, 40, e70269 (2025)

14. Dey T., Kumar N.*, Patil R.*, Pathak P.K.*, Bhattacharjee S.*, Yadav P., Bhaumik A.*, Salunkhe R.R.*, Dutta S.*
Elucidating the role of cobalt nanoparticles and Mn-phosphate in etched ZIF-67/phthalimide-NC and phthalimene oxide for supercapacitor and electrochemical oxygen evolution reaction applications
Sustainable Energy & Fuels, 9, 1173-1182, (2025)

15. Gautam A., Rao B.T., Verma S., Kumar, K.V.A.N.P.S., Yadav R.K., Rana L.B., Verma S., Kumar M.

A novel experimental setup for determination of CO content to characterize catalyst performance for application of sealed-off CO_2 laser
Review of Scientific Instruments, 96, 123013 (2025)

16. Gautam K.*, Bhatt M.*, Sagdeo A., Singh H.*, Sinha A.K.*
Charge transport dynamics and energy storage implications of nickel cobalt carbonate hydroxide interaction with the Aloe vera leaf matrix
Nanoscale Advances, 7, 6066-6083, (2025)

17. Gauttam V.K., Dikshit B.*, Kasliwal A., Sharma A.*
Simplified analysis and optimal design method for LLC resonant converter based focusing magnet DC power supply in high power LINAC applications
International Journal of Circuit Theory and Applications, 53, 6535-6553 (2025)

18. Gupta H.*, Modi M.H., Malik P.*, Bommali R.K.*, Srivastava P.*, Ghosh S.*
N rich a-SiN_x:H as a prospective material for EUV/soft x-ray mirror: A soft x-ray reflectivity analysis near Si $L_{2,3}$ absorption edge
Journal of Applied Physics, 138, 035302 (2025)

19. Gupta N., Bhatt H., Bose A., Gupta M.*, Singh S., Rai S.K., Gupta P.
Deciphering the role of Nb driven interface engineering on the magneto-structural properties of W/CoFeB heterostructures
Journal of Alloys and Compounds, 1035,181571 (2025)

20. Gupta P.K., Sharma R.K., Raghavendra S.
Design optimization study of cryogenic counter-flow plate fin heat exchangers
Cryogenics, 148,104063 (2025)

21. Jha H.S.K., Rai S.K., Ganguli T., Shukla R.
Finite element analysis of mechanical deformable mirror using near-Bessel point support
Journal of Optics, 27,125603 (2025)

22. Kane S.R., Whatmore R.W.*, Jha P.K.*, Mehta P.K.*
Optimizing pyroelectric x-ray detectors for synchrotron applications
AIP Advances, 15, 125309 (2025)

23. Karanje R.*, Bera A.*, Rudra S.*, Mukhopadhyay D.*, Banerjee S.*, Bansal M.*, Baraik K., Chowdhury S.*, Li W.B.*, Valvidares M.*, Maity T.*, Saha B.*
Orbital angular momentum-driven ferromagnetism with magnetic anisotropy and electronic structure of epitaxial neodymium nitride
ACS Nano, 19, 36636–36645 (2025)

24. Karmakar B.*, Aryshev A.*, Karmakar J.*, Aggarwal M.*, Sahu B.K.*, Mukhopadhyay P.K., Ghosh S.*, Kumar S.*
Burst mode amplification through Yb doped PCF ROD amplifier to generate mJ burst energy with femtosecond multi-micro bunch structure in all fiber laser system
Optics Communications, 596,132481 (2025)

25. Khandelwal A., Sharath Chandra L.S., Sagdeo A., Singh R., Gangrade M., Venkatesh R., Chattopadhyay M.K.
Eutectic microstructure and its effect on electrical and magnetic properties of V-Ti-Si alloy superconductors
Materials Science and Engineering B, 317, 118158 (2025)

26. Khanna A.*, Jain P.*, Paul C.P.
Towards biomimetic evolution of artificial intervertebral disc: a review
Medical & Biological Engineering &Computing, 63, 2853-2869 (2025)

27. Khanna A.*, Jain P.*, Paul C.P.
A finite element biomechanical investigation of lumbar spine segments through novel intervertebral disc design
Journal of Clinical Neuroscience, 139, 111425 (2025)

28. Krishna V.*, Sarguna R.M.*, Ganesan K.*, Ramaseshan R.*, Kamal C., Ganesamoorthy S.*
Structural, Dielectric, and Mechanical Properties of $ErFeO_3$ Single Crystal Grown Using Optical Floating Zone Method
Applied Physics A, 131, 995 (2025)

29. Kumar A.*, Ghosh T.*, Roy J.*, Aabdin Z.*, Sahoo S.K.*, Kandasami A.*, Tripathi S., Singh V.R.*
Luminescence shift in the nanocrystalline powder of Cu-doped ZnO revealed by synchrotron-based X-ray absorption techniques
Pramana, 99, 157 (2025)

30. Kumar, A., Sudheer A.E.*, Tejaswini, G.*, Vallinayagam M.*, Zschornak M.*, Murali D.*, Kamal C.
Electrically and mechanically tunable Rashba splitting in SbSeI Janus layer: a density functional theory study
Scientific Reports, 15, 45043 (2025)

31. Kumar L.*, Singh G.*, Bhatt R., Chowdhury D.R.*, Soharab M., Bhaumik I., Gautam C.*, Jewariya M*.
The effect of 1.5 mol % Zn substitution on the broadband THz optical parameters of stoichiometric $LiNbO_3$ single crystal
Journal of Molecular Structure, 1339, 142365 (2025)

32. Kumar R.*, Sisodiya D.S.*, Vijay K., Banik S., Sen S.*, Babu P.D.*, Bhattacharyya D.*
A combined theoretical and experimental investigation on an Fe-Doped Bi_2Se_3 topological insulator
Journal of Physical Chemistry C, 129, 19514-19526 (2025)

33. Kumar R.*, Sisodiya D.S.*, Vijay K., Banik S., Sen S.*, Babu P.D.*, Bhattacharyya D.*
Co doped Bi_2Se_3 topological insulator: a combined theoretical and experimental study
Materials Science in Semiconductor Processing, 195, 109572 (2025)

34. Kumar S.*, Rawat N.*, Parida S.C.*, Bhattacharya D.*, Jeyakumar S.*, Urkude R.*, Agrawal A.*, Ghosh B.*, Ganguli T., Haridas G.
Development of a facility for x-ray absorption fine-structure spectroscopy of radioactive samples at Indus-2 synchrotron radiation source India
Nuclear Instruments & Methods in Physics Research B, 568, 165857 (2025)

35. Le Sech C.*, Banerjee A.
The effect of space restriction on the bonding and vibrational properties of H_2^+ molecular ion
European Physical Journal D, 79, 119 (2025)

36. Mahapatra A., Ajimsha R.S., Vijay K., Kamparath R., Midday M., Banik S., Mukherjee C., Verma S., Misra P.
Tuning output of ZnO piezoelectric nanogenerators through V-doping and SiO_2 interlayer
Emergent Materials, 8, 8223-8232 (2025)

37. Maneesha P.*, Samantaray K.S.*, Saha R.*, Nabi T.*, Urkude R.*, Ghosh B.*, Pathak A.K.*, Bhaumik I., Mekki A.*, Harrabi K.*, Sen S.*
Room temperature multiferroicity and magnetoelectric coupling in Ca/Mn-modified BaTiO3
Journal of Materials Chemistry C, 13, 14552-14573 (2025)

38. Mohapatra L.*, Sonwane A.K.*, Samal S.*, Chauhan T.*, Garg P.*, Deshpande U.*, Tiwari M.K., Kushwaha A.K.*
Enhancing the photocatalytic water electrolysis performance of Zn_2SnO_4 nanostructures via post-synthesis nitrogen doping
Nanoscale, 17, 18852-1886 (2025)

39. Mollick F., Nayak M., Kashyap A.K., Kumar J., Majhi A.*, Pothana N., Rajput P.*, Tiwari M.K. Rai S.K., Singh M.N., Sagdeo A.
Structure, stress, and optical property correlations in nano-structured Mo/Si and W/B4C multilayer mirrors for hard x-ray applications
Journal Of Applied Physics, 138, 175303 (2025)

40. Muthukrishnan R.M.*, Sharma A., Kumar Y.N.*, Kader S.M.A.*
Structural and functional properties of $BiFeO_3/CuCrO_2$ nanocomposites for next-generation photosensors
Materials Science in Semiconductor Processing, 194, 109547 (2025)

41. Padole A.S.*, Singar V.*, Ratnawat P.*, Dabkara A.*, Kar D.P.*, Jain N.*, Gupta M.*, Sagdeo A., Sagdeo P.R.*
Structural and optical characterization of pure and lanthanum substituted $Nd_{1-x}La_xAlO_3$ prepared by Sol-Gel method
Chemistryopen, 14, e202400499 (2025)

42. Pal S., Kamparath R., Subrahmanyam V.V.V., Sharma N., Kumar Y.P., Tiwari S.K., Karwal S., Sankar P.R., Benerji N.S.
Sol-gel prepared TiO_2-PMMA composite thin film for high laser induced damage threshold optical coating
Optical Materials, 158, 116486 (2025)

43. Parashar R.*, Nailwal B.C.*, Goswami N.*, Lenka R.K.*, Singh J.*, Karki V*., Adak A.K.*, Parida S.C., Kar S., Mukhopadhyay S.*
Comparative study on corrosion behavior and performance evaluation of metal/alloy membranes for hydrogen recovery in bio-jet fuel production
Journal of Alloys and Compounds, 1041, 183874 (2025)

44. Parida T., Patajoshi S., Santra B., Qamar U., Bose A., Rao P.N., Rai S., Das S., Kanjilal A.
Exploring oxygen vacancies in sputtered HfO_2 films for multi-bit RRAM applications
Advanced Materials Technologies, 10, e00289 (2025)

45. Patajoshi S.*, Chattaraj A.*, Bose A., Qamar U.*, Das S.*, Luong M.A.*, Claverie A.*, Kumar V.*, Kanjila A.*
Experimental and theoretical exploration of oxygen impurities in sputter grown β-Ta films
Materialia, 42, 102430 (2025)

46. Patel A., Badapanda M.K., Reghu T., Kumar R., Khare P.
High-voltage pulse modulator for S-Band klystron in IR-FEL RF system
IEEE Transactions on Plasma Science, 53, 9 (2025)

47. Pathak M., Jain S.K., Ghodke D.V., Prasad V.
Pressure profiling of 2.45 GHz electron cyclotron resonance-based proton source for optimized performance
International Journal of Modern Physics A, 40, 30 (2025)

48. Pathak M., Naika R., Sharma N., Jain S.K., Ghodke D.V., Prasad V., Lad M.
Characterization of plasma produced at 2.45-GHz Frequency in CW mode by electron cyclotron resonance method using langmuir probe and optical emission spectroscopy
IEEE Transactions on Plasma Science, 53, 10 (2025)

49. Prakash R., Sharma A., Singh G.*, Kumar R.*, Kumar V.
Saturation of multipacting due to space-charge effects in elliptic SRF cavities
Physics of Plasmas, 32, 113904 (2025)

50. Priyadarsini M.*, Singh S.*, Kaushik S.*, Dev A.S.*, Roychowdhury R.*, Gupta P., Pandit P.*, Venkatesh R.*, Verma G.*, Vayalil S.K.*, Schwartzkopf M.*, Kumar D.*
Columnar nanostructure and morphology driven magnetic anisotropy crossover in obliquely deposited Co/Alq_3 metal-organic bilayers
Surfaces and Interfaces, 74, 107703 (2025)

51. Pussi K.*, Gupta P., Barbiellini B.*, Srihari V.*, Svec P.*, Bansil A.*, Gupta A.*, Kamali S.*
Local atomic structure of amorphous $Fe_{81-x}Co_xNb_7B_{12}$ alloys using synchrotron radiation x-ray diffraction and pair-distribution function analysis
Applied Physics Letters, 127, 012401 (2025)

52. Rathore R., Singhal H., Kulkarni R.*, Thamizhavel A.*, Bansal D.*, Chakera J.A.
Development of ultrashort intense broadband laser-plasma x-ray source for ultrafast Laue x-ray diffraction
Review of Scientific Instruments, 96, 074902 (2025)

53. Ravikanth K.V.*, Verma A.*, Singh J.B.*, Saini S.*, Rai S.K.
Tempering response of martensite and bainite in a Cr-Mo-V RPV steel: Influence of retained austenite and its thermal stability
Materials Today Communications, 49, 114246 (2025)

54. Roy R., Arora V., Mandal T., Mishra S., Moorti A., Chakera J.A.
Parametric variation of Cu Kα x-ray emission in intense ultra-short laser pulse solid interaction and correlation with fast electrons transport processes
Plasma Physics and Controlled Fusion, 67, 115005 (2025)

55. Rudra S.*, Rao D.*, Kobri M.S.*, Dey A.*, Karanje R.*, Das P.*, Manna S.*, Baral M., Yadav B.*, Pillai A.I.K.*, Garbrecht M.*, Gupta M.*, Sahoo S.*, Ganguli T., Saha B.*
Carbon ion implantation for electron compensation in epitaxial scandium nitride
Physical Review B, 112, 165302 (2025)

56. Sah D., Singh M.P.
Vacuum polarization current in presence of intense Sauter field
European Physical Journal Plus, 140, 1184 (2025)

57. Saini S.*, Srivastava A.P.*, Ghosh P.S.*, Sagdeo A., Ghosh A.*, Babu D.A.*, Madge S.V.*, Neogy S.*
Investigation of microstructural and magnetic property evolution in mechanically milled Co-Zr metallic ribbon
Journal of Materials Science, 60, 16480-16496 (2025)

58. Sarkar S., Singh V., Singh K.A.P., Chaudhary A., Tiwari V.B., Mishra S.R.
On Rabi oscillations in ground hyperfine states of 87Rb atom driven by a microwave field
Applied Physics B, 131, 8 (2025)

59. Sharma B.*, Hardeep*, Bisht K., Singh A., Singh R., Dalvi A.*
Solid-state supercapacitors with enhanced performance using Al^{3+}-Doped Li^+ Ion perovskite electrolyte integrated with carbon aerogel electrode
ACS Omega, 10, 39132–39147 (2025)

60. Shukla B.*, Maji D.*, Kumar N.R.S.*, Balakrishnan S.*, Upadhyay A.
Structural evolution and compressibility trends in Ce-doped UO_2
Journal of Nuclear Materials, 616, 156040 (2025)

61. Singh C.K.*, Rajalakshmi K.*, Balamurugan N.*, Kumar R., Gupta M.*, Ramaseshan R.*, Baraik K.*
Mitigating parasitic contributions in measured piezoresponse for accurate determination of piezoelectric coefficients in Sc-alloyed-AlN thin films using piezoresponse force microscopy
Journal of Applied Physics, 138, 075302 (2025)

62. Singh D.*, Singh R.*, Banerjee A.
A new variational wave-function ansatz for confined two-electron atomic systems
Journal of Physics B, 58,205002 (2025)

63. Singh S.*, Rath D.K.*, Kumar S.*, Ahlawat N.*, Sharma S., Singh A., Pandey S.C., Rout P.S.*, Bansal L.*, Sahu B.*, Srivastava S.*, Chondath S.K.*, Chattopadhyay M.K., Kumar R.*
Abrupt Raman line-shape evolution and quantifying short-range order parameter: laser-driven nanocrystallization in amorphous germanium
Journal of Physical Chemistry C, 129, 13329–13336 (2025)

64. Sudhir V.*, Das D.*, Utpalla P.*, Kolay S.*, Singh M.N., Dutta D.*
Amorphous solid water prevails inside the spherical nanopores of the MIL-101(Cr) framework below 200 K: PALS XRD and BDS studies
Physical Chemistry Chemical Physics, 27, 18222-18233 (2025)

65. Sun Y.L.*, Li Z.Z.*, Li Y.*, Zhou H.L.*, Pokhriyal A.*, Ghosh Haranath, Li S.L.*, Luo H.Q.*
Crystal growth and characterization of a hole-doped iron-based superconductor $Ba(Fe_{0.875}Ti_{0.125})_2As_2$
Chinese Physics B, 34,127401 (2025)

66. Verma A.K.*, Gupta R.*, Gupta, P., Rai, S., Prakash S.*, Tayal A.*, Gloskovskii A.*, Ramaseshan R.*, Garg P.*, Deshpande U.*, Gupta M.*
Effect of Al doping on structural, electronic, mechanical, and optical properties of VN thin films
Applied Surface Science Advances, 30, 100884 (2025)

67. Verma P.*, Swain A.*, Agarwal A.*, Mohanty S.*, Kumar S.*, Pandey P.*, Singh M.N., Giri S.*
Geometry-dependent nature of microstrain in single-phase NIR upconverting crystals
Crystal Growth & Design, 25, 9865 (2025)

68. Verma S., Bitra V.S.*, Rao B.T.
Machine learning driven trace detection of pesticide mixtures using citrate optimized Au nanoparticles based in-expensive efficient micro-drop SERS with portable spectrometer
Spectrochimica Acta Part A, 340, 126333 (2025)

69. Waghmaitar P.P.*, Alex S.B.*, Vazhayal L.*, Kad S.*, Urkude R.R., Ghosh B., Haram S.K.*
Rationally designed $PtNi/Ti_3C_2T_x$ bifunctional electrocatalysts with improved MOR and HER performance leveraged by alloying and SMSI effects
ACS Applied Energy Materials, 8, 14519–14529 (2025)

70. Wakale G.R.*, Choudhary E.*, Samtham M.*, Patil A.*, Yadav A.*, Yadav S.*, Sharma R.*, Ma Y-R.*, Jangir R., Jadhav H.*, Devan R.S.*
Morphology-driven interlinked 2D nanostructures anchored nickel cobalt sulfide ($NiCo_2S_4$) electrodes for high-performance symmetric supercapacitor
Journal of Energy Storage, 136, 118488 (2025)

71. Yadav J., Vanam S.P., Parate S.K.*, Doddi N.*, Srihari V.*, Pralong V.*, Fichtner M.*, Barpanda P.*
The effect of Ti-doping on the electrochemical activity of the $Li_{0.44}MnO_2$ cathode material for Li-ion batteries
Materials Advances, 6, 6508-6517 (2025)

B. Invited Talks

1. Banik S.
Role of topology, magnetism and electron correlation in kagome semimetal Co1-xFexSn
Physics of Strongly Correlated Electron Systems (5th PSCES-2025), Indian Institute of Technology-BHU, Varanasi, Sep. 12-14, 2025

2. Banik S.
Photoemission studies on spintronic materials using Indus-2 synchrotron.
A meeting on Advances in Condensed Matter Physics (ACMP-2025), UGC-DAE CSR, Indore, Dec. 26-28, 2025

3. Bose A.
SRF cavity processing
First Indian Particle Accelerator School (InPAS-2025), BARC, Mumbai, Sept.15-20, 2025

4. Chakera J. A.
Recent studies on proton acceleration and highly stable higher harmonic source generation and applications
12th DAE-BRNS Theme Meeting on Ultrafast Science (UFS-2025), IIT-Hyderabad, Nov. 13 –15, 2025

5. Jain V.
Cutting-edge technologies for high-performance superconducting particle accelerators
Special talk on the occasion of Engineer's Day, Indian Institute of Astrophysics, Bangalore, Sept 15, 2025

6. Jain V.
Mechanical design aspects: SC Linacs
First Indian Particle Accelerator School (InPAS-2025), BARC, Mumbai, Sept. 15-20, 2025

7. Jain V.
Indigenous development of superconducting Niobium cavities at RRCAT for particle accelerator
69th DAE Symposium on Nuclear Physics (SNP-2025), Dr B R Ambedkar National Institute of Technology Jalandhar, Punjab, Dec.8-12, 2025

8. Kumar V.
Envelope equations and particle dynamics
First Indian Particle Accelerator School (InPAS-2025), BARC, Mumbai, Sept. 15-20, 2025

9. Mondal P.
X-ray Lithography activities at the Synchrotron Radiation Source, Indus-2- A tool for micro-fabrication of 3-D structures
5th International Conference on Physics of Materials and Material based Device Fabrication (ICPM-MDF-2025), Shivaji University, Kolhapur, Dec. 10-12, 2025

10. Mukhopadhyay P. K.
Ultrafast Yb-doped fiber laser in diverse operating regime
International Conference on Atomic, Molecular, Nano & Optical Physics with Applications (IAMNOP-2025), Jawaharlal Nehru University (JNU), New Delhi, Dec. 17-19, 2025

11. Pal S.
Multifunctional thin films for optical coatings and optoelectronic device applications
International Symposium on Advanced Materials and Devices (SAMDeV 2025), IIT Kharagpur, Dec.19-20, 2025

12. Radheshyam P.
Electron guns
First Indian Particle Accelerator School (InPAS-2025), BARC, Mumbai, Sept. 15-20, 2025

13. Sandha R.
Mechanical design aspects: SC Linacs
First Indian Particle Accelerator School (InPAS-2025), BARC, Mumbai, Sept. 15-20, 2025

14. Upadhyaya B. N.
High-power solid-state lasers for material processing applications
International Conference on Atomic, Molecular, Nano & Optical Physics with Applications (IAMNOP-2025), Jawaharlal Nehru University (JNU), New Delhi, Dec. 17-19, 2025

C. Seminar/Conference Presentations

C.1. Other Seminar/Conference Presentations

1. Anuj, Tiwari H., Kumar R., Khamari S.K., Vashisht, G. Khakha A., Maheshwari P., Dixit V.K., Sharma T.K.
Micro-patterned electroplated Indium on GaAs for x-ray pixel detector integration
69th DAE Solid State Physics Symposium, Indian Institute of Technology, Roorkee, Uttarakhand, Dec. 19-23, 2025

2. Chakravarty U., Kumar A., Barnwal S., Jain S., Patidar R.K., Benerji N. S., Chakera J.A.
Bio-inspired route for enhanced x-ray emission from high-energy sub-ns Laser produced plasmas
National Symposium on Plasma Science and Technology (PLASMA-2025), IIT and IISER, Tirupati, Dec. 27-29, 2025

3. Khamari S. K., Vashisht G., Porwal S., Dixit V. K., Sharma T. K.
Photoluminescence intensity and polarization enhancement in a weakly coupled GaAs quantum well–microcavity system
36th AGM of MRSI & 7th Indian Materials Conclave and International Conference on Emerging Materials (MRSI-ICEM 2025), NISER Bhubaneswar, Odisha, Dec. 17-20, 2025

4. Khan R.A., Tayyab M., Moorti A., Chakera J. A.
Measurement of laser back reflection during High intensity laser solid interaction at oblique incidence
National Symposium on Plasma Science and Technology (PLASMA-2025), IIT and IISER, Tirupati, Dec. 27-29, 2025

5. Khan S., Khan S., Singh A., Sharma T.K.
Ultrafast dynamics of bound excitons in MoS_2 monolayer
12th DAE-BRNS Theme Meeting on Ultrafast Sciences (UFS-2025), 13-15 Nov., 2025, IIT Hyderabad.

6. Kumar A., Chakravarty U., Barnwal S., Singh A., Jain S., Mukherjee C., Patidar R.K., Singhal H., Benerji N.S., Chakera J.A.
Probing Laser-Driven Dynamic Compression and X-ray Emission in Pure and Layered Copper Targets
National Symposium on Plasma Science and Technology (PLASMA-2025), IIT and IISER, Tirupati, Dec. 27-29, 2025

7. Kumar A., Sudheer A.E.*, Tejaswini G.*, Vallinayagam M.*, Zschornak M.*, Murali D.*, Kamal C.
Tunable Rashba splitting in single layer janus SbSeI via strain and electric field
Topological Matter School: Topological excited states and non-crystalline systems (TMS2025), Donostia-San Sebastian, Spain, Aug. 18-22, 2025

8. Kumar M., Ansari A., Singhal H., Chakera J. A.
An intense, ultra stable, high-harmonic radiation from a semi-infinite gas cell with thermally-insulated end-cap
National Symposium on Plasma Science and Technology (PLASMA-2025), IIT and IISER, Tirupati, Dec. 27-29, 2025

9. Kumar R., Bhargava K., Choudhary M.R., Rawlani B.K.
Condition Assessment of Structures by NDT-A case study
2nd International Conference on Condition Assessment, Rehabilitation and Retrofitting of Structures (CARRS 2025), IIT- Roorkee, Dec. 11-13, 2025

10. Khan R.A., Tayyab M., Moorti A., Chakera J. A.
Measurement of laser back reflection during High intensity laser solid interaction at oblique incidence
National Symposium on Plasma Science and Technology (PLASMA-2025), IIT and IISER, Tirupati, Dec. 27-29, 2025

11. Maurya V.K., Chaudhari S., Tomar S.S., Rajan A.
NetFlow based multilayer fire wall effectiveness and validation framework
IEEE 2nd International Conference on Pioneering Developments in Computer Science & Digital Technologies (IC2SDT2025), National Institute of Technology, Delhi (NITD), Dec., 4-6,2025

12. Midday M., Ajimsha R.S., Sahu V.K., Payal, Verma S., Misra P.
Integration of memristive behaviour and NH_3 sensing in Pt/ZnO/ITO crossbar devices
XXIII International Workshop on the Physics of Semiconductor Devices (IWPSD-2025),
IIT Roorkee, Uttarakhand, Dec. 15-18, 2025

13. Sahu R.K., Sagdeo A., Singh R., Mishra S.*, Shahi P.*, Banik S.
Electronic structure and transport properties of Kagome semimetal Co1-xMnxSn.
69th DAE Solid State Physics Symposium 2025, Indian Institute of Technology, Roorkee, Dec. 19-23, 2025.

14. Sahu R.K., Mishra S.*, Shahi P.*, Sagdeo A., Kumar K.*, Chandra L.S.S., Banik S.
Effect of Mn doping in CoSn Kagome semimetal. ***National Conference on Electronic Structure (8th NCES-2025)***, Indian Institute of Science Education and Research, Bhopal, Nov. 20-22, 2025

15. Tiwari H., Anuj, Khamari S.K., Khakha A., Agrawal A., Kashyap Y.S., Khan S., Dixit V.K., Sharma T.K.
Development and characterization of fast-response hard x-ray detector based on SI-GaAs
69th DAE Solid State Physics Symposium, Indian Institute of Technology, Roorkee, Uttarakhand, Dec. 19-23, 2025

16. Verma D. K., Saxena G., Paraye A., Verma R.K., Tomar S.S., Rajan A.
A light weight deep learning model for real-time fire and smoke detection using CCTV footage. ***4th International Conference on Recent Trends in Advanced Sciences and Computing-2025 (ICRTASC-25)***, VIT Bhopal University, Bhopal, Nov.,17-19, 2025

17. Yadav U. Gandhi M.L., Kumari A.
Strategy to minimize low-frequency fluctuations in utility caused by cyclic load of ramping power supplies in booster synchrotron
2025 IEEE 4th International Conference on Smart Technologies for Power, Energy and Control (STPEC 2025), NIT Goa, Dec. 10-14, 2025

Note: '*' indicates author affiliation other than RRCAT, Indore

N.1: Handover of indigenous high-RRR Niobium sheets for accelerator development

In a significant step toward self-reliance in advanced accelerator technology, Dr. Ajit Kumar Mohanty, Chairman of the Atomic Energy Commission, handed over the first batch of indigenously developed high-Residual Resistivity Ratio (RRR) niobium sheets to Shri Unmesh D. Malshe, Director of RRCAT, on 22nd October 2025. This achievement stems from a collaborative effort between the Nuclear Fuel Complex (NFC), Hyderabad, and RRCAT to establish a domestic supply chain for high-purity niobium. These sheets, produced through rigorous melting, rolling, and annealing processes, are critical for manufacturing high-gradient superconducting cavities while ensuring minimal power loss. RRCAT performed RRR measurements at each stage of development.

Indigenously built first high-RRR niobium sheet handed over to Shri Unmesh D. Malshe, Director, RRCAT by Dr. Ajit Kumar Mohanty, Chairman, AEC & Secretary, DAE, at NFC, Hyderabad

These materials are critical to the development of Superconducting Radiofrequency (SCRF) niobium cavities, which achieve high efficiency by operating with negligible electrical resistance at 2 K. RRCAT employs specialized facilities for precision machining, forming, and electron beam welding (EBW) to fabricate diverse cavity structures, including single-spoke resonators and multi-cell elliptical cavities.

Reported by:
Vikas Jain (vikas@rrcat.gov.in)

N.2: DAE-Fermilab quality interaction meeting at RRCAT, Indore

A two-day DAE-Fermilab quality interaction meet was organized at RRCAT Indore during October 29-30, 2025 under the Indian Institution Fermilab Collaboration (IIFC). Objective of the meet was, to discuss the quality assurance/quality control (QA/QC) processes adopted by participating units of DAE with respect to the deliverables to the construction phase of PIP-II project of Fermilab, USA. Fermilab team comprising of Matthew Joseph Luedke, Quality Engineering Specialist II, Office of Performance Assurance and Hema Ramamoorthi, Director of International Engagements, Fermilab were present at RRCAT to conduct the meet. DAE QA team comprising of members from RRCAT, BARC and VECC attended the meeting offline at RRCAT. Sub-Project Managers and other system experts from Fermilab attended the meeting through video conferencing on Microsoft teams. Sub-Project Coordinators and other officials from DAE units working on the deliverables also attended the meeting online. Meeting was held from 18:30 to 20:30 hrs on both the days. During the day time Fermilab team visited various scientific laboratories/facilities of RRCAT involved in the activities related to deliverables under IIFC.

Participants attending the quality interaction meet

At the start of two-day meet, Shri Sanjay Chouksey, Overall Coordinator of DAE QA activity and Mr. Matthew Joseph Luedke from Fermilab gave a brief overview of the IIFC deliverables and explained the purpose of holding the interaction meeting. On the first day six presentations were made by QA team members from RRCAT/BARC/VECC. On the second day six presentation from DAE QA team members and one presentation by Fermilab expert were made. DAE team members gave presentations on topics such as QA/QC requirements of each deliverable item. It is to be noted here that composition of QA team is such that each participating units of DAE is checking QA requirements of deliverables executed by the other unit. Interactive discussions were made amongst the participants during the meet. The final talk was given by Mr. Matthew Joseph Luedke on the QA/QC Fermilab expectations, in which he covered the topics such as Non-conformance Handling, Document Handling, Quality Control Alignment Matrix, System Acceptance Review etc. Closing remarks were given by Shri Prashant Khare, Director, PAG and Matthew Joseph Luedke. They expressed satisfaction over the progress made regarding the Quality Assurance activities being under taken for IIFC activities. At the end of Quality meet, action items for DAE and Fermilab were summarized. Some of the major action items are as follows:

- Detailed Non-conformance process to be added to DAE QA plan
- Cavity shipping configuration to be clarified.
- Manufacturing inspection Plan for Amplifiers showing required tests at vendor to be finalized
- All Acceptance Check Lists to be completed and released by Fermilab

Reported by:
Shashikant Suhane (suhane@rrcat.gov.in)

N.3: Strengthening safety, health and environment practices at RRCAT

Ensuring a safe, healthy, and compliant workplace continues to be a core priority at RRCAT, given the presence of advanced accelerator, laser, and industrial facilities across the campus. Fire & Safety Section undertook several significant initiatives focused on statutory compliance, data-driven safety management, occupational health, inspections, training, and emergency preparedness.

Online Data-Driven Safety Management System: Fire & Safety Section adopted a structured, data-driven approach to strengthen Safety, Health & Environment (SHE) performance across RRCAT. Fire & Safety Section in coordination with Computer Division implemented an online Fire & Industrial Safety management system that integrates Yearly RRCAT safety review compliances, Quarterly status reports on Safety, Health & environment, Industrial hygiene surveillance reports, Fire call reports, Fire & Injury statistics reports, issuance of height passes etc. from various stakeholders. This digital initiative aims to enhance efficiency, accuracy, and accessibility of safety data, supporting the broader digital transformation of SHE management. Comprehensive data covering injury statistics, hazardous job activities (such as work at height, rotating and lifting machinery, high-voltage systems, and chemical handling), industrial hygiene monitoring, biological surveillance, work permit systems and emergency preparedness were compiled and analysed. Based on this analysis, the following key institutional reports were prepared on behalf of RRCAT & sent for compliance to AERB: (i) Quarterly Status Reports on Safety, Health & Environment (ii) Industrial Hygiene Surveillance Report (iii) Plant Accident Details Report (iv) Safety Management System (SMS) Report

Fire & Safety report management system

Internal Safety Inspections and Statutory Compliance: Members of Fire & Safety Section actively participated in Internal Safety Inspections. Inspections were conducted across various divisions to verify compliance with safe work practices and statutory provisions under AEFR-1996 and the Factories Act-1948. Workplace conditions including Fire safety, housekeeping, machine safety, electrical safety, emergency arrangements, noise levels, and illumination were assessed to ensure adherence to permissible standards. Observations and recommendations were communicated to concerned divisions for timely corrective actions. In addition, safety inspections were also carried out at the newly upcoming NEG coating facility at unoccupied area and at locations outside the RRCAT premises.

Occupational Health and Work-at-Height Safety: To mitigate risks associated with work at elevated locations, physical fitness tests for employees and contract workers were conducted prior to issuing "Height Passes." This ensured that only medically fit personnel were authorized for work at height. In coordination with the Certifying Surgeon, RRCAT, regular occupational health check-ups were conducted for employees, contract workers, and food handlers. These health surveillance activities enabled early identification of occupational health risks and strengthened preventive healthcare measures.

Training, Awareness, and Outreach: Fire & Safety Section actively contributed to a wide range of training and awareness programmes throughout the year. Industrial Safety lectures were delivered for employees and trainees, including a lecture at PC-94 jointly organized by ATI, Mumbai and RRCAT. A training programme for AERB officers was conducted at RRCAT during 25–28 November 2025 which focused on RRCAT's accelerator and high-power laser facilities and associated safety aspects.

Electrical Safety and Fire-Fighting Training: As part of National Electrical Safety Week-2025, RRCAT organized a one-day Electrical Safety Lecture Series. The programme was inaugurated by Shri Jishnu Dwivedi, Director, TDSG, who emphasized integrating safety into all professional activities. Expert speakers covered high-voltage safety, electrical hazards, control system safety, substation practices, pulsed power systems, and electrical fire prevention.

To strengthen fire safety awareness and hands-on preparedness, comprehensive fire-fighting training was imparted to 445 RRCAT and contract employees during 2025. The programme included lectures with audio-visual aids and practical training on fire extinguishers, breathing apparatus sets, hoses, and water branches at the Fire Station.

Fire-fighting training

Industrial Safety Management Programme: A One-Day Lecture Series on Industrial Safety Management was conducted on 8th October 2025. The programme was inaugurated by Shri Jishnu Dwivedi, Director, TDSG, who urged participants to adopt safety as a core professional responsibility. Expert sessions addressed crane and load-handling safety, disaster management, laser safety, construction hazards, machine safety, fire detection and alarm systems, and emergency first aid, supported by practical demonstrations.

Electrical safety lecture series at RRCAT

Professional Participation and Achievements: Shri Ajay Kumar, Dy. Chief Fire Officer, and Shri Shailendra Kumar Shukla, Scientific Assistant, participated in the 41st Safety and Occupational Health Professionals Meet (SOHPM) held at Ahmedabad from 17–19 December 2025 under the banner of IPR Gandhinagar and AERB. Shri Shailendra Kumar Shukla secured First Prize in English Slogan at the All-India DAE level, while Shri Ajay Kumar received consolation prizes in both English and Hindi Slogan competitions.

RRCAT officers at 41st SOHPM, Ahmedabad

Emergency Preparedness and Institutional Support: Members of Fire & Safety Section attended refresher training on National Radiation Emergency Preparedness as part of the Radiation Emergency Response Team to maintain readiness for radiological emergencies. Safety inspections were conducted for exhibits prior to public access during National Science Day - 2025. A week-long programme was organized during National Fire Service Week - 2025, including Martyr's Day observance, slogan, essay, and fire quiz competitions.

Joint Mock Drill and Accident Management: A joint mock drill under the On-Site Emergency Plan was conducted on 30th December 2025 at the Indus User Building, simulating an earthquake with mass casualties and fire. Multiple agencies including Indore Fire Service, Indore Police, BDS, CISF, RRCAT Fire and Medical Services participated. The exercise was successfully conducted under the command of the Incident Commander, with valuable feedback provided by the umpire.

Mock-drill for accident management

In the event of any accident, investigations were carried out as per the established SOP through a constituted committee. The Fire & Safety Section personally interacted with injured personnel and recommended remedial measures to prevent recurrence.

Reported by:
Prateek Bhatnagar (prateek@rrcat.gov.in)

N.4: Activities for clean and green campus

RRCAT under the aegis of Advisory Committee for Clean and Green Campus (ACCGC) strides for maintaining an eco-friendly culture in a lush green campus that covers all aspects of swachhata like waste segregation and management, energy conservation, rain water harvesting, paperless office procedures, plantation drives, cleanliness campaigns, and public awareness programmes.

During the monsoon session of 2025, a record 6,000 saplings of native plant species such as Arjuna, Neem, Maulsari, Pilkhan, Peepal, Bargad etc. were voluntarily planted by employees of the Centre including DAC members and the Director. With a survival rate of 90 %, they will develop into a self-sustaining Miyawaki forest within the next 2–3 years. These efforts have turned the campus into a model for biodiversity preservation as confirmed by google map that depicts the appearance of dense forest cover in 3 years.

A. Vriksharopan   B. Google map of miyawaki forest

The campus is already separating green and dry waste at source and the green-waste is processed at in-house 'Nisargun' plant to produce biogas, which is utilized to fuel the Guest House kitchen in part. Additionally, special drives were conducted in technical premises as well as colony area to collect e-waste separately and scrapping appropriately. Colour coded e-waste bins were introduced for the first time. Also, around 15 tons of e-waste, obsolete machinery, and scrap were collected from the RRCAT technical area by Stores.

Shri Viraj P. Bhanage, Director, Electron Accelerator Group, RRCAT and other senior officials during plantation drive

Swachhata in technical area

Metal turnings scrap for sale: Waste to wealth

Colour coded bins

Safai mitra felicitation on Swachh Bharat Diwas

Shramdaan at Surya mandir, Indore

Sanitary pad distribution & lecture by resident doctor

As part of its social outreach, 3000 packets of sanitary pads were distributed to underprivileged school girls in four nearby government-aided schools. Lecture cum demonstration was imparted to the students by resident doctor on general and menstrual hygiene. This assumes importance in view of the recent Supreme Court judgement that declares access to menstrual hygiene products a fundamental right under Article 21, directing the Union and State governments to ensure free sanitary pads and functional, gender-segregated toilets in all schools. RRCAT is perhaps the only DAE unit engaged in sanitary-pad distribution to the needy for last two years.

आरआरकैट में स्वच्छता महोत्सव

साइकिल रैली से सफाई के साथ किया 'मेक इन इंडिया' का आह्वान

Press coverage for the cycle rally

To promote sustainable and clean transportation, a cycle rally was organized on 25 September 2025, which was also joined by the Hon'ble Mayor of Indore, Shri Pushyamitra Bhargava. The rally witnessed enthusiastic participation from 200 RRCAT employees, CISF personnel, and AECS students.

Successful completion of above reported activities was possible due to the enthusiastic support and cooperation received from Horticulture section, Civil Construction and Maintenance Section, Construction and Services Division, Administration, Security and CISF personnel. Swachhata is a continuous process and must be adopted as a daily habit. As Mahatma Gandhi aptly remarked:

''जहाँ स्वच्छता है, वहाँ स्वास्थ्य है;
जहाँ स्वास्थ्य है, वहाँ संतोष है;
जहाँ संतोष है, वहाँ भगवान हैं।''

Reported by:
Team Clean & Green Campus (greencampus@rrcat.gov.in)

N.5: Activities by Women's Welfare Committee, RRCAT

"UDYAM-2025" - Entrepreneurship Fair by Women: Women's Welfare Committee organized a women's entrepreneurship fair "Udyam-2025" for female family members of employees of RRCAT on 2nd August 2025. The purpose was to encourage women entrepreneurship and provide them a platform to showcase their skills. 80 women participants had put up 40 stalls that showcased products which included handicraft and decorative Items, handmade jewellery, painting, clothes & dress material, home furnishing, homemade food products etc.

The event was inaugurated by Dr. Alpana Rajan, Associate Director, Technology Development and Support Group & Head, Computer Division, RRCAT. Dr. Alpana Rajan addressed the participants and emphasized that inherent qualities and skills of women can make them successful entrepreneurs. She actively interacted with the participants and learned about their products and motivated them. The event was attended by employees and their families with great enthusiasm.

Inauguration by Chief Guest Dr. Alpana Rajan

Chief Guest visiting the stalls put-up by the women entrepreneurs in the Udyam-2025 fair

Reported by:
Gitika Khare (gitika@rrcat.gov.in)

N.6: Activities of RRCAT Staff Club

RRCAT Staff Club organizes welfare activities in the areas of sports, music, culture, yoga and health to provide a holistic development environment to its members and their families. In addition to regular on-going activities, several events have been organized in the period July to December 2025. This period remained action-packed and dynamic, with the club successfully conducting over fifteen sports tournaments and cultural events. The Club successfully organized annual badminton, carrom, chess, pickleball, ball-badminton, table-tennis and season ball cricket tournaments in which more than 700 members participated.

Glimpses of activities by RRCAT Staff club

During this period, RRCAT Staff Club also conducted the Dwarka group team selection trials for cultural and table tennis events for participation 40th DAE S & CC meet. More than 150 players from different units of DAE participated in the selection trials. One of our active members, Sh. K. K. Kumar, undertook an extraordinary K2K (Kashmir to Kanyakumari) cycling expedition under the Fit India Movement of the Ministry of Youth Affairs and Sports. The expedition was flagged off on 1st November and successfully concluded on 16th November at Kanyakumari, covering approximately 4250 km. Three children from RRCAT, namely Jiyansh Gautam, Gourav Mehar, and Karthik Badgoti, were selected for the U-12 baseball team of the Indore Zone, which secured the Runner-up position at the National Level Little League Championship held from 5th to 9th November 2025 at New Delhi.

Shri K. K. Kumar during the K2K cycling expedition (left), and Indore Zonal team as runners-up in the baseball event during the National Little League Championship (right)

The Club placed strong emphasis on health and wellness by regularly organizing wellness classes for both men and women. In addition, a marathon and a cyclothon were also conducted. These activities witnessed enthusiastic participation from more than 800 members and their dependents. During this period, a musical extravaganza "Voice Icon RRCAT- 2025" emerged as a standout highlight, displaying exceptional talent from within the community and receiving an overwhelming response.

Participants during cyclothon and marathon events

Winner of the Voice-Icon RRCAT-2025

The year reached its crescendo with the flagship celebration "Kya Masti Kya Dhoom," a vibrant and grand funfair organized by the RRCAT Staff Club on 31st December 2025 to welcome the New Year 2026. It turned out to be a resounding success and making it a memorable celebration of the New Year.

Funfair "Kya Masti Kya Dhoom," on the eve of new year 2026

Reported by
Gurvinderjit Singh (gjit@rrcat.gov.in)

N.7: Rashtriya Karmayogi Large Scale Jan Seva Program (Phase-II) at RRCAT

In alignment with Honorable Prime Minister Shri Narendra Modi's national vision of Viksit Bharat 2047, RRCAT successfully conducted the Rashtriya Karmayogi Large Scale Jan Seva Program (Phase-II). The primary objective of this mass training initiative was to fundamentally transform the mindset and approach of central government employees toward public service. Organized under the directives of the Administrative Training Institute (ATI), Mumbai, and the Capacity Building Commission (CBC), New Delhi, the program successfully trained a total of 1,363 employees in batches across various hierarchies (Group A to Group C). The implementation of the program was executed seamlessly under a structured leadership framework to ensure high-quality delivery across all training batches. The training was executed in a multi-stage cascading model, ensuring that core training concepts were scaled effectively from expert trainers down to the entire workforce.

During the initial stage of the program, two Lead Trainers from RRCAT attended a specialized, national level 5-day rigorous training at the Indian Institute of Corporate Affairs (IICA) in Gurugram. Conducted directly by the Capacity Building Commission (CBC), New Delhi, this foundational phase successfully equipped the Lead Trainers with the specific curriculum and pedagogical methodologies required to drive the subsequent large-scale institutional rollout.

Thereafter, the two Lead Trainers in coordination with Nodal Officer, RRCAT conducted a comprehensive 3-day training session and successfully trained 32 Master Trainers (Karmayogi Facilitators) equipped to lead subsequent employee training modules.

Two Lead Trainers, Nodal Officer, and 32 Master Trainers (Karmayogi Facilitators), who spearheaded the Rashtriya Karmayogi Large Scale Jan Seva Program at RRCAT to provide training to 1329 employees of RRCAT

To execute the 1-day training sessions for mass employee training, the 32 certified Master Trainers were divided into 16 distinct pairs, with each pair taking charge of running the sessions. Each Master Trainer team covered between 2 to 4 batches, maintaining an optimized average batch size of 33 employees to ensure interactive and effective learning. A total of 1,329 employees (up to Level 16) underwent the rigorous 1-day training session during August 20 – October 15, 2025 at RRCAT, Indore.

Batch of RRCAT officials who participated in the one-day mass training program under Rashtriya Karmayogi Large Scale Jan Seva Program

Another batch of RRCAT officials who participated in the one-day mass training program under Rashtriya Karmayogi Large Scale Jan Seva Program

The conclusion of the program marked a significant milestone for RRCAT and the Department of Atomic Energy in building a citizen-centric, future-ready workforce. By successfully training 1,363 personnel, the institute has established a solid foundation for citizen-first public service delivery, directly contributing to the governance goals required to realize a fully developed nation by 2047.

Reported by:
Vijaya M. Tomar (aposrw@rrcat.gov.in)

N.8: Observance of Vigilance Awareness Week-2025

In accordance with the directives received from CVC and DAE, the Vigilance Awareness Week-2025 was observed in this Centre during the period from 27.10.2025 to 02.11.2025 with the theme “Vigilance: Our Shared Responsibility”.

For spreading the awareness among the employees, family members of employees and general public, flex banners inscribing the theme “Vigilance: Our Shared Responsibility” were prepared and displayed at various places of RRCAT. Integrity Pledge was administered by 1321 nos. of officials of RRCAT on 27.10.2025 through online mode.

CVC mandated to conduct structured training programs for Masters Trainers as well as other executives and officials by the Master Trainers/training institutes/other resources on the subject matters viz. Investigation & Report, Framing of Chargesheet, Conducting CTE type Intensive Examinations under “Capacity Building Programs”. In line of the said instructions, a two days lectures programme on topics viz. Investigation & Report CCS (Conduct) Rules, CCS (CCA) Rules, etc.) and Framing of Chargesheet was organized by inviting experts from RRCAT namely Shri Kamlesh Kumar Rambadia, AO-III and Shri Raghvendra Sinha, APO (Vigilance) in which 32 nos. of participants attended the lecture programme.

Lecture programme during Vigilance Awareness Week

In addition to this, as mandated by CVC, various courses available on iGOT on topics/themes such as Ethics, Conduct Rules, Integrity, Attitudinal Change, Cyber Hygiene, Public Procurement were undertaken and completed by 308 nos. of officials of this Centre. Various competitions viz. Essay writing, Poster making, Slogan writing were conducted in which 26 nos. of officials participated. Winners of I[st], II[nd] and III[rd] places in each of the competitions were awarded by cash prizes through their bank accounts and those participants who could not secure the winning positions were awarded by the consolation prizes.

Reported by:
Vigilance Section (apov@rrcat.gov.in)

N.9: राराप्रप्रौके में राजभाषा गतिविधियाँ

जुलाई-दिसंबर, 2025 के दौरान राजभाषा कार्यान्वयन समिति की 02 बैठकें दिनांक 26.09.2025 एवं 29.12.2025 को आयोजित की गईं। जुलाई- सितम्बर, 2025 की तिमाही में दिनांक 23.07.2025 को पीएजी प्रभाग तथा कर्मचारी संपर्क एवं कल्याण अनुभाग और 24.07.2025 को अग्निशमन एवं संरक्षा अनुभाग का आंतरिक राजभाषा निरीक्षण किया गया। अक्टूबर-दिसंबर, 2025 तिमाही में दिनांक 10.12.2025 को लेसर प्लाज्मा प्रभाग, दिनांक 11.12.2025 को उच्च ऊर्जा लेसर एवं प्रकाशिकी प्रभाग तथा दिनांक 12.12.2025 को रेडियो आवृत्ति प्रणाली प्रभाग का आंतरिक राजभाषा निरीक्षण किया गया।

जुलाई-दिसंबर, 2025 के दौरान 01 नियमित हिंदी कार्यशाला का आयोजन दिनांक 06.11.2025 को तथा केंद्र के प्रभाग/अनुभाग/प्रयोगशाला प्रमुखों के लिए 'संसदीय राजभाषा निरीक्षण प्रश्नावली' पर दिनांक 05.08.2025 को 01 विशेष हिंदी कार्यशाला का आयोजन किया गया । इन कार्यशालाओं में कुल 84 पदाधिकारियों ने भाग लिया। दिनांक 22-23 अगस्त, 2025 को दो दिवसीय अखिल भारतीय हिंदी वैज्ञानिक संगोष्ठी का आयोजन किया गया, जिसका उद्घाटन समारोह के मुख्य अतिथि अंतर-विश्वविद्यालय त्वरक केंद्र (IUAC), नई दिल्ली के निदेशक प्रोफेसर (डॉ.) अविनाश चंद्र पाण्डेय द्वारा किया गया। इस संगोष्ठी में परमाणु ऊर्जा विभाग की विभिन्न इकाइयों से लगभग 16 व्याख्याताओं ने व्याख्यान दिये। इसमें लगभग 200 श्रोतागण उपस्थित थे। हिंदी पखवाड़ा-2025 के दौरान आठ (08) प्रतियोगिताओं यथा काव्य-पाठ प्रतियोगिता, निबंध लेखन प्रतियोगिता, टिप्पण एवं आलेखन प्रतियोगिता, आशुभाषण प्रतियोगिता, वाद-विवाद प्रतियोगिता, अनुवाद प्रतियोगिता, प्रश्नोत्तरी प्रतियोगिता तथा संगीत प्रतियोगिता (गायन एवं वादन) का आयोजन किया गया। परमाणु ऊर्जा राजभाषा कार्यान्वयन योजना (अटॉलिस) के अंतर्गत जुलाई-सितम्बर, 2025 तिमाही में 69 दावे प्राप्त हुए, जिनमें से 56 पुरस्कार दिए गए। केंद्रीय हिंदी प्रशिक्षण संस्थान, राजभाषा विभाग, गृह मंत्रालय, नई दिल्ली द्वारा संचलित प्रबोध, प्रवीण एवं प्राज्ञ पत्राचार पाठ्यक्रम के 36 वें सत्र (जुलाई, 2025 से मई, 2026 तक) में इस केंद्र के 10 अधिकारी/कर्मचारी अध्ययनरत हैं।

प्रस्तुति:
विमल कुमार शुक्ल (vimalks@rrcat.gov.in)

N.10: Awards and Honours

N.10.1: Homi Bhabha Science and Technology Maanpatra

1. Shri Alok Singh, SO/G, Switch Mode Power Converter Section, Electron Accelerator Group, RRCAT has been conferred with the "Homi Bhabha Science and Technology Maanpatra" for the year 2025 for his outstanding contributions in the field of "Power Electronics". The Maanpatra was presented on the occasion of Founder's day program held at BARC, Mumbai on 30th Oct 2025.

2. Shri Sachin Kumar Agrawal, SO/G, Laser Controls & Instrumentation Division, Laser Group, RRCAT has been conferred with the "Homi Bhabha Science and Technology Maanpatra" for the year 2025 for his outstanding contributions in "Machine Vision Based Inspection Systems for Nuclear Fuel Quality Assurance". The Maanpatra was presented on the occasion of Founder's day program held at BARC, Mumbai on 30th Oct 2025.

N.10.2: Best Paper/Poster Award

1. Shri Ujjwal Yadav, SO/D, Accelerator Ramping Power Converter Section, Electron Accelerator Group, RRCAT, received the Best Paper Award at the 2025 IEEE 4th International Conference on Smart Technologies for Power, Energy and Control (STPEC 2025) held at the National Institute of Technology, Goa, India, during 10-13 December 2025. The detail of the paper is as given below

Title: Strategy to Minimize Low-Frequency Fluctuations in Utility Caused by Cyclic Load of Ramping Power Supplies in Booster Synchrotron

Authors: Ujjwal Yadav, Manoj Leelachand Gandhi, Aradhana Kumari

N.11: New Recruits

RRCAT welcomes the following personnel who have joined during July 2025 to December 2025:

- Shri Arpit Goyal, SOC, IAD
- Shri Raj Gaurav, SOC, RFSD
- Shri Siddharth Uniyal, SOC, LBAD
- Shri Manoj, SOC, ALOD
- Shri Pranav Sharma, SOC, SCDD
- Kum. Diksha Joshi, SOC, LPSD
- Shri Akash Chaurasiya, SOC, LCID
- Kum. Harshaa, SOC, ISUD
- Shri Abhinav Raj, SOC, SMPCS
- Shri Harsh Shukla, SOC, IAD
- Shri Abhay Kumrawat, SOC, AMTD
- Shri Snehendu Bose, SOC, LBAD
- Shri Vinayak Shrivastava, SOC, CD
- Shri Santosh Yadav, Work Astt./A, Admin.
- Kum. Yasakshi Patle, UDC, Accounts
- Shri Pankaj Rawat, UDC, Admin
- Shri Tarzan Kumar, Work Astt./A, IRPSU

N.12: Superannuations

The following RRCAT colleagues retired during July 2025 to December 2025. RRCAT family wishes them a happy and healthy post-retirement life.

- Dr. Sudhir Kumar Dixit, OS, LG
  DoJ: 31-07-1987, DoR: 31-08-2025
- Dr. M.S. Ansari, SOH, LPSD
  DoJ: 01-08-1988, DoR: 31-07-2025
- Dr. Arup Banerjee, SOH, SLDD
  DoJ: 01-08-1989, DoR: 31-08-2025
- Dr. Alok Dubey, SOH, LBAD
  DoJ: 23-08-1993, DoR: 31-08-2025
- Smt. Musuku Seema, SOG, CDBID
  DoJ: 17-11-1989, DoR: 31-08-2025
- Shri Pramod Kumar Tripathi, SOG, LPD
  DoJ: 01-12-1989, DoR: 31-10-2025
- Shri Rajeev Kumar Mishra, SOG, LPSD
  DoJ: 05-05-1987, DoR: 31-10-2025
- Shri Lakshman Singh, SAG, IOD
  DoJ: 12-12-1989, DoR: 31-07-2025
- Shri S.L. Baghel, SAG, IOD
  DoJ: 17-11-1989, DoR: 31-07-2025
- Shri Ram Chayan Yadav, SAF, CSD
  DoJ: 21-08-1990, DoR: 30-11-2025
- Shri Ram Gopal, SAF, CSD
  DoJ: 04-01-1991, DoR: 30-11-2025
- Shri G. Muralidharan, SAF, HELOD
  DoJ: 29-10-1993 DoR: 31-12-2025
- Shri Babu Ram, Foreman/D, CSD
  DoJ: 31-12-1990, DoR: 31-12-2025
- Shri Ashok Kumar Dewangan, Foreman/C, SCCCS
  DoJ: 20-03-1995, DoR: 30-11-2025
- Shri Vasudev Prasad Sharma, Tech. Sup./A, DMTD
  DoJ: 29-11-1991, DoR: 31-12-2025
- Shri S. Sowrirajan, Tech. Sup./A, EDMD
  DoJ: 29-10-1993, DoR: 30-09-2025
- Shri Ranjeev Kumar Choudhary, Tech. Sup./A, ALOD
  DoJ: 26-10-1993, DoR: 31-12-2025
- Shri Hemant Chitre, Sr.Techn/H, CSD
  DoJ: 13-12-1999, DoR: 31-08-2025

Dr. Sudhir Kumar Dixit, Outstanding Scientist and Director, Laser Group superannuated on August 31, 2025 after a meritorious service of 38 years in the Department of Atomic Energy. He received M. Sc. Degree in Physics from Lucknow University in 1985 and his Ph. D. degree in the field of Laser Physics from Devi Ahilya Vishwa Vidyalaya, Indore in 1994. He joined the Laser Program of RRCAT, Indore in 1987 after graduation from 30th batch of BARC Training School, Mumbai. Dr. Dixit has strong expertise in the fields of Laser Technology Development, Optical Resonators, Non-Linear Optics, Interferometry, Fiber Bragg Gratings, Optical Fiber Sensors, and Laser Spectroscopy. As the Director of the Laser Group at RRCAT, he handled the scientific, administrative, and financial responsibilities of the Group. At the senior level, Dr. Dixit put special emphasis on and guided the activities regarding the development and utilization of advanced technologies, such as diode-pumped solid-state lasers and fiber lasers, laser-based additive manufacturing, and laser-based medical isotope production and instrumentation. He has served on various Committees of RRCAT as both Secretary and Chairman. As a member of the Board of Directors of AIC Pi-Hub, he took the lead in the technology transfer and incubation of RRCAT-developed advanced technologies to academic and industrial partners. He also held the position of Senior Professor at HBNI, Mumbai, and guided the Ph.D. and M. Tech. theses of several students. Dr. Dixit contributed to the selection, screening, and promotional interviews of DAE colleagues as a Member/Chairman of several committees. He has more than 250 publications in journals, conferences, and books to his credit. He has also delivered several technical lectures as an Invited Speaker at national and international conferences, both in India and abroad. Dr. Dixit has traveled widely abroad and visited major laser and accelerator institutes all over the world. The RRCAT family wishes him and his family a very happy, healthy, and fulfilling post-retirement life.

Dr. Arup Banerjee, Scientific Officer H and Head, Theoretical and Computational Physics Section, Laser Group, superannuated on August 31, 2025 after rendering meritorious service of 36 years in the Department of Atomic Energy. Dr. Banerjee made outstanding contributions in the fields of electronic properties of many-electron systems using density functional theory (DFT), optical response properties through time-dependent DFT, confined atoms and molecules, atomic clusters, and quantum optics. He received his B.Sc. and M.Sc. degrees in Physics in 1986 and 1988, respectively, from Delhi University. Dr. Banerjee graduated from the 32nd Batch of the BARC Training School in 1989 and joined the Laser Physics Division, RRCAT. He was awarded a Ph.D. degree by Devi Ahilya Vishwavidyalaya, Indore, in 2000. He visited the University of Texas, USA (2001), and the University of Calgary, Canada (2002), for postdoctoral work. Apart from his scientific research, he also contributed significantly to human resource development activities at RRCAT and held positions such as Head, BARC Training School; Head, Human Resource Development Section; and Dean (Academic), HBNI at RRCAT. He has more than 100 research publications in peer-reviewed journals. He was awarded the Homi Bhabha Science & Technology Award by DAE in 2009 and the Group Achievement Award in 2015. The RRCAT family wishes him and his family a very happy, healthy, and fulfilling post-retirement life.

Dr. Alok Dube, Scientific Officer H, Laser Biomedical Applications Division superannuated on Aug 31, 2025 after a meritorious service of 32 years in the Department of Atomic Energy. Dr. Dube obtained his PhD degree in Life Sciences from DAVV Indore and joined RRCAT as Scientific Officer 'D' in Aug 1993. He was involved in R&D work in the area of photo-biological and therapeutic effects of narrow band-width light and lasers. Dr. Dube made significant and innovative contributions in the development of in-house synthesized chlorophyll-based photosensitizers and its conjugates for use in anticancer and antimicrobial photodynamic therapy. His eminent research work generated one Indian patent and more than 50 publications in peer reviewed international journals. He was recipient of Group Achievement Award along with the team members for his contributions in the "design, development and utilization of optical techniques for high resolution biological imaging". Dr. Dube contributed to the HBNI Ph.D. program (Life Sciences), guided several Ph.D. students and served in various academic committees. The RRCAT family wishes him and his family a very happy, healthy, and fulfilling post-retirement life.

Career and Research Opportunities at RRCAT, Indore

1. Join as Scientific Officer

The selection of the Scientific Officers is done in a centralized manner by BARC, Mumbai, for all BARC Training Schools situated in different units of the Department of Atomic Energy.

https://www.barc.gov.in/careers/index.html#sandt

2. Join as Scientific Assistant

Graduates in science and diploma holders in various engineering branches are recruited through a two-year Stipendiary Training Scheme (Category-I) and they are recruited as Scientific Assistant-C.

https://www.barc.gov.in/careers/index.html#sandt

3. Join as Technician

Candidates having qualification of HSC (Science) or SSC followed by ITI certificate, are recruited under a two-year Stipendiary Training Scheme (Category-II), and they are recruited as Technician-B or Technician-C.

https://www.barc.gov.in/careers/index.html#sandt

4. Ph. D. Programme of HBNI at RRCAT

RRCAT invites students with appropriate qualifications to pursue Ph. D. programme in Physical Sciences, Engineering Sciences (Electronics/Electrical/Mechanical) and Life Sciences of the Homi Bhabha National Institute (HBNI), a Deemed University with NAAC "A" grade under Department of Atomic Energy.

https://www.rrcat.gov.in/hrd/advt/phdad.html

5. Project Work Opportunities for Students

RRCAT offers opportunities to the students pursuing M.Tech/M.E./M.Sc./B.E./B.Tech. degree in India for carrying out project work towards partial fulfillment of their degree programme.

https://www.rrcat.gov.in/hrd/advt/project.html

6. Trade Apprenticeship Scheme (TASAR) at RRCAT

TASAR is a skill development scheme for young ITI trained personnel, by providing them access to advanced engineering infrastructure and opportunity to work under the guidance of experienced engineers and scientists at RRCAT.

https://www.rrcat.gov.in/hrd/Openings/tasar.html#

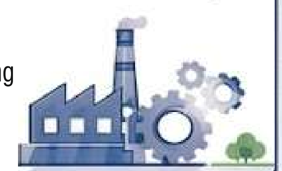

Indigenously built first high-RRR niobium sheet handed over to Shri Unmesh D. Malshe, Director, RRCAT by Dr. Ajit Kumar Mohanty, Chairman, AEC & Secretary, DAE, at NFC, Hyderabad

6th batch of TQLP staff for Indus facility

Shri Viraj P. Bhanage, Director, Electron Accelerator Group, RRCAT and other senior officials during plantation drive

RRCAT Newsletter is a publication of Raja Ramanna Centre for Advanced Technology, Indore 452013
Website: www.rrcat.gov.in/newsletter/NL
Email: newsletter@rrcat.gov.in
(For private circulation only)

Printed at :
Printing Arts # 9826604242